

Stochastic Computation of Quasibrittle Fracture

A DISSERTATION
SUBMITTED TO THE FACULTY OF THE
UNIVERSITY OF MINNESOTA
BY

Anna Gorgogianni

IN PARTIAL FULFILLMENT OF THE REQUIREMENTS
FOR THE DEGREE OF
DOCTOR OF PHILOSOPHY

Jia-Liang Le, Advisor

August 2021

© Anna Gorgogianni 2021

Acknowledgements

Reflecting on these challenging and rewarding years of my doctoral studies at the University of Minnesota, I would like to firstly give my gratitude to my advisor, Professor Jia-Liang Le, for the exciting research project he assigned to me, for exposing me to areas of knowledge I had not previously explored, for his guidance and commitment to the progress of my research and of myself as a researcher. Besides, I would like to express my appreciation to Professor Jan Eliáš at Brno University of Technology for our close collaboration throughout these years, for his efforts, inspiring enthusiasm and constructive criticism.

I thank Professor Henryk K. Stolarski, Professor Emmanuel Detournay and Professor Ellad B. Tadmor at the University of Minnesota, for serving in my Ph.D. committee. I indeed consider myself extremely lucky having been a student of them; I admire Professor Stolarski's ability to present tough concepts in a simple and meaningful way, Professor Detournay's physical intuition and critical thinking, Professor Tadmor's clarity in teaching and instructional feedback that allows students to find the answers themselves.

I deeply appreciate the friendship and support of other members of the research group, particularly Dr. Anu Tripathi and Dr. Teng Man, as well as Mr. Chen Hu and Mr. Tianhao Yan. Many thanks to Dr. Zhifeng Xu and Mr. Joshua Vievering for our collaboration.

I also acknowledge the financial support for my doctoral studies provided by the U.S. Army Research Office, the U.S. Department of Energy, and the Department of Civil, Environmental and Geo-Engineering (CEGE) of the University of Minnesota. I thank the Department Head, Professor Joseph F. Labuz, as well as all faculty members at CEGE for the welcoming academic environment they have created.

I strongly feel the need to express my gratitude to my former advisors in Greece, Professor Sofia Papargyri-Beskou at the Aristotle University of Thessaloniki and Professor Dimitri E. Beskos at the University of Patras. I thank them for guiding me during my very first research experience, for further solidifying my interest to continue with advanced studies, and for holding me up during

personal hardship. I thank all my former educators for they have largely shaped my thinking. I am also grateful to Dino Xykis, former Ph.D. graduate of the CEGE Department at the University of Minnesota, for his help during my arrival in the U.S. and encouragement in my doctoral studies.

I am more than thankful to my parents, Ioannis and Evangelia, for their devotion to my well-being and personal development which has been the driving force for all my efforts. I also thank my sister Eleni, my aunts Chariklia and Maria, and my precious friends in Greece for their love and support that reveals the bright side of life.

To my father, for shaping my character
and guiding my thought.

“If one way be better than another, that you may
be sure is nature’s way.”

Aristotle

ABSTRACT

Continuum finite element (FE) modeling of quasibrittle fracture is a challenging task. It is well known that the continuum approaches suffer from the issue of spurious mesh sensitivity due to localization instability. The issue of mesh dependence must be addressed to ensure the robustness of FE simulations. Numerical techniques to mitigate the spurious mesh sensitivity include localization limiters such as nonlocal continuum models, as well as energy regularization methods such as the crack band model. Nonlocal integral formulations and implicit gradient models, have been shown to be largely equivalent to each other, able to recover mesh-objective failure patterns that preserve the finite size of localization bands as well as mesh-objective global structural response. A drawback of these techniques is the need for sufficiently small mesh sizes to capture the nonlocality or resolve the gradient terms, which makes them inefficient for the analysis of large-scale structures. On the other hand, the crack band model addresses solely the mesh dependence of the global structural response only for cases of failure with severe strain localization. It is computationally efficient for large-scale simulations since it allows use of elements of size larger than the material-dependent localization bandwidth.

The first part of this dissertation focuses on mitigating the mesh dependence of FE simulations of softening continua in the deterministic setting, by proposing a general energy regularization scheme. In contrast to the crack band model, the proposed model captures the effect of the failure mechanism on the energy regularization of the constitutive law. Considering that each finite element represents a material element of finite size, the constitutive law assigned to it should generally depend on both the material properties as well as the failure pattern of the corresponding element. The goal of energy regularization methods is to ensure correct amount of energy dissipation in simulations of failure. In cases of a purely localized damage pattern, the post-peak part of the input constitutive law must be adjusted according to the element size such that the fracture energy is preserved. However, in cases of diffused damage, the input constitutive model represents purely material behavior and should thus be independent of the element size. In order to mathematically describe the actual damage pattern, which evolves during the loading process, the present study introduces a localization parameter which

is calculated from the spatial distribution of the damage variable and is updated at every loading step. The localization parameter governs the energy regularization of the constitutive law, and can capture the transition from diffused to localized damage during the failure process. The method is cast into an isotropic damage model, and is further extended to rate-dependent behavior. The proposed model is applied to FE simulations of static and dynamic failure of ceramic specimens. The results show that the model is highly effective in mitigating mesh dependence of the global response of quasibrittle structures experiencing different failure mechanisms.

An important feature of the aforementioned mechanism-based energy regularization scheme is that it does not require any a priori knowledge of the structural failure mechanism. In the second part of this dissertation, the model is extended to stochastic FE simulations of quasibrittle structures with spatially varying element tensile strengths and fracture energies. Focus is placed on the case when the finite element mesh size is larger than the crack band width of the material, as well as the autocorrelation length of the underlying random fields of constitutive properties. For general loading scenarios it is not possible to know the evolving failure mechanism. Therefore, use of pre-assumed sampling distribution functions of the random element strengths following some well-established models such as the weakest-link or fiber-bundle model, which is a common practice in the literature, could be inconsistent with the actual failure mechanism. It is well known that the probability distributions of fracture properties of a material element depend on the failure mechanism. For instance, the weakest-link model is applicable for failures with damage localization, whereas the fiber-bundle model is suitable for failures with distributed cracking. In this study, a general probabilistic model of fracture properties of finite elements is proposed. The probability distribution of the fracture property of strength depends on the evolving failure mechanism and can transition from a fiber-bundle model representation of structural failure to a weakest-link model as damage localization emerges from diffusive damage. This is achieved by introducing a dependence of the sampling distribution functions of apparent fracture properties on numerical parameters describing the damage pattern and introduced in the energy regularization scheme (e.g. localization parameter). Hence, the size effects on the statistics of fracture properties arising due to the failure mechanism of an element are taken into account. The model is applied to stochastic FE simulations of quasibrittle structures of different geometries, subjected to different loading configurations. The simulation results show that the mesh dependence of the output probabilistic structural response is effectively mitigated. Most importantly, the mechanism-based energy regularization scheme and the proposed probabilistic model are interconnected and are always consistent with the actual failure mechanism of the structure, resulting in a unified and general framework for addressing the mesh dependence

of numerical simulations of quasibrittle failure in both deterministic and stochastic settings.

Contents

List of Figures	x
1 Introduction	1
1.1 Background	1
1.2 Numerical Modeling of Quasibrittle Failure	4
1.2.1 Cohesive Crack Model and Discrete Element Models	4
1.2.2 Crack Band Model	8
1.2.3 Nonlocal Damage Models	10
1.2.4 Phase-Field Models	13
1.3 Probabilistic Modeling of Strength Distribution of Quasibrittle Structures	16
1.3.1 Chain Model	17
1.3.2 Fiber-Bundle Model	18
1.3.3 Fishnet Model	20
1.4 Research Outline	22
2 Energy Regularization in Deterministic Numerical Simulations of Strain-Softening Continua	24
2.1 Model Formulation	25
2.2 Extension to Rate-Dependent Behavior	31
2.3 Simulations of Quasi-Static Failure	35
2.4 Simulations of the Dynamic Spalling Test	40
2.5 Conclusions	44
3 Rate and Size Effects on Strength Distribution of Quasibrittle Structures	46
3.1 Stochastic Discrete Model Simulations of Dynamic Failure	47

3.1.1	Model Description	47
3.1.2	Simulations of Dynamic Tensile Failure of Aluminum Nitride Specimens . . .	52
3.2	Rate-Dependent Finite Weakest Link Model	56
3.2.1	Model Formulation	56
3.2.2	Numerical Verification	62
3.3	Conclusions	68
4	Stochastic Numerical Simulations of Strain-Softening Continua	69
4.1	Model Formulation	70
4.1.1	Probabilistic Modeling of Element Fracture Properties	70
4.1.2	Description of the Local Damage Pattern	77
4.2	Numerical Examples	81
4.2.1	Description of Analysis	81
4.2.2	Unnotched beams under three-point bending	83
4.2.3	Notched beam under three-point bending	87
4.2.4	Unnotched beam under four-point bending	90
4.3	Conclusions	92
5	Conclusions	94
	Bibliography	97

List of Figures

1.1	Probabilistic analysis of failure of a strain softening bar under uniaxial tension . . .	3
1.2	Characterization of fracture	5
1.3	Cohesive crack model	6
1.4	Cohesive laws	6
1.5	a) Crack band parallel to the element sides in a square mesh, and b) Crack band along the element diagonals in a square mesh	10
1.6	a) Nonlocal weighting function, and b) treatment of the weighting function near the structural boundaries	12
1.7	A solid body Ω with the crack set Γ : a) sharp cracks, and b) approximated diffuse crack bands	14
1.8	Probabilistic models of structural failure: a) chain model, b) fiber-bundle model, and c) fishnet model	16
1.9	a) Hierarchical model of the RVE, b) idealization of the force transmission mechanisms inside the FPZ, and c) stress-strain diagrams of the coupled elements	18
2.1	Two distinct crack patterns in a material element represented by a finite element: a) localized cracking, and b) diffused cracking	27
2.2	Schematic of finite element mesh for defining the localization parameter	28
2.3	Uniaxial tensile stress-strain curves for different mesh sizes for the case of fully local- ized damage	31
2.4	Rate-dependent uniaxial tensile stress-strain behavior of a material element for the case of fully diffused damage	33
2.5	Rate effect on material properties: a) apparent tensile strength, b) fracture energy, and c) Irwin's characteristic length	34

2.6	Notched and unnotched three-point bend beams considered in the simulation (all dimensions are in mm)	35
2.7	Evolution of the damage pattern of the notched beam	36
2.8	Simulation results of the notched beam: a) load-displacement curves, and b) profile of normal stress along the ligament for the diffused damage model	37
2.9	Snapshots of the damage pattern of the unnotched beam during the loading process	38
2.10	Simulated load-displacement curves of the unnotched beam	39
2.11	a) Schematic of the modified split Hopkinson bar test, b) stress wave traveling in the bar, c) stress pulse used in the present simulations, and d) discretization of the bar	40
2.12	Time histories of free-end velocity predicted by the localized damage model (first row), the diffused damage model (middle row), and the present model (bottom row)	41
2.13	Time histories of energy dissipation simulated by the localized damage model (first row), the diffused damage model (middle row), and the present model (bottom row)	43
2.14	Snapshots of the damage pattern of the bar at different times simulated by the localized damage model	44
2.15	Snapshots of the damage pattern of the bar at different times simulated by the present model	45
3.1	Representation of the discrete element model: a) domain discretization, and b) Voronoi body and facet	48
3.2	A typical realization of the random field $h(\mathbf{x})$	51
3.3	A rectangular specimen loaded by a prescribed strain rate: a) schematic of the specimen, and b) weakest link model representation	52
3.4	Simulated average nominal stress-strain curves for different specimen sizes and strain rates	54
3.5	Simulated damage patterns of specimen of $D = 400\mu\text{m}$ at the peak load	55
3.6	Modeling of strength distribution of a RVE: a) hierarchical model of static RVE, and b) fiber-bundle model of RVE under high strain-rate loading	57
3.7	Simulated mean size effect curves of nominal strength at different strain rates and the optimum fits by the rate-dependent finite weakest-link model	63
3.8	Effect of the strain rate on the RVE size	64
3.9	Rate dependence of the statistical parameters of $P_1(\sigma_N)$	65

3.10	Simulated size effects on the standard deviation of nominal strength at different strain rates and its comparison with the rate-dependent finite weakest-link model	67
4.1	A finite element with a damage zone consisting of n_b number of crack bands	71
4.2	Schematic of finite element mesh for calculation of the localization and propagation parameters	79
4.3	Geometry of unnotched beams under three-point bending considered in the simulation (all dimensions are in mm)	84
4.4	Mean (left) and standard deviation (right) of peak load of the unnotched beam under three-point bending with probabilistic models I)-III) ($\bar{G}_{f0} = 50\text{J/m}^2$)	84
4.5	Mean (left) and standard deviation (right) of peak load of the unnotched beam under three-point bending with probabilistic models I)-III) ($\bar{G}_{f0} = 15\text{J/m}^2$)	87
4.6	Notched beam under three-point bending considered in the simulation (all dimensions are in mm)	88
4.7	Mean (left) and standard deviation (right) of peak load of the notched beam under three-point bending with probabilistic models I)-III)	90
4.8	Unnotched beam under four-point bending considered in the simulation (all dimensions are in mm)	91
4.9	Mean (left) and standard deviation (right) of peak load of the unnotched beam under four-point bending with probabilistic models I)-III)	92

Chapter 1

Introduction

1.1 Background

Failure of engineering structures made of brittle heterogeneous, aka quasibrittle materials, is caused by material fracture, which is commonly referred to as quasibrittle fracture. A salient feature of quasibrittle fracture is the formation of a fracture process zone (FPZ) whose size is not negligible compared to the characteristic structural dimensions. The failure behavior of quasibrittle structures is dependent on the ratio between the structure size and the FPZ size, and transitions from quasi-plastic to perfectly brittle with increasing values of this ratio. At the scale of normal laboratory testing, typical examples of quasibrittle materials include concrete, composites, ceramics, rock, cold asphalt, etc.

Quasibrittle materials exhibit a strain-softening constitutive behavior, defined as decreasing stress at increasing strain in the one-dimensional setting, which may result in strain localization. Strain localization can be considered as an instability of the constitutive description of the material, which may allow the emergence of discontinuities in the deformation field, with the formation of a band of non-uniform deformation and continuing equilibrium, whereas outside the localization band the initial conditions of homogeneous deformation continue to be satisfied [124]. The localization instability was initially studied for finite strain plasticity and its onset was analyzed by the acoustic tensor [124]. It was found that strain localization in rock masses described by von Mises plasticity could occur at either positive or negative values of the hardening modulus, depending on the details of the incremental constitutive relation [124]. The analysis was limited to the behavior of a material point in an infinite space, and the stability of the initial state of uniform strains against localiza-

tion was not examined. The above considerations were taken into account in [20–22, 82], where the condition for the onset of localization was extended to arbitrary constitutive laws and to bodies of finite size. The effects of the size of the localization band and of unloading of the material outside the localization region were also taken into account. Besides, the stability of inelastic structures was studied within the framework of thermodynamics upon introducing the concept of the tangentially equivalent elastic structure in [12]. It was shown that [12, 22], out of the infinitely many equilibrium paths emanating from a bifurcation point in the load-displacement diagram of an inelastic structure with homogeneous properties, the one that will be actually followed by the structure, as dictated by the 2nd Law of Thermodynamics, is not the path corresponding to homogeneous deformation, but rather the path with strains localizing inside the narrowest possible region, the localization band, whereas the surrounding structure experiences unloading.

Based on the preceding conclusion, in finite element (FE) simulations of softening continua, strain localization would occur in a single finite element, or even in a subdivision of the element defined by its Gauss points [79]. Thus, upon mesh refinement, the overall volume of the localization band tends to zero. This implies that the energy expended to form a damage band tends to zero. Consequently, a smaller mesh size will lead to a more brittle failure behavior of the simulated structure, which is known as the spurious mesh sensitivity of FE simulations. Various methods, known as the localization limiters, have been proposed to address this problem by preventing the strains from localizing into infinitesimally small regions. These methods will be briefly discussed in Section 1.2.

Another issue that has received very limited attention is the spurious mesh sensitivity of stochastic FE simulations of quasibrittle fracture. This can be demonstrated by considering a quasibrittle bar under quasi-static uniaxial tension, which is sub-divided into several elements along its length (Fig. 1.1a)). Due to the strain-softening behavior, strains will localize into one element and the maximum load capacity of the structure will be determined by the strength of this element. Considering the tensile strength f_t and fracture energy G_f as the constitutive parameters governing the failure behavior and thus modeling those only as statistically independent random variables, the peak load of the bar P_{\max} is governed by the minimum of the random strengths of the elements in the mesh, i.e. $P_{\max} = A_0 \min(f_{ti})$, where A_0 is the cross sectional area and f_{ti} denotes the tensile strength of the i_{th} element. Without introducing any mesh-size dependence of the input distributions of the constitutive parameters, a finer mesh will render a lower mean peak load, and the probability distribution of P_{\max} will depend on the number of elements. The existing localization limiters cannot address the mesh sensitivity of stochastic simulations, since they were formulated within a purely

deterministic framework. To demonstrate this, the cumulative distribution function (cdf) of P_{\max} was calculated using the conventional crack band model [17], with some commonly employed assumptions: 1) the material has a linear softening stress-strain behavior (Fig. 1.1b)), 2) the material strength and fracture energy of each element are statistically independent random variables, and 3) the cdf of f_t of each element follows a Gauss-Weibull grafted distribution [14, 90]. Fig. 1.1c) shows the computed cdfs of P_{\max} for different element sizes. It can be seen that the resulting cdf of the peak load strongly depends on the element size. On the other hand, the cdf of the total energy dissipation of the bar is independent of the element size (Fig. 1.1d)) since the crack band model was used to regularize the fracture energy.

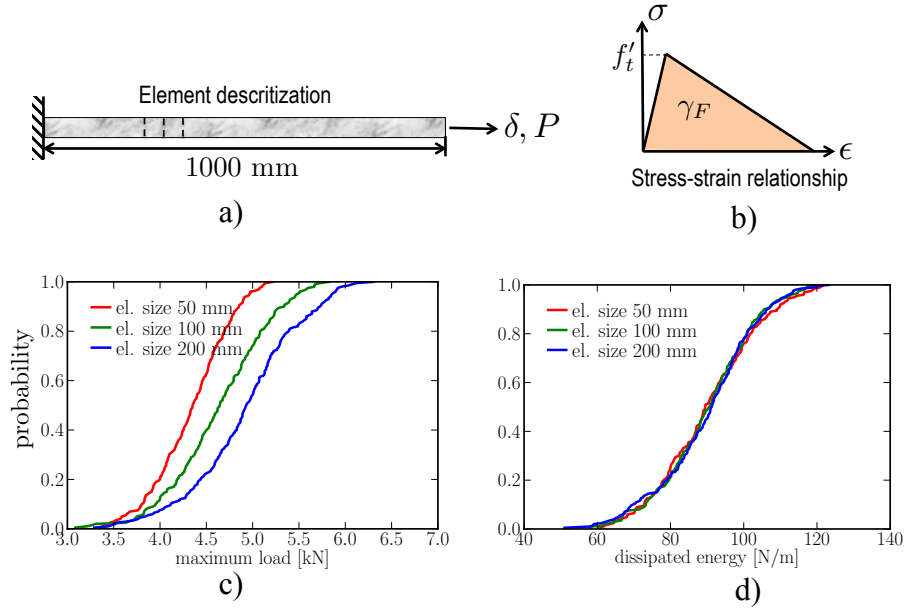


Figure 1.1: Probabilistic analysis of failure of a strain softening bar under uniaxial tension

As has been demonstrated, strain localization due to softening can lead to the spurious mesh sensitivity of FE simulations of quasibrittle fracture, in both the deterministic and stochastic settings. Quasibrittle structures can exhibit a complex damage pattern, featured by both diffused and localized damage, depending on the loading configuration and structural geometry. For instance, strain-rate effects have been shown to significantly affect the failure mechanism of quasibrittle structures [54, 68, 91]. The prevalent damage pattern has profound implications on the regularization of the constitutive law of finite elements. The goal of this research is to develop a general framework, that

is able to take into account the evolving state of damage in a structure and address the issue of mesh dependence under general failure patterns, for both cases of deterministic and stochastic analyses.

1.2 Numerical Modeling of Quasibrittle Failure

1.2.1 Cohesive Crack Model and Discrete Element Models

Fracture is accompanied by the formation and propagation of a macroscopic crack. At the crack tip, on account of the stress concentration, irreversible deformation occurs and a nonlinear zone is formed. This nonlinear zone could consist of the fracture process zone (FPZ), which exhibits softening damage due to microcracking (and is denoted with black color in Fig. 1.2), and a plastic (or yielding) zone surrounding the FPZ, which can exhibit perfect or hardening plasticity due to small scale yielding and void growth. Depending on the dimensions of the FPZ compared to the structure size, fracture can be characterized as brittle, ductile or quasibrittle. In brittle fracture, the entire nonlinear zone, and therefore the FPZ as well, is very small compared to the structural dimensions and can be lumped into a single point. As a consequence, the entire volume of the structure remains elastic and the theory of linear elastic fracture mechanics (LEFM) is applicable. In ductile fracture, observed in elastoplastic materials such as metals, the nonlinear plastic zone is of significant size, whereas the FPZ remains negligible. In quasibrittle fracture, which is the focus of this dissertation, it is the size of the FPZ which is non-negligible compared to the structural dimensions, whereas the nonlinear yielding zone is very small, almost pointwise, so that it can be considered that the boundary of the FPZ coincides with that of the plastic zone.

In the numerical modeling of quasibrittle fracture, an explicit representation is required for the deformation mechanisms inside the FPZ. Cohesive zone models (CZM), introduced by Barenblatt [6] and Dugdale [57] for elastic-plastic fracture in ductile metals, and for quasi-brittle materials by Hillerborg et al. [74] in the so-called fictitious crack model, model the FPZ as a line (Fig. 1.3). The damage behavior of the FPZ is described by a softening cohesive law, which relates the cohesive traction to the opening displacement w (Fig. 1.4). The cohesive law is regarded as a material property (Eq. (1.1)):

$$\sigma_{yy} = f(w) \tag{1.1}$$

Eq. (1.1) can be considered as an accurate description of the constitutive behavior of the FPZ in the case when the normal stresses σ_{xx} and σ_{zz} along the crack plane are negligible compared to the compressive and tensile material strengths, otherwise a tensorial constitutive law would be needed

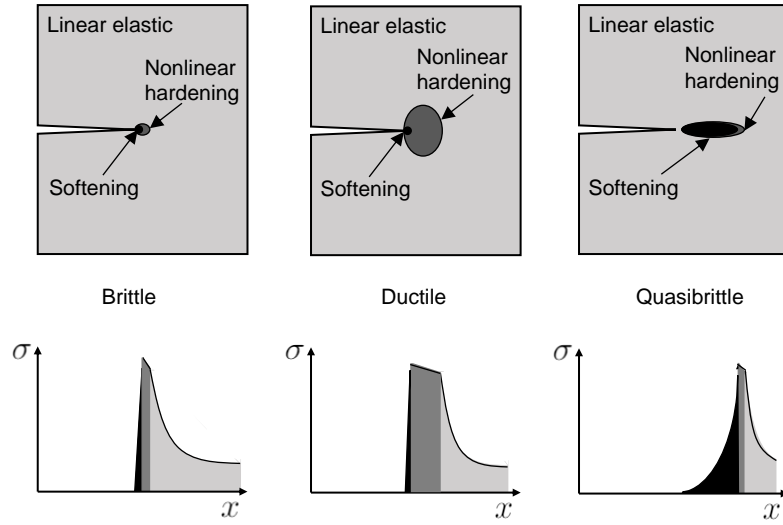


Figure 1.2: Characterization of fracture

(Sections 1.2.2, 1.2.3). Two of the most important parameters of the cohesive law described by Eq. (1.1) are the material tensile strength $f(0) = f_t$, which is the stress level at which the cohesive opening is activated, and the fracture energy G_F , defined as the energy required to create a unit of new surface area along the crack line. It can be shown that G_F is equal to the area under the softening curve:

$$G_F = \int_0^{w_f} f(w)dw \quad (1.2)$$

where w_f is a critical value of the opening of the cohesive crack, after which the stress at the corresponding location reduces to zero. Thus, the point at which $w = w_f$ and $\sigma_{yy} = 0$ corresponds to the tip of the real traction-free crack.

Fig. 1.4 shows examples of some commonly used decohesion relations: a) a simple linear relation, b) a stress-separation relation with a horizontal yield plateau applicable for ductile fracture, and c) a bilinear curve, which has been used as a realistic cohesive law for concrete by [29, 52]. The cohesive stress σ_{yy} decays from the finite failure strength f_t to zero, removing the LEFM stress singularity at the crack tip. For the case of brittle fracture, LEFM is applicable and can provide a good approximation to the predictions of the cohesive zone model. In brittle fracture, the most important property of the cohesive law is the material fracture energy G_F , since it fully controls the peak load of the structure, irrespectively of the assumed shape of the softening curve. For quasibrittle fracture, the precise shape of the stress separation law plays a significant role in the proximity of the predicted mechanical response of the structure to experimental results [43].

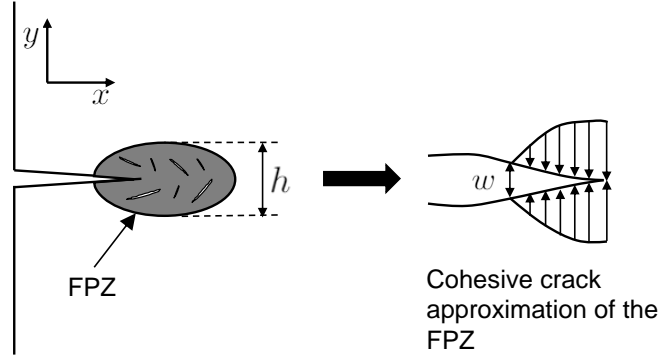


Figure 1.3: Cohesive crack model

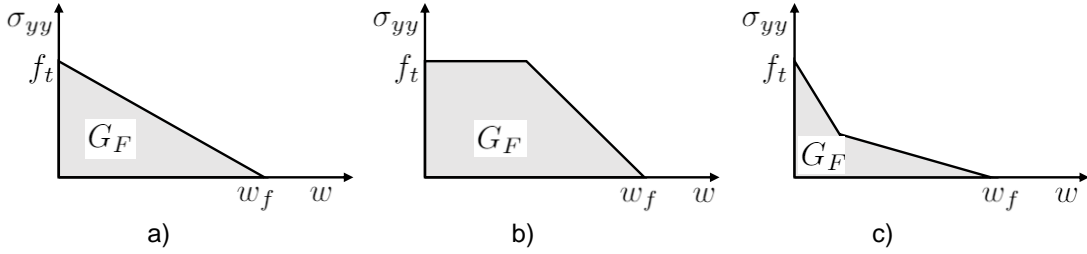


Figure 1.4: Cohesive laws

Given that the material properties of fracture toughness G_F and failure strength f_t introduced in cohesive laws are independent and have different dimensions, the so-called Irwin's internal length l_{ch} is usually introduced to characterize the length of the fracture process zone (FPZ) ahead of the crack tip:

$$l_{ch} = \frac{EG_F}{f_t^2} \quad (1.3)$$

For a vanishing internal length, $l_{ch} \rightarrow 0$, Griffith's brittle fracture is asymptotically recovered [66]. Therefore, Barenblatt's CZM can be used not only for cohesive fracture, but also for brittle fracture.

Another major advantage of the cohesive crack model is that it allows for the entire volume of the structure to be treated as elastic since all the nonlinearity of the FPZ is embedded in the boundary conditions at the crack faces. One important limitation of cohesive zone models, though, is that they cannot account for triaxiality of the stress field ahead of the crack tip, which can lead to premature fracture through its effect on the fracture toughness of the material. Besides, cohesive crack models are computationally expensive, requiring topological changes in the mesh to account for

the displacement discontinuities due to crack propagation, and the predicted crack paths are mesh dependent, because fracture is considered to occur only along the interface zero-thickness cohesive elements.

The cohesive crack models described above constitute numerical tools for modeling fracture within the discrete approach, since they allow discontinuities in the displacement field (i.e. strong discontinuities). Other models of softening damage and fracture of quasibrittle materials belonging to the same approach, are the discrete models in the form of either lattice or particle models, which consist of a collection of interconnected rigid bodies organized into a net structure. The first lattice model was introduced by Hrennikoff [75] for the solution of elasticity problems, and in the 1970s and 1980s lattice models were employed for the study of the fracture process of disordered media in theoretical physics [61, 73, 123, 125, 139]. Further developments of the lattice discrete model for 2D and 3D simulations of quasibrittle fracture were made by [28, 47, 48, 80, 81, 127, 141].

The discrete particle model was originated from the so-called distinct element model [45, 46], which was developed for capturing the behavior of particulate materials such as cohesionless soils and rock masses. The model was further extended to concrete materials [141], in which the computational domain consisted of a set of rigid polyhedral elements. In further extensions of this approach, the connections between elements were implemented by nonlinear springs of zero length [36, 37, 85]. An important feature of discrete element models is the introduction of a characteristic length scale (e.g., particle size or lattice size), which prevents fracture from localizing into infinitesimally small regions and thus ensures a finite amount of dissipated energy in the fracture process.

Recently, significant advances have been made towards realistic discrete models for various concrete materials. The lattice discrete particle model (LDPM) of Cusatis and coworkers [47, 48, 51], which considered the random size distribution of concrete heterogeneities, has been experimentally validated under many loading scenarios, and was shown to give very realistic predictions of cracking damage and fracture. Discrete element models can also account for the randomness of mesoscale constitutive properties, and they have been successfully applied in stochastic simulations of quasibrittle fracture [59, 69].

In general, discrete models have two major advantages: 1) they are based on a discontinuous formulation, which avoids the singularity-related issues of continuum-based numerical simulation methods, such as the finite element method (FEM), and 2) they allow for explicit representation of the microstructure of the material [114]. Owing to the second advantage, lattice or particle models are dominant in the simulation of the mesoscale or microscale of materials, where the effects of material heterogeneity should be considered. A major disadvantage of discrete element models

though is their high computational cost, which hampers their application for the simulation of large-scale structures. For this reason, recent research efforts have focused on the development of robust multiscale computational frameworks, which aim to bridge the discrete with the continuum approach to fracture [120].

1.2.2 Crack Band Model

The crack band model [17] is a generalization of the discrete cohesive zone concept to a continuum formulation by smearing the inelastic strains due to microcracking over the width of the FPZ. The average inelastic strain $\overline{\epsilon''_{yy}}$ inside the FPZ is defined from the relationship $w(x) = \int_0^h \overline{\epsilon''_{yy}}(x, y) dy$, where $w(x)$ is the cohesive crack opening and h the crack band width (Fig. 1.3). Assuming that the inelastic damage strain is uniformly distributed across the crack band width, its pointwise value $\epsilon''_{yy}(x, y)$ coincides with the average value and thus we have $\epsilon''_{yy} = \overline{\epsilon''_{yy}} = w/h$. This assumption also implies that the fracture energy under mode I loading (opening mode) is given by:

$$G_F = h \int_0^{\epsilon_f} \sigma_{yy} d\epsilon''_{yy} \quad (1.4)$$

where $\epsilon_f = w_f/h$ is the ultimate fracturing strain after which the stress component normal to the localization plane decreases to zero. In contrast to the cohesive crack model, the crack band model allows for description of the constitutive behavior of the FPZ by a triaxial nonlinear constitutive law, which can be written in general form as:

$$\sigma_{ij} = F_{ij}(\epsilon_{kl}) \quad (1.5)$$

where σ_{ij} , ϵ_{kl} are the stress and strain tensors, i, j, k, l are Cartesian tensorial subscripts and F_{ij} is a function of a history functional. Such constitutive law takes into account all other stress components that can exist with or without the presence of σ_{yy} , which allows for a much richer description of mechanical behavior. For instance, the shear components can lead to change of the direction of propagation of the crack band, whereas the normal compressive stress components parallel to the crack plane can precipitate failure and are able of causing splitting fracture, even in the absence of the σ_{yy} stress component.

In finite element analysis, the crack band is modeled as a stack of finite elements undergoing damage. The constitutive behavior of the elements inside the localization band can exhibit gradual softening, but it has also been checked [11] that the model is applicable for brittle failure as well,

since the stress intensity factor K_I calculated for the case of elements exhibiting a sudden post-peak stress drop was very close to the LEFM prediction (within 1% error at most). On the other hand, the cohesive zone model is represented as an interface element of zero thickness, and, in contrast to the crack band model, requires topological changes in the mesh in order to capture the displacement discontinuity arising from crack initiation at the element boundaries. It can be considered as an approximation of the crack band model neglecting the effect of the finite FPZ width.

Use of the crack band model in finite element analysis, which is more convenient than use of the cohesive crack model, requires the user to specify the constitutive behavior of an element of size equal to the crack band width. Apart from being a numerical parameter, the size of the elements forming the localization band, (crack band width), is physically related to the width h of the FPZ, which is a material property. The crack band width can be measured experimentally as the minimum possible spacing of parallel cracks in specimens that have been designed so as to fail with distributed cracking [27]. However, if the user selects elements of size $h_e = h^*$ larger than the material property of h (for instance for reasons of computational efficiency), a scaling of the post-localization part of the input constitutive law according to the chosen element size h^* is required, so as to always dissipate the same amount of energy during failure of the elements inside the developed band of localized strains, independently of their size. This mesh-dependent adjustment of the post-peak part of the constitutive law is essential in order to ensure the mesh objectivity of finite element simulations of strain-softening continua for the case of failure with strain localization.

The crack band model cannot address the issue of mesh-induced directional bias and thus its efficiency in mitigating mesh dependence is maximized when the mesh lines are aligned with the direction of crack band growth (Fig. 1.5a)). In case when the mesh lines are inclined with respect to the direction of crack propagation, the crack band width h can be determined by applying correction factors to the element dimensions (Fig. 1.5b)). In general, the method of estimate of the effective band width in finite element simulations using the crack band model can significantly affect its performance in mitigating mesh dependence [79], since the scaling of the constitutive law according to this model is based on the width of the FPZ, which may not always coincide with the finite element width (Fig. 1.5b)).

Finally, it should be noted that the crack band model regularizes the global load-displacement behavior of the structure. However, the numerically resolved width of the FPZ decreases and tends to zero upon mesh refinement [25]. For more complex constitutive laws, it becomes increasingly hard to identify which parameters govern the global behavior of the structure and should thus be adjusted so as to mitigate mesh dependence by regularizing the energy dissipation in the softening

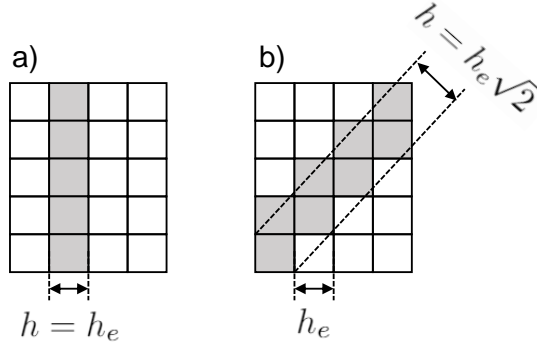


Figure 1.5: a) Crack band parallel to the element sides in a square mesh, and b) Crack band along the element diagonals in a square mesh

region. Other limitations of the crack band model include its rather simplified assumption of the failure mechanism of the structure. It assumes that damage localization occurs as soon as damage initiates. Meanwhile, as discussed earlier, the crack band model is also inefficient in mitigating mesh dependence of stochastic finite element simulations, since it does not take into the randomness in the location of crack band formation inside an element, as originating from the underlying random field of material strength. The present dissertation particularly focuses on improving the energy regularization methods within the crack band concept so as to overcome these last two limitations.

1.2.3 Nonlocal Damage Models

The development of cavities in the microscopic, mesoscopic and macroscopic processes of fracture in materials together with the resulting deterioration in their macroscopic properties is called damage [83, 94, 108]. Continuum damage mechanics aims at the analysis of damage development in mesoscopic and macroscopic fracture processes in the framework of continuum mechanics. More specifically, the mechanical effects of progressive microcracking, void nucleation and growth are represented by a set of state variables which act on the elastic and/or plastic behavior of the material at the macroscopic level [118].

Description of the softening behavior of quasibrittle materials through continuum damage mechanics models can lead to localization instability and the spurious mesh sensitivity of finite element analysis. One of the simplest remedies to alleviate mesh dependence of the global response is the crack band model, described in Section 1.2.2. However, because continuum damage models are formulated in terms of a stress-total strain relation, rather than an additive decomposition of the strain to its elastic and inelastic part, it is not easy to scale only the postlocalization part of the strain, as

dictated by the crack band model, while keeping the unloading part unaffected [25]. Contrariwise, smeared crack models [17] decompose the strain into elastic and inelastic parts and hence make application of the crack band model more convenient.

Another, more rigorous method of mitigating mesh dependence, are nonlocal formulations, which are able to fully regularize the problem in the sense that the resulting strain field is highly concentrated in narrow zones but remains continuous [78]. Not only are nonlocal models able to suppress mesh sensitivity of numerical simulations, but they also prevent strain localization into arbitrarily small regions, which is why they are often characterized as true localization limiters, differentiating them from partial localization limiters such as the crack band model and rate-dependent models. The general approach in nonlocal models is to replace a certain variable at a given point by its nonlocal counterpart, which is obtained by weighted averaging in the spatial neighborhood of the point under consideration. In the first formulations of nonlocal models [24], the stress tensor at a point \mathbf{x} is calculated from the nonlocal strain tensor at the same point $\bar{\epsilon}(\mathbf{x})$, which is defined by the following relation:

$$\bar{\epsilon}(\mathbf{x}) = \int_{V_0} \alpha(\mathbf{x}, \mathbf{x}') \epsilon(\mathbf{x}') dV(\mathbf{x}') \quad (1.6)$$

where $\alpha(\mathbf{x}, \mathbf{x}')$ is an empirical bell-shaped weighting function (Fig. 1.6a)), and V_0 is the volume of the neighborhood whose size is controlled by a characteristic length of the material.

Since one of the goals of the development of nonlocal models has been preventing strain localization, which most often occurs after inelastic processes initiate, nonlocality may be introduced only in the variables that control the inelastic behavior, e.g. damage variable, and in this case nonlocal models can reduce to standard local models at low strain values. This prevents some problematic issues related to the original formulations, that applied the nonlocal averaging (Eq. (1.6)) to the elastic part of the strain as well, leading to dispersive wave propagation even in homogeneous elastic continua [15].

The efficiency of nonlocal models in preventing strain localization into regions of diminishing size can be explained as follows. If strains tend to localize in a very narrow region, the nonlocal strain, by its definition (Eq. (1.6)), will become high not only in the material point with high local strain, but also in its immediate neighborhood. The damage variable, which depends on the nonlocal strain, will grow in the neighborhood of the material point as well. Considering the simple case of a uniform stress field (e.g. static equilibrium of a bar under uniaxial tension with zero body forces), damage growth in the close neighborhood will lead to increase of the local strains so as to keep the stress constant, therefore localization of strain and damage in an infinitesimal region is prevented. The region of localized strains has a finite size, which is dictated by the length scale involved in the

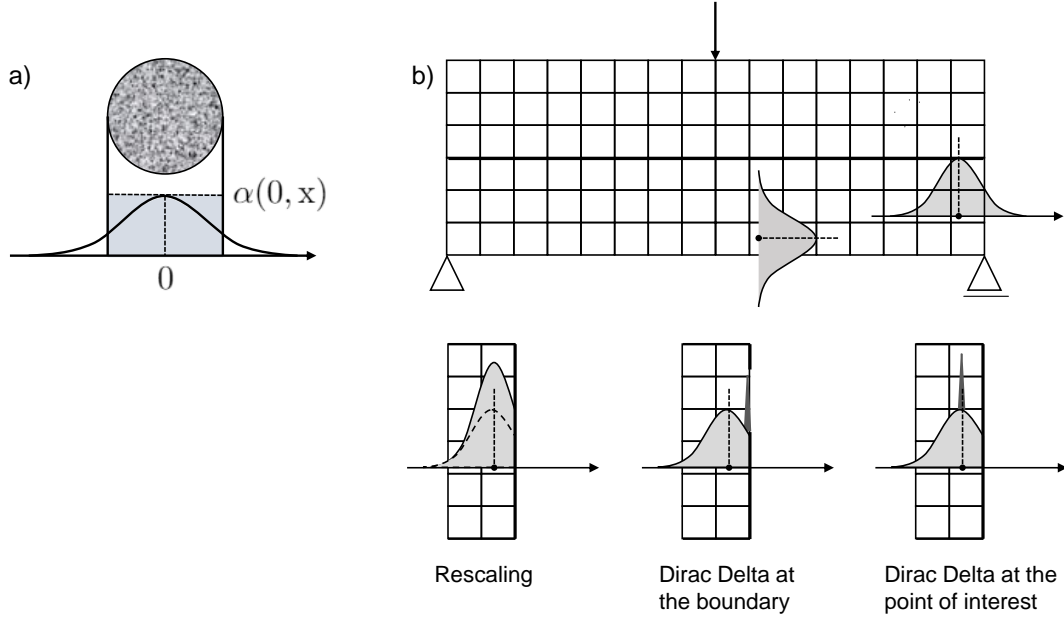


Figure 1.6: a) Nonlocal weighting function, and b) treatment of the weighting function near the structural boundaries

nonlocal weighting function.

Numerical implementation of nonlocal models has to deal with difficulties arising near the structure boundaries, where the averaging neighborhood tends to protrude outside the boundaries (Fig. 1.6b), upper). Attempts to resolve this issue include rescaling of the weighting function within the body [25] or placing a Dirac delta function either along the structural boundary, or at the center point of the nonlocal integral [38] (Fig. 1.6b), lower). However, these approaches were not based on physical arguments. The problem with the boundary can be eliminated by the nonlocal boundary layer model [16]. In this model, a boundary layer of specified thickness related to the material characteristic length is excluded from the body in which the nonlocal averaging is carried out. Other approaches are stress-based nonlocal damage models [67], which consider a non-fixed size of the averaging region, and have been extended to rate-dependent behavior as well [116]. The efficiency of nonlocal models in preventing strain localization can be undesirable in dynamic loadings, where it was shown that use of nonlocal models can lead to an overspread of the damaged region and inability of description of localized failure [55]. As a remedy to this problem, models that transition from nonlocal to local with increasing strain rate can be considered, as suggested in [55] and successfully developed in [116].

1.2.4 Phase-Field Models

Phase-field models are numerical tools for modeling fracture within the framework of continuum mechanics, and they are closely related to the variational approach to brittle fracture [63], which was introduced in order to overcome limitations of the theory of fracture mechanics. Fracture mechanics, both the linear elastic [70] as well as the nonlinear cohesive zone models [6], is not a self-contained theory in the sense that additional criteria are required to predict phenomena such as initiation of crack propagation, to estimate the crack path and to determine the onset of branching instabilities in dynamics [30]. Phase-field models, in contrast, being solely based on energy minimization, are able to automatically determine crack nucleation, growth and coalescence, without requiring an assumption of predefined cracks and without suffering from the pathological mesh dependence of other continuum approaches to fracture.

As an introduction to the phase-field models, we consider an elastic solid $\Omega \subset \mathbb{R}^{n_{\text{dim}}}$ with a set of sharp cracks $\Gamma \subset \mathbb{R}^{n_{\text{dim}}-1}$, where $n_{\text{dim}} = 1, 2, 3$ is the number of spatial dimensions (Fig. 1.7a)). The external boundary of the solid $\partial\Omega \subset \mathbb{R}^{n_{\text{dim}}-1}$, with outward unit normal vector \mathbf{n} , consists of two disjoint parts $\partial\Omega_u$ and $\partial\Omega_t$, i.e., $\partial\Omega_u \cap \partial\Omega_t = \emptyset$ and $\overline{\partial\Omega_u} \cup \overline{\partial\Omega_t} = \partial\Omega$, subjected to prescribed displacements $\mathbf{u}^*(\mathbf{x})$ for $\mathbf{x} \in \partial\Omega_u$ and tractions $\mathbf{t}^*(\mathbf{x})$ for $\mathbf{x} \in \partial\Omega_t$, where \mathbf{x} are the spatial coordinates of the material particles of the solid. Kinematics of motion of the solid are described by the displacement field $\mathbf{u}(\mathbf{x})$ and the infinitesimal strain field $\boldsymbol{\epsilon}(\mathbf{x}) := \nabla^s \mathbf{u}(\mathbf{x})$ for the symmetric gradient operator $\nabla^s(\cdot)$ with respect to \mathbf{x} . The potential energy functional of the external loads acting on the solid is given by:

$$\mathcal{P}(\mathbf{u}) = \int_{\Omega} \mathbf{b}^* \cdot \mathbf{u} \, dV + \int_{\partial\Omega_t} \mathbf{t}^* \cdot \mathbf{u} \, dA \quad (1.7)$$

where \mathbf{b}^* are the prescribed volumetric body forces.

In phase-field models, the sharp topology of cracks is regularized by a diffuse damage band of finite thickness, characterized by a scalar phase-field parameter ϕ , where $\phi = 1$ represents the cracked material and $\phi = 0$ the intact one [39, 40], as shown in Fig. 1.7b). Considering quasi-static brittle fracture of isotropic elastic solids and the regularized crack topology, the surface energy $\Psi_c(\Gamma)$ is approximated by:

$$\Psi_c(\Gamma) = \int_{\Gamma} G_c \, dA \approx \int_{\Omega} G_c \gamma(\phi; \nabla\phi) \, dV, \quad \gamma(\phi; \nabla\phi) = \frac{1}{2} \left[\frac{1}{l_0} \phi^2 + l_0 (\nabla\phi \cdot \nabla\phi) \right] \quad (1.8)$$

where G_c [J/m²] is the critical energy release rate of the material, $\gamma(\phi; \nabla\phi)$ is the crack surface density function [107], and l_0 is a length scale that determines the width of the diffuse crack. The

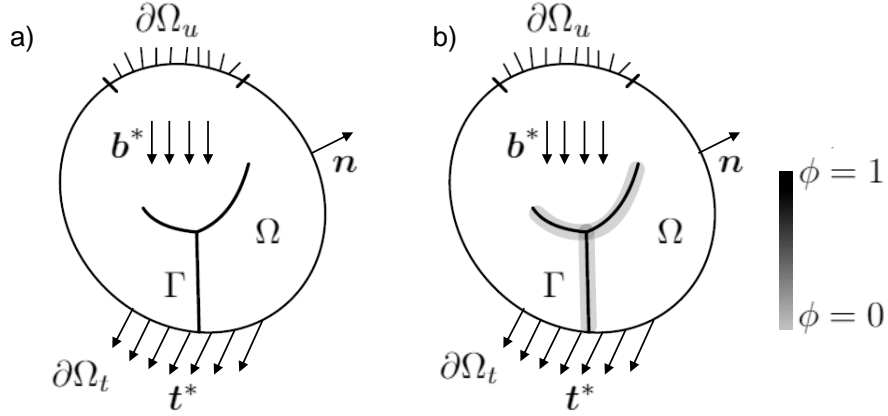


Figure 1.7: A solid body Ω with the crack set Γ : a) sharp cracks, and b) approximated diffuse crack bands

length scale l_0 , though initially treated as a purely numerical parameter, was later considered to be a material property that can be measured experimentally [110]. When $l_0 \rightarrow 0$, the solution converges to that of the original problem with the sharp crack topology according to the Γ convergence theorem [42]. It has also been shown that the results of the phase-field model can be made independent of the length scale l_0 [136] provided there is sufficient resolution of the crack phase-field, which was not the case in earlier formulations of the model. Because of the phase-field regularization of the sharp crack Γ , the stored strain energy of the elastic solid Ψ_s is a function of both the displacement field \mathbf{u} as well as the crack phase field ϕ and is expressed as follows:

$$\Psi_s(\mathbf{u}, \phi) = \int_{\Omega} g(\phi) \psi_0(\boldsymbol{\epsilon}(\mathbf{u})) \, dV \quad (1.9)$$

where $g(\phi)$ is an energetic degradation function, which leads to a decrease of the initial elastic energy density $\psi_0(\boldsymbol{\epsilon})$ with increasing values of the crack phase-field parameter ϕ . The total energy functional of the solid is thus given by:

$$\mathcal{E}(\mathbf{u}, \phi) = \int_{\Omega} g(\phi) \psi_0(\boldsymbol{\epsilon}(\mathbf{u})) \, dV + \int_{\Omega} G_c \frac{1}{2} \left[\frac{1}{l_0} \phi^2 + l_0 (\nabla \phi \cdot \nabla \phi) \right] \, dV - \mathcal{P}(\mathbf{u}) \quad (1.10)$$

The displacement field \mathbf{u} and the crack phase-field ϕ at every instant are found by minimizing the total potential energy of the cracking solid (Eq. (1.10)) subject to appropriate boundary conditions. Similar to Griffith's energetic approach to fracture, crack propagation results from the competition

between the elastic strain energy stored in the bulk material and the surface energy. On the one hand, deformations of the elastic solid due to loading increase the elastic energy. Any excess of the stored elastic energy beyond the energy required for fracture, which is the surface energy in the case of Griffith's perfectly brittle fracture considered here, will lead to crack propagation by a continuous reduction of the strain energy and a corresponding increase of the surface energy (all other dissipative mechanisms ignored) through increase of the crack phase-field ϕ towards unity. Thus, phase-field models can be regarded as solving fracture mechanics problems using partial differential equations (PDEs): basically one solves two PDEs; one for the vectorial displacement field \mathbf{u} and another one for the scalar phase-field ϕ , through alternating minimization of each field in Eq. (1.10).

Phase field models have also been developed for ductile [3, 56] and cohesive fracture [41, 104, 111, 131, 132]. In the case of ductile fracture, the stored energy functional is decomposed into elastic and plastic parts. The mechanisms of plastic deformation and crack growth may be considered either as occurring independently [3, 56], or the interaction between them can be modeled by considering the plastic energy term to affect the evolution of the crack phase-field [106]. A review of various phase-field models for ductile fracture can be found in [2]. For the case of cohesive fracture, modifications of the surface energy term are introduced so as to approximate the gradual release of fracture energy with increasing crack opening displacement, which is the essential feature of this type of failure. Extension of phase-field models to dynamics can be straightforward if the kinetic and fracture energy are assumed to be independent of the crack phase-field. Successful attempts of predicting crack branching [33] and providing quantitative estimates of the crack speed [34] have been made. However, accurate prediction of the paths of ultra-high-speed cracks requires relaxing the aforementioned assumptions and considering velocity or rate-dependent fracture energy [1] and phase-field degraded kinetic energy [44], which is a more challenging task.

Advantages of phase-field models for fracture include prediction of phenomena such as crack initiation, growth and coalescence purely from energy minimization and without any further (sometimes ad hoc) criteria required, ability to deal with the merging and branching of multiple cracks with no additional heuristics, as well as computational implementation that is straightforward in any number of dimensions. However, phase-field models are rather computationally expensive, since accurate resolution of the gradient term in Eq. (1.8) requires sufficiently fine mesh inside the damaged zone. Besides, more efforts are still required in order to make phase-field models capable of providing accurate predictions of crack tip locations. Finally, lack of representation of the displacement discontinuity caused by fracture is a drawback of phase-field models and of all continuum approaches to fracture. Nevertheless, the high performance of phase-field models in predicting complex crack

patterns, their connection to both fracture mechanics and continuum damage mechanics as well as their rigorous variational structure render them worthy of further research efforts, as also concluded in a review of phase-field models by [137].

1.3 Probabilistic Modeling of Strength Distribution of Quasibrittle Structures

The foregoing discussion focuses on deterministic analysis of quasibrittle fracture. Due to material heterogeneity, the response of quasibrittle structures is inevitably stochastic. Up to present, there have been developed three analytically tractable probabilistic models of structural failure: a) the weakest-link model, b) the fiber-bundle model, and c) the fishnet model (Fig. 1.8). The weakest-link and fiber-bundle models represent failure with damage localized into a single crack and failure with distributed cracking, respectively, whereas the recently developed fishnet model is transitional between the weakest-link and fiber-bundle models.

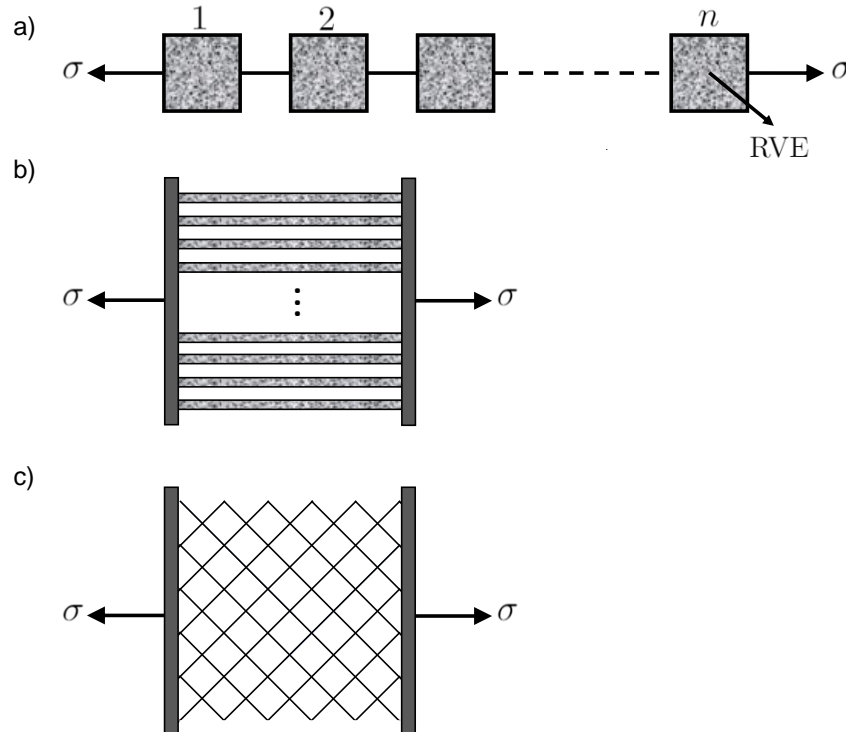


Figure 1.8: Probabilistic models of structural failure: a) chain model, b) fiber-bundle model, and c) fishnet model

1.3.1 Chain Model

The chain model or series coupling model (Fig. 1.8a)) statistically represents the structure as a chain of representative volume elements (RVEs), and is based on the assumption that structural failure will occur as soon as one RVE fails. It should be noted that, for strength statistics, the RVE is defined as the smallest material element whose failure causes the entire structure to fail, which is different from the definition of the RVE in the homogenization theory of continuum mechanics. Each RVE in the weakest-link model represents one of the potential fracture process zones (FPZs) inside which damage can localize and lead to global failure. In Weibull's theory of perfectly brittle structures [134], the size of the FPZ is negligible compared to the structural dimensions, therefore the number of RVEs in the weakest-link model can be considered as infinite. This hypothesis of brittleness is not obeyed in quasibrittle failure, in which the size of the fracture process zone (FPZ) becomes nonnegligible with respect to the system size and thus the number of RVEs is finite, as was considered in the finite weakest-link model [18, 90]. The assumption of the failure mechanism employed in the aforementioned weakest-link representations of the structure is applicable to structures of positive geometry, for which the stress intensity factor at constant load increases with the crack length, and thus load control conditions would lead to unstable crack propagation.

Assuming that the RVE strengths are statistically independent random variables with cumulative distribution function (cdf) P_1 , the probability distribution of the structural strength P_f can be written as follows:

$$P_f(\sigma_N) = 1 - [1 - P_1(\sigma_N)]^n \quad (1.11)$$

where n is the number of RVEs in the structure, and σ_N is a maximum load parameter with the dimension of stress. Based on Eq. (1.11), the survival probability of the structure is the joint probability of survival of all its RVEs. Recent studies on the statistics of static strength of quasibrittle structures [14, 15, 18, 90] have shown that the RVE can be statistically modeled by a hierarchical model, which consists of a combination of bundles and chains (Fig. 1.9a)). Each RVE represents a potential FPZ, comprising a number of subscale cracks, as shown in Fig. 1.9b). The subscale cracks which are aligned with the macrocrack direction can be considered to act approximately in parallel coupling, i.e. they are constrained to open approximately equally and simultaneously while the forces applied on them are summed. Transversely to the FPZ, the adjacent subscale cracks act approximately in series coupling, i.e. they are subjected to approximately the same force and their transverse deformations, or openings, are summed [23]. The above considerations justify the hierarchical model of the RVE. Based on the hierarchical model, it was shown that the probability

distribution of the static strength of the RVE can be approximated by a Gaussian distribution onto which a Weibull tail (or, equivalently, a power-law tail) is grafted at a fairly low probability.

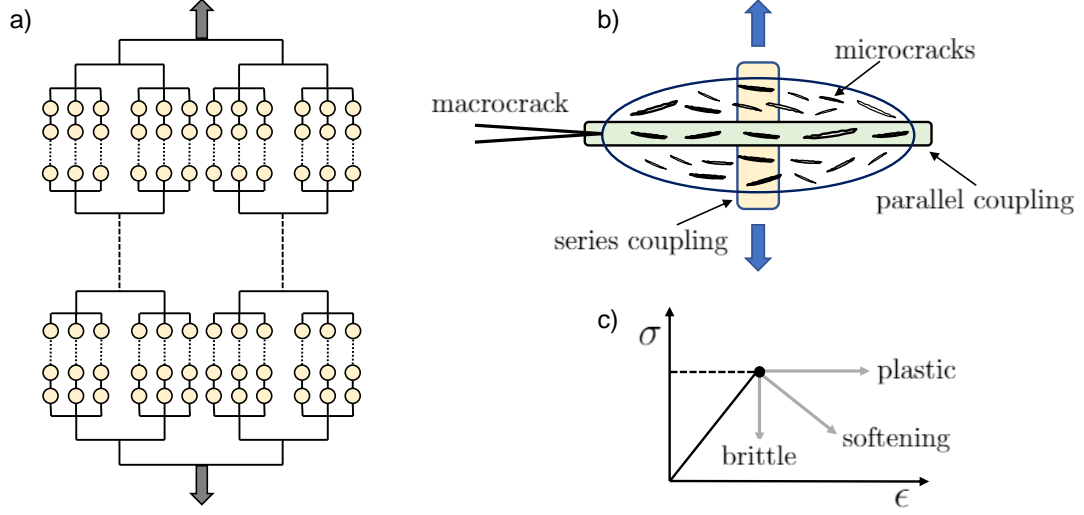


Figure 1.9: a) Hierarchical model of the RVE, b) idealization of the force transmission mechanisms inside the FPZ, and c) stress-strain diagrams of the coupled elements

The weakest-link model has the following mathematical properties which have been proven analytically [15,18,90]: If the cdfs of strength of all the elements (links) have a power-law tail of exponent m , then the cdf of strength of the entire chain has also a power-law tail of the same exponent m ; and each ten-fold increase of the number of elements in the chain extends the reach of its power-law tail in terms of failure probability by an order of magnitude, thus for sufficiently large number of links, the cdf of structural strength approaches the Weibull distribution. The latter property reflects the fact that quasibrittle structures, whose strength statistics have been realistically described by the finite weakest-link model, become perfectly brittle at the large size limit.

1.3.2 Fiber-Bundle Model

In contrast to the weakest-link model, which represents the damage localization mechanism, the fiber-bundle model represents structural failure with distributed cracking. The structure is statistically modeled by a set of elements, also called fibers, which are loaded in parallel, i.e. all fibers are subjected to the same deformation whereas the load carried by the bundle is the sum of the loads of the individual fibers (Fig. 1.8b)). Once a fiber fails, its load is redistributed among other surviving

fibers, this way preventing global failure. The maximum load of the bundle is reached when a certain fraction of the fibers breaks. Various phenomenological rules have been proposed in the literature [53, 89, 117] in order to describe the stress redistribution after the failure of a fiber. According to the equal or global load-sharing rule, the load of the failed element is equally carried by all the remaining unbroken fibers, whereas in the local load-sharing rule, only the surviving fibers in the vicinity of the failed element carry the redistributed load. Another approach is to derive the load-sharing rule by assuming a constitutive behavior (e.g. brittle, plastic, softening) of the elements in the bundle [15, 90], as shown in Fig. 1.9c).

Assuming that the strengths of the individual fibers are statistically independent random variables with probability density functions $f_i(x)$, where i denotes the i_{th} fiber, the cdf of bundle strength, which is defined as the maximum of the average bundle stress, is given by the following expression

$$G_n(S) = n! \int_{\Omega_n(S)} \prod_{i=1}^n f_i(\sigma_i) d\sigma_1 d\sigma_2 \dots d\sigma_n \quad (1.12)$$

where n is the number of fibers in the bundle model, and $\Omega_n(S)$ is the admissible region of stresses in all the fibers.

The fiber-bundle model has the following mathematical properties, which hold regardless of the constitutive behavior of its elements [126]: If the cdf of strength of each fiber has a power-law tail of exponent m_i , then the cdf of bundle strength will also have a power-law tail, with an exponent that is equal to the sum of the exponents of the power-law tails of the cdfs of fiber strengths, i.e. $\sum_{i=1}^n m_i$. The extent of the power-law tail of the cdf of bundle strength in terms of failure probability decreases with the number n of elements coupled in parallel, as described by the following relations: $P_{tn} \sim (P_{t1}/n)^n - (P_{t1}/3n)^n$ for brittle bundles and $P_{tn} \sim (P_{t1}/n)^n$ for plastic bundles [26], where P_{t1} is the failure probability at the point where the power-law tail of the strength cdf of a single fiber terminates. Another important asymptotic property of the fiber-bundle model is the convergence of the cdf of strength of sufficiently large bundles to the Gaussian distribution. This has been shown in [53] for the case of brittle bundles, whereas for plastic bundles it is a consequence of the central limit theorem, since the strength of a plastic bundle is the sum of strengths of all the fibers. The latter property leads to the conclusion that the cdf of strength of ductile structures should follow the Gaussian distribution, since in ductile failure the structural strength is a weighted sum of the strengths of all the material elements along the failure surface.

1.3.3 Fishnet Model

Both the hierarchical model of the RVE strength used in the finite weakest-link model as well as the fiber-bundle model are based on simplified assumptions of the load transmission and redistribution mechanisms inside the FPZ, which are necessary for the mathematical formulation of the probability distribution of structural strength. In the recently developed fishnet probabilistic model [99,101,102], which aimed to describe the strength distribution of nacreous materials, but was also shown able of capturing the lower tail of failure probability of quasibrittle materials such as concrete or fiber composites, the force transmission mechanism of the structure is modeled as a fishnet with diagonally pulled links (Fig. 1.8c)). The links were initially considered as perfectly brittle, though in subsequent formulations the fishnet model was generalized to links exhibiting a gradual softening postpeak behavior (Fig. 1.9c)).

In contrast to the weakest-link model, which assumes that global failure will occur as soon as a single link, the weakest one, fails, the fishnet model considers that several links can fail prior to reaching the maximum load. Thus, the survival probability of the structure $1 - P_f(\sigma)$ at a prescribed load σ can be expressed as the probability of the union of disjoint events, each one representing survival under different number of failed links, as follows:

$$1 - P_f(\sigma) = P_{s_0}(\sigma) + P_{s_1}(\sigma) + P_{s_2}(\sigma) + \dots \quad (1.13)$$

where $P_{s_k}(\sigma)$ represents the survival probability of the entire fishnet under load σ for the case when there have been exactly k failed links. For a two-dimensional fishnet consisting of r rows and q columns of links ($n = r \times q$), whose strengths are independent and identically distributed (i.i.d.) random variables with cdf $P_1(\sigma)$ following the Gauss-Weibull grafted distribution, the first term in Eq. (1.13) is the same as the finite weakest-link model and equals $[1 - P_1(\sigma)]^n$, whereas the remaining series terms differentiate the fishnet model from the weakest-link model. The terms $P_{s_k}(\sigma)$ with $k > 0$ can be calculated as the joint probability of failure of k number of links at load σ , and survival of the $n - k$ links under the corresponding level of applied load, which takes into account the stress redistribution caused by the damages. For instance, for $k = 1$, P_{s_1} has the following expression:

$$P_{s_1} \simeq nP_1(\sigma) [1 - P_1(\sigma)]^{n-\nu-1} [1 - P_1(\eta\sigma)]^\nu \quad (1.14)$$

where it is assumed that ν number of links in the vicinity of the failed link will carry the redistributed stress $\eta\sigma$, whereas the remaining $n - \nu - 1$ will survive under the prescribed load σ . The analytical

expressions of the terms corresponding to $k \geq 2$ are rather complicated, but for brittle fishnets and for not unusually large coefficient of variation of the link strengths, these higher terms are not required since the peak load is reached when only a few links have failed. However, in the case of links exhibiting a general softening behavior, the number of failed elements prior to the peak load increases with decreasing brittleness of the links and thus truncating the series of Eq. (1.13) up to the first few terms because of the difficulty of calculating the stress redistribution history for the higher-order terms, cannot provide a reliable approximation of the survival probability of the entire fishnet.

For this reason, a realistic and more computationally efficient approximation of the failure probability of fishnets with softening links was introduced in [100], by using the order statistics. More specifically, it was considered that the maximum load of the structure is determined by the k th weakest link, where k is a discrete random variable characterizing the extent of damage prior to structural failure. The failure probability of the structure is then expressed as:

$$P_f(\sigma) = \mathbb{P}(\sigma_{\max} \leq \sigma) = \sum_{k=0}^n \mathbb{P}(n_c = k) W_k(\gamma_k \sigma) \quad (1.15)$$

where n_c is the number of failed links just before the peak load is reached, $W_k(x)$ is the cdf of strength of the k th smallest minimum (k th order statistics), and γ_k is the average stress concentration factor, which depends on k . It has also been shown in [102] that the series expansion of Eq. (1.13) and the approach using order statistics, Eq. (1.15), are equivalent at the lower tail of the structural failure probability.

The fishnet shape, i.e., the width-to-length aspect ratio, where the length is measured in the direction of the applied tensile loading, is particularly important for the probability distribution of its strength. Increasing the aspect ratio from 0 to ∞ , the fishnet gradually transitions from the weakest-link model to the fiber-bundle model, which represent its limiting cases. However, in contrast to the finite weakest-link model, in the fishnet model there is no fixed-size RVE, and the predicted size effect is similar, but different from the Type I quasibrittle size effect described by the finite weakest-link model. The main drawback of the fishnet model is that it requires the calculation of stress redistributions after breakages of the links, a calculation which becomes intractable as the number of failed links prior to the peak load increases.

1.4 Research Outline

Despite the development of several successful numerical techniques to mitigate the spurious mesh sensitivity of FE simulations of softening continua, known as the localization limiters, the mesh dependence issue continues to attract significant research interest, as an essential part of the overarching goal to continue improving the computational efficiency and reliability of numerical models of failure and aid the design of safer structures. The highly sophisticated localization limiters, such as nonlocal integral or gradient-type models, have been mostly used for academic applications, whereas commercial codes use predominantly the simplest localization limiter, that is the crack band model, owing to its convenient implementation and low computational cost.

An important limitation of the widely-used crack band model, as already discussed, is that its ability to recover mesh-objective structural response is limited to cases of failure with severe strain localization. However, failure of quasibrittle structures can manifest a complex damage process, which may include a transition between localized and diffused damage patterns. Moreover, conditions that may suppress strain localization (e.g. high strain-rate loading) render the crack band model and generally localization limiters less appropriate. It is thus clear that a general approach for addressing the issue of mesh dependence should be tied to the actual spatial and temporal evolution of damage pattern in a structure, which is one of the motivations of the current study.

In Chapter 2, we focus on FE simulations of softening continua in the deterministic setting, and propose an energy regularization method that adjusts the constitutive law according to the current level of damage localization, as described by a numerical parameter referred to as the localization parameter. The method is cast into an isotropic damage model, and is further extended to rate-dependent behavior. The model is shown to be efficient in mitigating mesh dependence of the global structural response, by its application to FE simulations of both static and dynamic failures of ceramic specimens. Even though the proposed energy regularization scheme is applied to an isotropic continuum damage mechanics model suitable for tension-governed failure, extensions of the model to account for anisotropy, mixed-mode failure, and more complicated constitutive behaviors can be pursued in the future.

The present research is further extended in the stochastic setting, since it is known that the properties of quasibrittle materials could exhibit a significant degree of spatial variability. Effective discretization of the random fields of constitutive properties of a given material while preserving their original probability distribution and correlation structure is an issue which has been extensively studied in the literature [65,71,129]. In contrast, in this study, we shift our attention to a mechanistic-

based representation of the randomness of finite element properties, which takes into account both the inherent variability as well as the failure pattern of the considered element. Since focus is placed on the use of mesh sizes larger than the autocorrelation lengths of the underlying random fields, the apparent fracture properties of different finite elements can be considered as statistically independent random variables, and can thus be fully defined by their input probability distributions. This approach constitutes a more efficient method, since it allows use of large element sizes, and it also offers the benefit of retaining the same spatial discretization for both the mechanical problem as well as the modeling of randomness of fracture properties, in contrast to stochastic FE methods. However, it is important to take into account the size effects on the sampling probability distributions of fracture properties that can arise due to the failure mechanism of an element, otherwise localization of strains into the weakest elements will lead to the output probabilistic structural response be dependent on the spatial discretization, as explained in Section 1.1.

Different probabilistic models of failure have been developed for the various failure mechanisms of quasibrittle structures (Section 1.3). The models capture the size effects on the strength statistics. Even though the described failure models consider statistically independent strengths of their elements, they are able to partially account for the presence of correlations in the system through their assumptions or approximations of the load redistribution mechanism after local failures. However, given that the structural failure mechanism cannot generally be known a priori, the numerical parameters describing the evolving damage pattern introduced in our energy regularization scheme, are also used to determine the sampling distribution functions of the constitutive properties. In this way, a general probabilistic model of apparent fracture properties is developed in Chapter 4, which can transition from a weakest-link model representation of structural failure in cases of damage localization, to a fiber-bundle model in cases of distributed damage. Insight for the formulation of this model is gained by stochastic discrete element simulations of the size effects on the statistics of structural strength of ceramic specimens experiencing different failure mechanisms, triggered by loading with a wide range of applied tensile strain rates (Chapter 3). The probabilistic model is applied to continuum stochastic FE simulations of quasibrittle structures experiencing different failure mechanisms. The simulation results show that the model can effectively mitigate mesh dependence of the predicted first and second statistical moments of structural strength. The probabilistic model is intimately tied with the proposed energy regularization scheme and is not based on any assumptions for the structural failure mechanism. Therefore, the present research contributes to the development of a general and unified framework for addressing the mesh dependence of continuum FE simulations of quasibrittle failure, in both deterministic and stochastic settings.

Chapter 2

Energy Regularization in Deterministic Numerical Simulations of Strain-Softening Continua

As discussed in Chapter 1, the strain-softening behavior of quasibrittle materials can lead to localization instability and the spurious mesh sensitivity of finite element simulations. Energy regularization methods in the concept of the crack band model [17] are based on the assumption of a fully localized damage pattern, which occurs as soon as the peak load of the structure is reached. However, depending on the loading configuration and structural geometry, quasibrittle structures can exhibit a complex damage process, which may involve both localized and diffused damage patterns. In this chapter, a generalized energy regularization method, that considers the spatial and temporal evolution of the internal damage variable, is presented. The method introduces a localization parameter, which describes the local spatial distribution of damage at every time step, and can capture the transition from diffused to localized damage during the failure process. It is the localization parameter that governs the energy regularization of the constitutive model, obviating the need for any a priori knowledge of the failure mechanism of the structure. The method is cast into an isotropic damage model, and is further extended to rate-dependent behavior. The efficiency of the model in mitigating mesh dependence is shown by its application in finite element simulations of both static and dynamic tension-governed failure of quasibrittle specimens. The simulation results demonstrate the essential role of mechanism-based energy regularization of constitutive relation in continuum

finite element modeling of quasibrittle fracture.

2.1 Model Formulation

The proposed energy regularization scheme is incorporated into an isotropic continuum damage mechanics model [83, 94, 119], which is represented in general form by

$$\boldsymbol{\sigma} = f(\omega)\mathbf{C} : \boldsymbol{\epsilon} \quad (2.1)$$

where \mathbf{C} denotes the elastic stiffness tensor, ω is the damage variable ranging from 0 (virgin state) to 1 (fully damaged state), $\boldsymbol{\epsilon}$ is the infinitesimal strain tensor, and $f(\omega)$ is a damage function, which describes stiffness degradation of the material. The function $f(\omega)$ has a maximum value of one at $\omega = 0$, and a minimum value of zero at $\omega = 1$. Meanwhile, $f(\omega)$ must also be monotonically non-increasing, i.e. $df/d\omega \leq 0$. The damage parameter represents a state variable, which can be related to the strain tensor. The core of continuum damage models largely lies in the formulation of this relationship. In this study, the damage evolution equation is formulated by linking damage mechanics with fracture mechanics through an energy regularization scheme.

Considering a finite element with linear shape functions and a given Gauss point inside its domain, let \vec{n}_g denote a unit vector perpendicular to the crack plane. The crack plane is assumed to be perpendicular to the direction of the maximum principal tensile strain at the onset of damage, and is considered to have a fixed orientation throughout the damage process - fixed crack model - even though the principal strain directions can change during loading. The dimension of the element projected in the direction of \vec{n}_g is denoted as h_1 , and h_2 denotes the corresponding dimension in the direction orthogonal to h_1 . It is noted that, inside a given element, each Gauss point may have a different \vec{n}_g , and therefore the corresponding length h_1 , which physically represents the crack band width, may also differ among Gauss points of the same element. Various numerical estimates of the crack band width have been proposed in the literature, and the performance of the crack band model [17] in addressing the mesh dependence of finite element simulations when using different estimates of the localization bandwidth can vary significantly [79]. The modified projection method [79], which considers a single value of h_1 for all Gauss points of an element based on the principal values of its average strain tensor, could also have been used in the present model. Besides, the estimate of the crack band width h_1 should also take into account the order of approximation of the displacement field, since for higher order shape functions, damage could localize into a single

Gauss point [79], but in this study we limit our focus to linear elements.

In order to derive the damage evolution law by employing fracture mechanics, it is not unduly restrictive to consider that ωh_2 represents the crack length a , which is similar to a common definition of the damage variable in continuum damage mechanics [83]. The energy required (per unit thickness) for advancement of a crack by distance δa is equal to $G_f h_2 \delta \omega$, where G_f represents the mode I fracture energy, since this study focuses on tensile damage. Crack advancement is made possible through the release of energy from the entire element during an increment of damage $\delta \omega$, which can be written as $h_1 h_2 \delta U$, where U represents an energy potential governing tensile failure. Considering quasi-static crack propagation, and fracture as the only energy dissipation mechanism, the energy balance equation in the limit of $\delta \omega \rightarrow 0$ can be written as follows:

$$\frac{\partial U}{\partial \omega} + \frac{G_f}{h_1} = 0 \quad (2.2)$$

Evidently, Eq. (2.2) is based on the assumption that the damage of the element is manifested by a single crack (Fig. 2.1a)). This corresponds to the damage localization mechanism. Eq. (2.2) indicates that the constitutive relation varies with the mesh size h_1 .

On the other hand, if the element experiences diffused damage (Fig. 2.1b)), there would be h_1/h_0 number of cracks propagating together, where h_0 = width of the fracture process zone (FPZ). Note that h_0 is a material length scale, which, under quasi-static loading, is typically on the order of two to three times the size of material heterogeneity. In this case, the energy balance equation becomes

$$\frac{\partial U}{\partial \omega} + \frac{G_f}{h_0} = 0 \quad (2.3)$$

In contrast to Eq. (2.2), Eq. (2.3) suggests a mesh-independent constitutive behavior. To further explain this difference, we emphasize that the constitutive model of a single finite element describes the behavior of a material element of finite size. In the case of localized damage, only the material inside the damage zone experiences cracking, which is manifested by strain softening, whereas the material outside the damage zone undergoes unloading. Since the size of the damage zone is a material constant, a larger material element implies a larger unloading zone. Consequently, the overall mechanical behavior of the material element is dependent on the element size. In the case of diffused damage, the entire material element experiences the same softening damage, and therefore the mechanical behavior of the element is independent of its size.

Based on the foregoing discussion, it is evident that Eqs. (2.2) and (2.3) correspond to two distinct damage mechanisms. In some cases, such as a pre-notched specimen, Eq. (2.2) can directly be applied

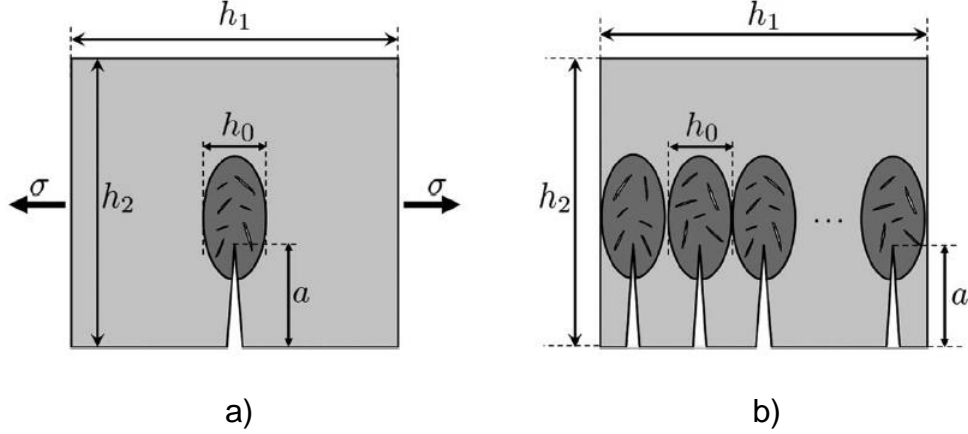


Figure 2.1: Two distinct crack patterns in a material element represented by a finite element: a) localized cracking, and b) diffused cracking

since damage localization occurs right away. However, in other cases, the damage process involves the transition from diffused to localized damage, and the onset of this transition is not known a priori. Therefore, a general energy regularization method is required, which can automatically adjust the constitutive model as the damage pattern evolves. To formulate such a method, the key step is to determine the localization level from the evolving damage pattern. In recent studies, an estimate for the onset of localization was calculated based on the spatial fluctuations of the damage variable [31, 92]. However, in these studies, the formulation is either in a one-dimensional setting [31] or does not consider the direction of damage propagation [92]. Here we develop an improved formulation based on the concept proposed in [92].

Considering a finite element labeled by i , let \vec{v}_{ij} denote the vector that connects the centroid of element i with the centroids of its neighboring elements j (Fig. 2.2). For any given Gauss point of element i , we determine the connection vectors that maximize and minimize the product $(\vec{n}_g \cdot \vec{v}_{ij})/|\vec{v}_{ij}|$, and denote them by \vec{v}_{m1} and \vec{v}_{m2} , respectively. It is clear that these two vectors represent the directions of the two adjacent elements that most closely align with the direction of the maximum principal strain of the Gauss point. We then define a localization parameter δ_ω for

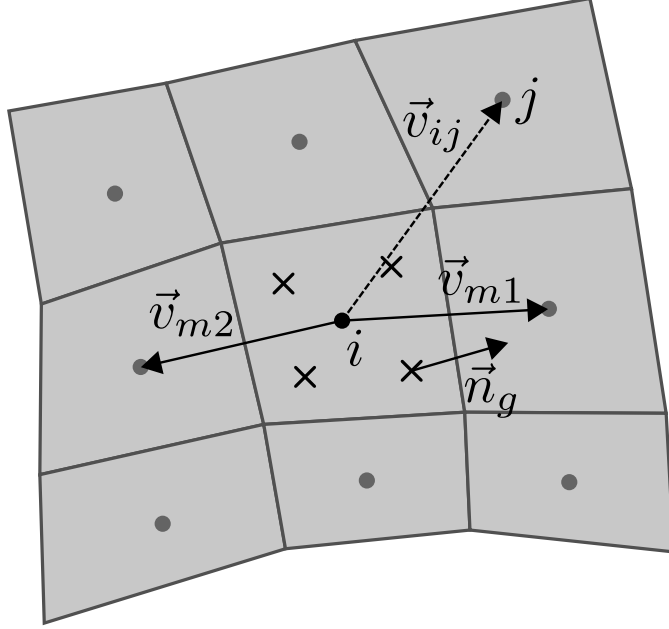


Figure 2.2: Schematic of finite element mesh for defining the localization parameter

the Gauss point as

$$\delta_\omega = \begin{cases} \left\langle 1 - \frac{\bar{\omega}_{i1} + \bar{\omega}_{i2}}{2\bar{\omega}_i} \right\rangle^2 & \text{when } \bar{\omega}_i > 0 \\ 0 & \text{when } \bar{\omega}_i = 0 \end{cases} \quad (2.4)$$

where $\langle x \rangle = \max(x, 0)$, $\bar{\omega}_i$ = average damage value of element i , and $\bar{\omega}_{i1}, \bar{\omega}_{i2}$ = average damage values of the two adjacent elements that are along the directions of \vec{v}_{m1} and \vec{v}_{m2} . Eq. (2.4) indicates that the localization parameter is governed by the relative difference between the damage of element i and the average damage of its adjacent elements along the directions of \vec{v}_{m1} and \vec{v}_{m2} . It is evident from Eq. (2.4) that δ_ω has a minimum value of zero, which corresponds to the case of a uniform distribution of damage or the case where the damage level of element i is lower than the average damage level of its adjacent elements. δ_ω has a maximum value of one, which corresponds to the case of a fully localized damage pattern.

By introducing the localization parameter, we now propose a general energy regularization equa-

tion for each Gauss point:

$$\frac{\partial U}{\partial \omega} + \frac{G_f}{h_0} g(\delta_\omega) = 0 \quad (2.5)$$

where we assume function $g(\delta_\omega)$ to have the following form:

$$g(\delta_\omega) = 1 + \left(\frac{h_0}{h_1} - 1 \right) \delta_\omega^\kappa \quad (2.6)$$

where $\kappa = \text{constant}$. It is clear that Eq. (2.5) converges to Eq. (2.2) and Eq. (2.3) for the case of localized damage ($\delta_\omega = 1$) and diffused damage ($\delta_\omega = 0$) respectively, regardless of the selected value for κ . Exponent κ governs the transition between these two fundamental failure mechanisms as a function of δ_ω .

In this study, we choose a form of the free energy function suitable for tension dominated failure. A simple choice is to consider the concept of equivalent strain, which has been widely used in tension-governed continuum damage models [92, 105]:

$$U = \frac{1}{2} f(\omega) E \bar{\epsilon}^2 \quad (2.7)$$

$$\text{where } \bar{\epsilon} = \sqrt{\sum_{k=1}^3 \langle \epsilon_k \rangle^2} \quad (2.8)$$

E = Young's modulus of the material, $\bar{\epsilon}$ = equivalent strain, and ϵ_k = the principal values of the strain tensor. Note that the damage function in Eq. (2.7) is a natural consequence of the present isotropic damage model (Eq. (2.1)). Substitution of Eq. (2.7) into Eq. (2.5) yields an evolution equation of the damage function that is compatible with fracture mechanics:

$$\frac{df(\omega)}{d\omega} = -\frac{2G_f}{h_0 E \bar{\epsilon}^2} g(\delta_\omega) H(\bar{\epsilon} - \epsilon_0) H(\dot{\bar{\epsilon}}) \quad (0 \leq \omega < 1) \quad (2.9)$$

where $H(x)$ = Heaviside function, ϵ_0 = threshold strain, and $\dot{\bar{\epsilon}} = d\bar{\epsilon}/dt$. Eq. (2.9) gives the energy-based evolution law of the damage function, in which the energy regularization is governed by the localization parameter. Note that the two Heaviside functions in Eq. (2.9) indicate that 1) damage would not grow if $\bar{\epsilon} \leq \epsilon_0$, and 2) damage would not grow if the material experiences tensile unloading. Note that, based on Eq. (2.1), function $f(\omega) = 0$ when $\omega = 1$, and therefore we have $df(\omega)/d\omega = 0$ when $\omega = 1$.

The original crack band model [17] applicable for localized damage was anchored by the preservation of fracture energy (i.e. the product of the fracture energy density times the element size is

set equal to the material fracture energy) [8, 15, 19]. In some cases, though, it can be hard to assess which constitutive parameters should be adjusted based on the mesh size so as to recover mesh objective simulation results. In the present model, there is no need for such an insight, since the energy regularization is carried out by adjusting the point-wise tangential stiffness tensor through Eq. (2.9).

The constitutive model is completed by combining Eq. (2.9) with an explicit form of the damage function $f(\omega)$, which in this study is assumed to be (e.g. [97, 135])

$$f(\omega) = \frac{1 - \omega}{1 - a\omega} \quad (2.10)$$

where a = model parameter that is directly related to the material tensile strength f_t , not to be confused with the crack length a for which the same notation was used. To reveal this relationship, we consider the case of monotonic uniaxial tension with applied strain ϵ . By differentiating Eq. (2.10) with respect to the damage variable and combining it with Eq. (2.9), we obtain the following relationship between the damage variable and the strain for $\epsilon \geq \epsilon_0$:

$$\omega = \frac{1}{a} - \frac{\epsilon}{a} \sqrt{\frac{h_0 E (1 - a)}{2 G_f g(\delta_\omega)}} \quad (2.11)$$

The condition of threshold strain ($\omega = 0$ at $\epsilon = \epsilon_0^+$) yields:

$$a = 1 - \frac{2 G_f g(\delta_\omega)}{h_0 E \epsilon_0^2} \quad (2.12)$$

Threshold strain ϵ_0 can be determined by investigating the tangential stiffness at $\epsilon = \epsilon_0^+$:

$$\left. \frac{d\sigma}{d\epsilon} \right|_{\epsilon_0^+} = \left(1 + \left. \frac{df(\omega)}{d\epsilon} \right|_{\epsilon_0^+} \right) E = E/a \quad (2.13)$$

Here we consider that the stress-strain response exhibits a softening response right after ϵ_0^+ , which implies $a < 0$. In this case, ϵ_0 must correspond to the material tensile strength f_t , i.e. $\epsilon_0 = f_t/E$, and Eq. (2.12) becomes:

$$a = 1 - \frac{2 l_{ch} g(\delta_\omega)}{h_0} \quad (2.14)$$

where $l_{ch} = EG_f/f_t^2$ = Irwin characteristic length. Eq. (2.14) indicates that the damage function (Eq. (2.10)) is directly related to the localization parameter. For the case of localized damage, the damage function explicitly depends on the mesh size, h_1 , whereas for the case of diffused damage it

does not. Fig. 2.3 shows the uniaxial tensile stress-strain curves for material elements of different sizes for the case of localized damage. As seen, in this case the present model recovers the original crack band model. Note that, due to the limit $a < 0$, Eq. (2.14) suggests a maximum element size that can be used in the FE simulation: $h_m = 2l_{ch}$. If the element size is larger than h_m , the post-peak tangential stiffness would become positive indicating a snap-back behavior.

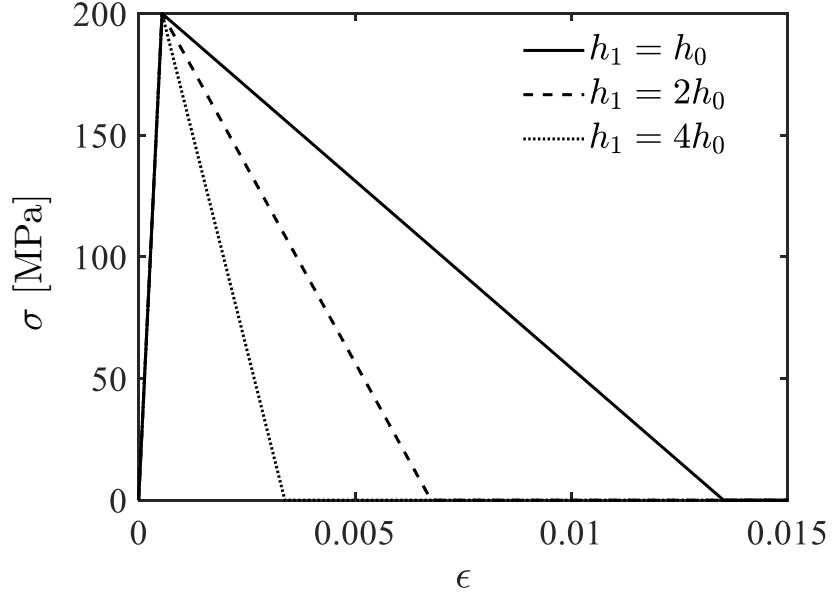


Figure 2.3: Uniaxial tensile stress-strain curves for different mesh sizes for the case of fully localized damage

2.2 Extension to Rate-Dependent Behavior

We now extend the model to dynamic tensile failure of quasibrittle materials. One way to capture the rate effect on the constitutive behavior is through a kinetics model of damage growth [86]. Within the present modeling framework, it is essential to incorporate the energy regularization scheme into the formulation of the damage kinetics model, which can be applied to any arbitrary loading path. The simplest way is to derive an equation for the damage growth rate directly from Eq. (2.9). To this end, we introduce the rate dependence of the fracture energy and crack band width.

It is well documented that many quasibrittle materials exhibit a rate enhancement of fracture

energy [32,121,128]. In this study, we consider the following rate dependence on the fracture energy

$$G_f^d(\dot{\omega}) = G_f \exp[a_1(\dot{\omega}/\dot{\omega}_0)] \quad (2.15)$$

where a_1 = model constant, $\dot{\omega} = d\omega/dt$ = damage growth rate, and $\dot{\omega}_0$ = reference damage growth rate, which is defined as $\dot{\omega}_0 = C_R/l_{ch}$, where C_R = the Rayleigh wave speed = $(0.862 + 1.14\nu)\sqrt{E/2\rho(1+\nu)^3}$ (ν = Poisson ratio, and ρ = material density).

The consideration of the rate effect on the crack band width is motivated by recent discrete element simulations of dynamic fracture of ceramic specimens. The simulations showed that the spacing of distributed cracks, which is a measure of the crack band width, decreases with an increasing strain rate [91]. Therefore, we consider the following rate dependence on the crack band width:

$$h_0^d(\dot{\omega}) = h_0 \exp[-a_2(\dot{\omega}/\dot{\omega}_0)] \quad (2.16)$$

where a_2 = model constant. By considering $\dot{\omega}_0$ as the maximum damage growth rate, the minimum crack band width predicted by Eq. (2.16) equals $h_0 \exp(-a_2)$. Under quasi-static loading, the crack band width is about three times the maximum size of material heterogeneities [19]. It is reasonable to consider that, under high loading rate, the minimum crack band width is about the maximum size of material heterogeneities. Therefore, we have $a_2 \approx 1.1$. It should be mentioned that the present model does not consider comminution and fragmentation of material heterogeneities. Nevertheless, the effect of material comminution and fragmentation can be taken into account by introducing an additional energy dissipation term to the constitutive model [9,10].

The rate-dependent fracture energy and crack band width are incorporated into the evolution equation of the damage function (Eq. (2.9)) as well as the function g (Eq. (2.6)). As a result, we obtain a rate-dependent evolution equation of the damage function:

$$\frac{df(\omega)}{d\omega} = -\frac{2G_f \exp[(a_1 + a_2)(\dot{\omega}/\dot{\omega}_0)]}{h_0 E \bar{\epsilon}^2} g^d(\delta_\omega, \dot{\omega}) \quad \text{for } \bar{\epsilon} \geq \epsilon_0 \text{ and } \dot{\bar{\epsilon}} > 0 \quad (2.17)$$

where $g^d(\delta_\omega, \dot{\omega}) = 1 + [h_0^d(\dot{\omega})/h_1 - 1] \delta_\omega^\kappa$. However, the model parameter a is considered to be affected only by the rate dependence of the localization parameter, i.e. $a(\delta_\omega, \dot{\omega}) = 1 - 2l_{ch}g^d(\delta_\omega, \dot{\omega})/h_0$. By combining Eq. (2.17) with the assumed damage function $f(\omega)$ (Eq. (2.10)), we have

$$\frac{1}{(1 - a\omega)^2} = \exp[(a_1 + a_2)(\dot{\omega}/\dot{\omega}_0)] \left(\frac{\epsilon_0}{\bar{\epsilon}}\right)^2 \quad \text{for } \bar{\epsilon} \geq \epsilon_0 \text{ and } \dot{\bar{\epsilon}} > 0 \quad (2.18)$$

When using an explicit numerical scheme with a small time step, we may consider that the

localization parameter is evaluated based on the damage state calculated in the previous step, and therefore can be kept constant during the current time step. Based on Eq. (2.18), the damage growth rate for the current time increment can then be calculated as

$$\dot{\omega} = \frac{\dot{\omega}_0}{a_1 + a_2} \ln \left\{ \frac{1}{[1 - a(\delta_\omega^0, \dot{\omega}^0)\omega]^2} \frac{\bar{\epsilon}^2}{\epsilon_0^2} \right\} H(\dot{\epsilon})H(\bar{\epsilon} - \epsilon_0) \quad (0 \leq \omega < 1) \quad (2.19)$$

where $\delta_\omega^0, \dot{\omega}^0$ = localization parameter and damage rate calculated in the previous time step, respectively. Note that Eq. (2.19) indicates a zero damage growth rate at $\bar{\epsilon} = \epsilon_0^+$, which ensures the continuity of the damage growth function. Eq. (2.19) is further supplemented by the condition that $\dot{\omega} = 0$ when $\omega = 1$. The combination of Eq. (2.19) and Eq. (2.10) completes the rate dependent constitutive model.

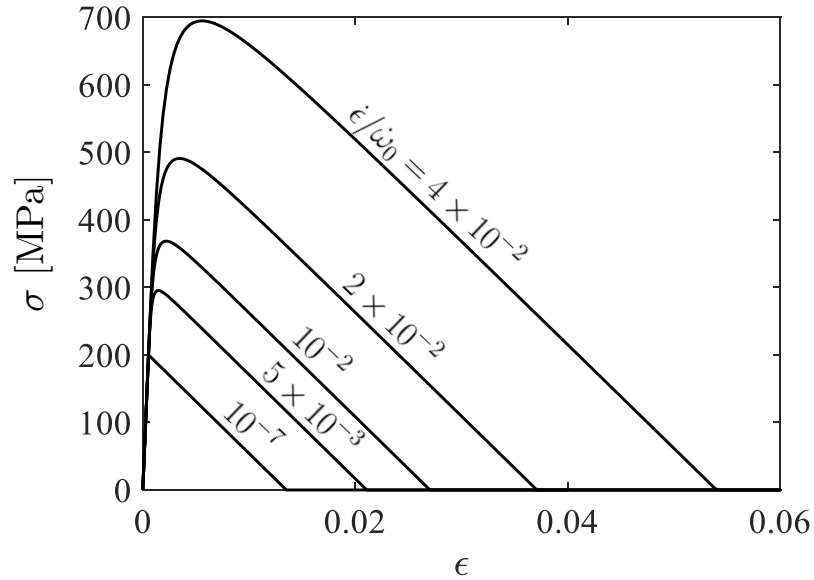


Figure 2.4: Rate-dependent uniaxial tensile stress-strain behavior of a material element for the case of fully diffused damage

To demonstrate the constitutive behavior described by the present model, we consider a set of model parameters for dense alumina [140]: $E = 370$ GPa, $\nu = 0.24$, $\rho = 3900$ kg/m³, $f_t = 200$ MPa, $G_f = 50$ J/m², $a_1 = 2.5$ and $a_2 = 1.1$. These parameters are also used in the subsequent simulations of quasi-static and dynamic failure. Fig. 2.4 presents the uniaxial tensile stress-strain curves of a material element with diffused damage (i.e. $g^d(\delta_\omega, \dot{\omega}) = 1$) under different uniform applied strain rates $\dot{\epsilon}$. It is seen that, for all strain rates, the stress-strain curve deviates from the initial linear elastic

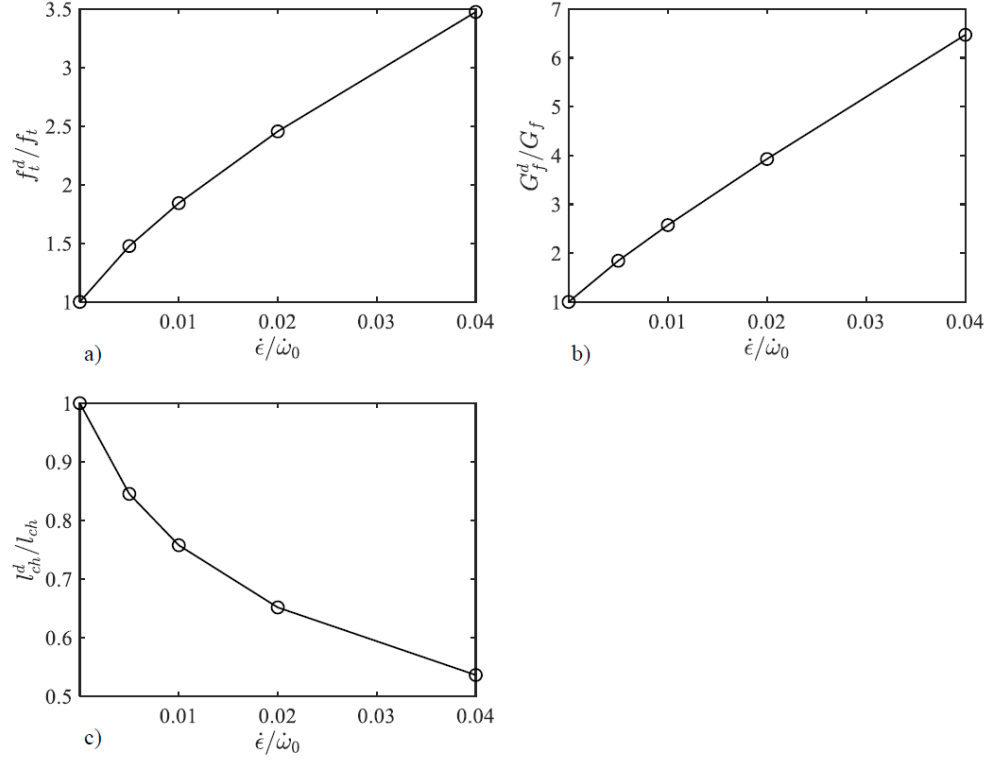


Figure 2.5: Rate effect on material properties: a) apparent tensile strength, b) fracture energy, and c) Irwin's characteristic length

response at the threshold strain ϵ_0 . At increasing strain rates, the stress-strain response exhibits a more pronounced nonlinearity before the peak strength is reached. Meanwhile, the present model predicts a rate enhancement of material tensile strength, as shown in Fig. 2.5a). Note that, for the case of constant strain-rate loading, the damage growth rate varies with time, and therefore the model does not directly yield the dependence of the fracture energy on the strain rate. Nevertheless, we may approximate this strain rate effect by using the average damage growth rate $\dot{\omega}_a = \dot{\epsilon}/(\epsilon_u - \epsilon_0)$, where ϵ_u = ultimate strain at which the stress drops to zero. Fig. 2.5b) plots this approximated strain rate effect on the fracture energy, which as expected exhibits a strong rate enhancement. The rate effects on tensile strength and fracture energy directly provide the rate dependence of Irwin's characteristic length, as shown in Fig. 2.5c). It is seen that Irwin's characteristic length, which is proportional to the FPZ length, decreases with an increasing strain rate. Such a trend has been experimentally observed in quasibrittle materials [13, 19].

2.3 Simulations of Quasi-Static Failure

Implemented in an open-source FEM software (OOFEM) [115], the present model is first applied to simulate quasibrittle fracture under quasi-static loading. We use dense alumina as a model system. The simulations consider both notched and unnotched beams subjected to three-point bending under displacement controlled loading (Fig. 2.6). The unnotched beam has a size of 7.5 mm (length) \times 2.5 mm (depth) \times 0.0375 mm (width). The notched beam has a size of 15 mm (length) \times 5 mm (depth) \times 0.0375 mm (width), and has a notch of length equal to half of the beam depth placed at the mid-span. The quasi-static crack band width is chosen as $h_0 = 37.5 \mu\text{m}$, which is about three times the maximum grain size [91].

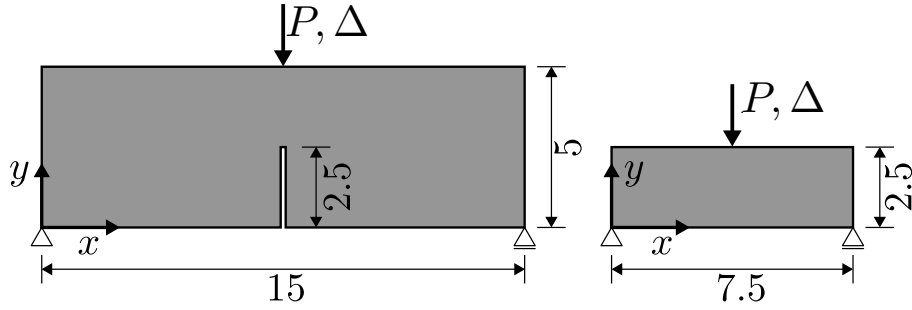


Figure 2.6: Notched and unnotched three-point bend beams considered in the simulation (all dimensions are in mm)

In the simulation, the beam is discretized with a uniform mesh of linear isoparametric brick elements, each of which contains eight Gauss integration points. The dimensions of the finite elements in the reference case are $h_x = h_0$, $h_y = 2h_0$, and $h_z = h_0$, where subscripts x, y, z denote the directions of the beam span, depth and width, respectively. In the present simulation cases, the mesh size along the direction of the maximum principal strain is approximately equal to the quasi-static crack band width h_0 . To investigate the mesh sensitivity, we consider other two mesh sizes: $h_x = 2h_0$ and $h_x = 4h_0$ while h_y and h_z are kept the same as those in the reference case. It is noted that, for the notched beam, the notch width is set to be equal to the current dimension h_x of the finite element. Therefore, the notch width varies with the element size. Nevertheless, the ratio between the notch depth and the notch width is large (on the order of 10) for all three mesh sizes, so it is expected that the effect of the notch width on the simulation results is insignificant.

For the purpose of comparison, we use three different approaches of energy regularization for each simulation case:

- I) Direct use of Eq. (2.2), which assumes damage localization in all cases.
- II) Direct use of Eq. (2.3), which assumes diffused damage in all cases.
- III) The present model, which handles diffused damage, localized damage, as well as the transition between them (Eq. (2.5)).

It is evident that approach I resembles the original crack band model [17]. Approach II implies a mesh independent constitutive model. Hereafter, we refer to approaches I and II as the localized damage model and the diffused damage model, respectively. Approach III (i.e. the present model) requires an additional parameter κ for determining the transition between different damage patterns. As will be discussed later, the κ value will be determined based on the simulation of the unnotched beam.

For the notched beam, damage localization occurs right away at the notch tip due to the stress concentration at the pre-existing notch. This is evidenced by the simulated damage pattern (Fig. 2.7). Thus, it is expected that the localized damage model would effectively mitigate the spurious mesh dependence. Meanwhile, damage localization implies that $\delta_\omega = 1$ in the present model, so regardless of the value of κ , the present model yields the same result as the localized damage model. Therefore, we do not seek to determine the optimum value of κ from the simulation of the notched beam.

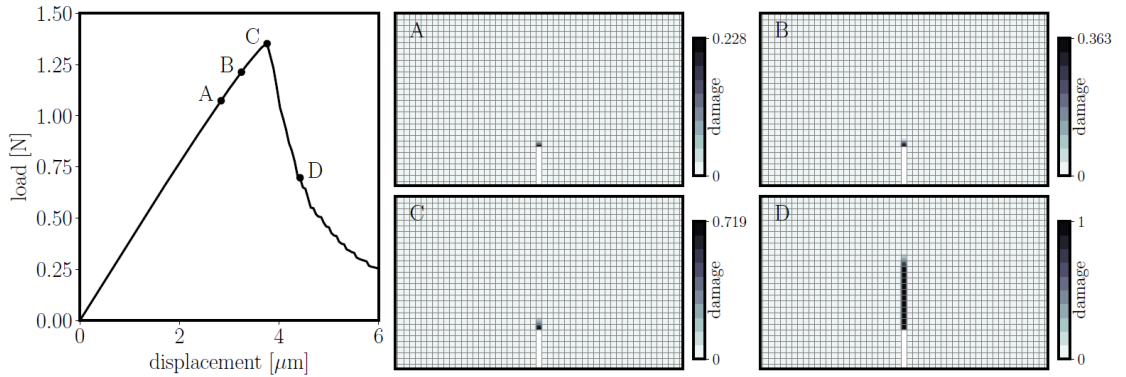


Figure 2.7: Evolution of the damage pattern of the notched beam

Fig. 2.8a) presents the simulated load-displacement curves of the notched beam using the aforementioned three approaches. It is found that the localized damage model and the present model essentially give the same results, which are independent of the mesh size. However, the diffused damage model yields a strong mesh sensitivity. When a large mesh size is chosen, the simulation predicts a significant increase in both the peak load and the total area under the load-displacement curve. This can be attributed to the fact that, for localized damage, the fixed stress-strain model implies a higher fracture energy for larger finite elements. Fig. 2.8b) shows the simulated profile of normal stress along the ligament using the diffused damage model. It is seen that, when using a larger mesh size, the FPZ becomes longer. This explains why the simulated post-peak regime for larger mesh sizes exhibits a more ductile behavior.

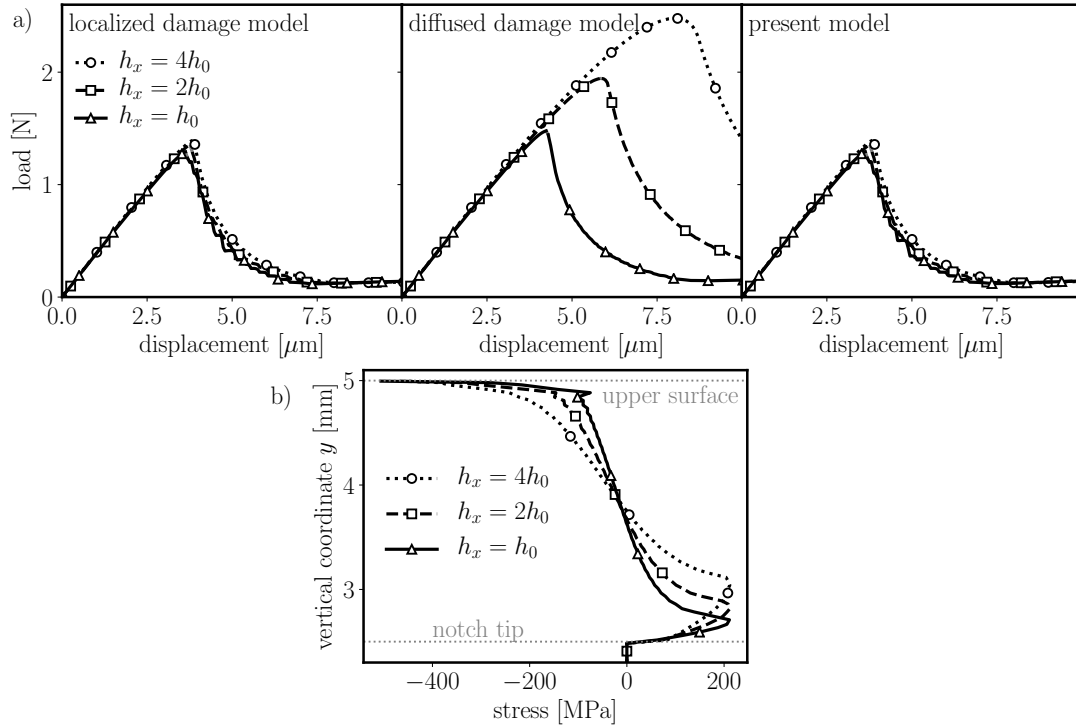


Figure 2.8: Simulation results of the notched beam: a) load-displacement curves, and b) profile of normal stress along the ligament for the diffused damage model

The failure process in the unnotched beam is more complicated. Present simulations show that all three approaches give a qualitatively similar damage evolution, which is shown in Fig. 2.9. It is clear that the beam first experiences a diffused damage pattern and gradually transitions to

localized damage featured by macrocrack propagation. Therefore, it is expected that neither the localized damage model nor the diffused damage model will be able to effectively mitigate the issue of mesh dependence. This is confirmed by the simulated load-deflection curves of the unnotched beam as shown in Fig. 2.10. It is seen that, when using the localized damage model, the simulation predicts a lower peak load as the mesh size increases. On the other hand, when using the diffused damage model, the simulation shows an opposite trend, where a larger mesh size leads to a slightly higher peak load. The mesh dependence by using the localized damage model is considerably more pronounced than that by using the diffused damage model. This indicates that the energy dissipation of distributed cracking contributes significantly to the peak load capacity. In the localized damage model, a larger mesh size underestimates the energy dissipation when a diffused damage pattern is present, and therefore it leads to a lower peak load capacity. The fact that the diffused damage model does not completely suppress the mesh sensitivity indicates that damage localization has occurred at the peak load. Similar to the foregoing analysis of the notched beam, a larger mesh would overestimate the energy dissipation for the case of localized damage and yield a higher peak load capacity.

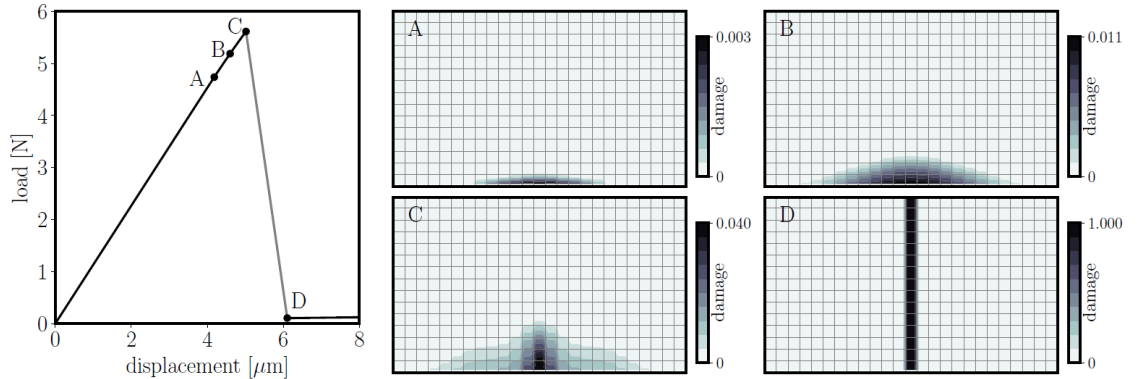


Figure 2.9: Snapshots of the damage pattern of the unnotched beam during the loading process

The opposite trends of mesh dependence of the localized damage model and the diffused damage model indicate that the present model should be able to mitigate the mesh dependence if an appropriate value of the parameter κ is chosen. It is found that $\kappa = 1$ leads to the best performance of the present model (Fig. 2.10), where the simulation result is almost insensitive to the mesh size. The essence of the proposed model is that, as the loading proceeds, the energy regularization gradually switches from Eq. (2.3) to Eq. (2.2) as damage localization emerges from distributed damage. The

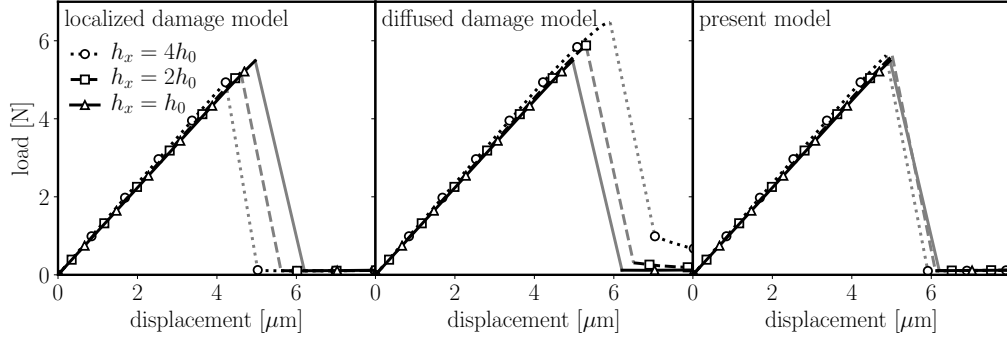


Figure 2.10: Simulated load-displacement curves of the unnotched beam

same κ value will be used in the subsequent analysis of dynamic fracture as well.

It should be mentioned that the simulations show a lack of convergent solution for part of the post-peak region (colored in grey in Fig. 2.10), which indicates a snap-back behavior. The post-peak region with the snap-back behavior includes the kinetic energy due to unstable crack propagation, and therefore cannot be directly used to investigate the effect of different energy regularization schemes on the calculated energy dissipation due to damage and fracture. Nevertheless, it is clear from Fig. 2.9 that the snap-back behavior occurs only during the propagation of a single macrocrack, and the energy dissipation of the specimen is primarily due to the energy expended for the macrocrack propagation. Therefore, it is expected that, if we are able to trace the snap-back behavior using a different loading scheme (e.g. crack-mouth opening displacement controlled test), the present model would be able to correctly capture the overall energy dissipation during this loading stage, since the localization parameter would approach the value of 1, corresponding to a localized damage pattern.

The foregoing analysis of quasi-static fracture of beams indicates that energy regularization plays an important role in mitigating mesh dependence in FE simulations. Meanwhile, energy regularization is intimately tied with the underlying damage mechanism. Neither the crack band model nor the mesh-independent local constitutive model can provide a general approach for energy regularization due to their underlying assumptions of the damage mechanism. Figs. 2.8a) and 2.10 show some promising features of the present model for overcoming the limitations of these previous models.

2.4 Simulations of the Dynamic Spalling Test

In this section, we apply the model to simulations of dynamic tensile failure of quasibrittle structures. We consider the modified split Hopkinson bar test, also known as the dynamic spalling test (Fig. 2.11a)). In this test, a compressive stress pulse is applied to one end of the bar (the left end was considered here), whereas the other end is free. As soon as the compressive stress wave reaches the free end, it will reflect as a tensile wave and travel back into the bar, causing tensile damage (Fig. 2.11b)). Depending on the amplitude and duration of the compressive stress pulse, the spalling test can produce high strain rates, e.g. up to the order of $10^2/\text{s}$ for concrete, or even up to the order of $10^4/\text{s}$ for higher strength materials, such as ceramics [62]. One important measurement of the spalling test is the time history of the velocity of the free end. It has been suggested that the difference between the peak velocity and the rebound velocity, also referred to as the pullback velocity, can be used to estimate the intrinsic dynamic tensile strength of the material [60, 76, 98, 128].

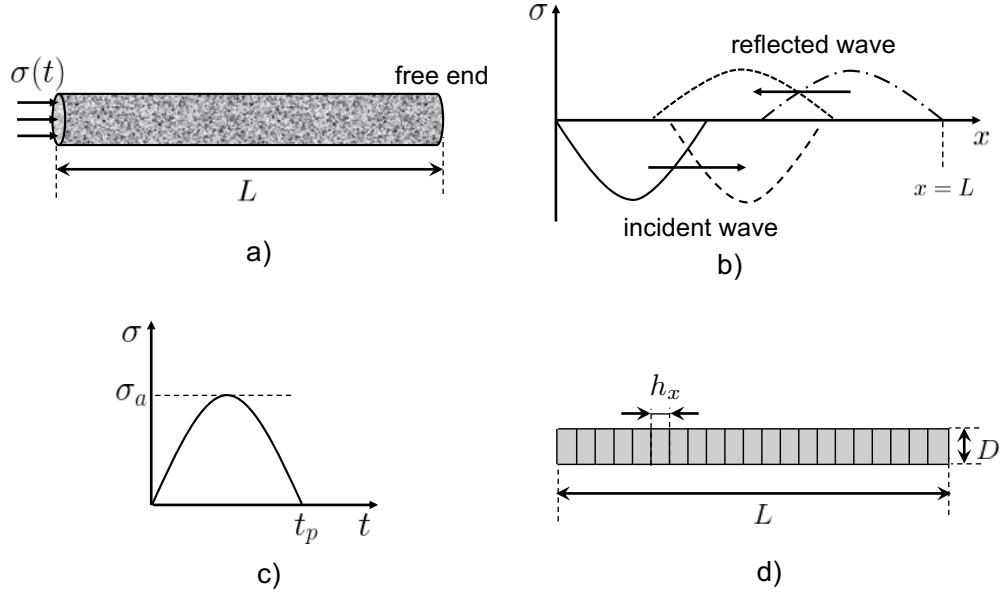


Figure 2.11: a) Schematic of the modified split Hopkinson bar test, b) stress wave traveling in the bar, c) stress pulse used in the present simulations, and d) discretization of the bar

In this study, we simulate the spalling test on a dense alumina bar of square cross-section. The bar has a size of 12 mm (length) \times 0.225 mm (depth) \times 0.225 mm (thickness). The constitutive properties are chosen to be the same as those used to produce Fig. 2.4 except that here we set

Poisson's ratio to zero in order to preserve one-dimensional wave propagation. A sinusoidal pressure pulse of half period $t_p = 1 \mu\text{s}$ is applied to the left end of the bar as an initial condition (Fig. 2.11c)). Different stress amplitudes $\sigma_a = 0.5, 0.75$ and 1.25 GPa are considered in the simulations.

The bar is discretized with one row of linear isoparametric brick elements (Fig. 2.11d)). To investigate mesh dependence, three different mesh sizes along the longitudinal direction are considered in the simulations, i.e. $h_x = h_0, 2h_0$, and $4h_0$. Nonlinear dynamic analysis is performed by using an explicit time integration scheme. A convergence study is first conducted in order to determine the required time step. In order to achieve a convergent result for all mesh sizes, the time step is found to be $5 \times 10^{-4} \mu\text{s}$, which is about 12% of the minimum time that the sound wave needs to propagate through the smallest mesh with size $h_x = h_0$. For each loading case, we consider the same three energy regularization methods as in the foregoing simulations of quasi-static fracture (i.e. approaches I-III). As mentioned, for the present model, we set κ value equal to 1 based on the simulation results of the unnotched beam.

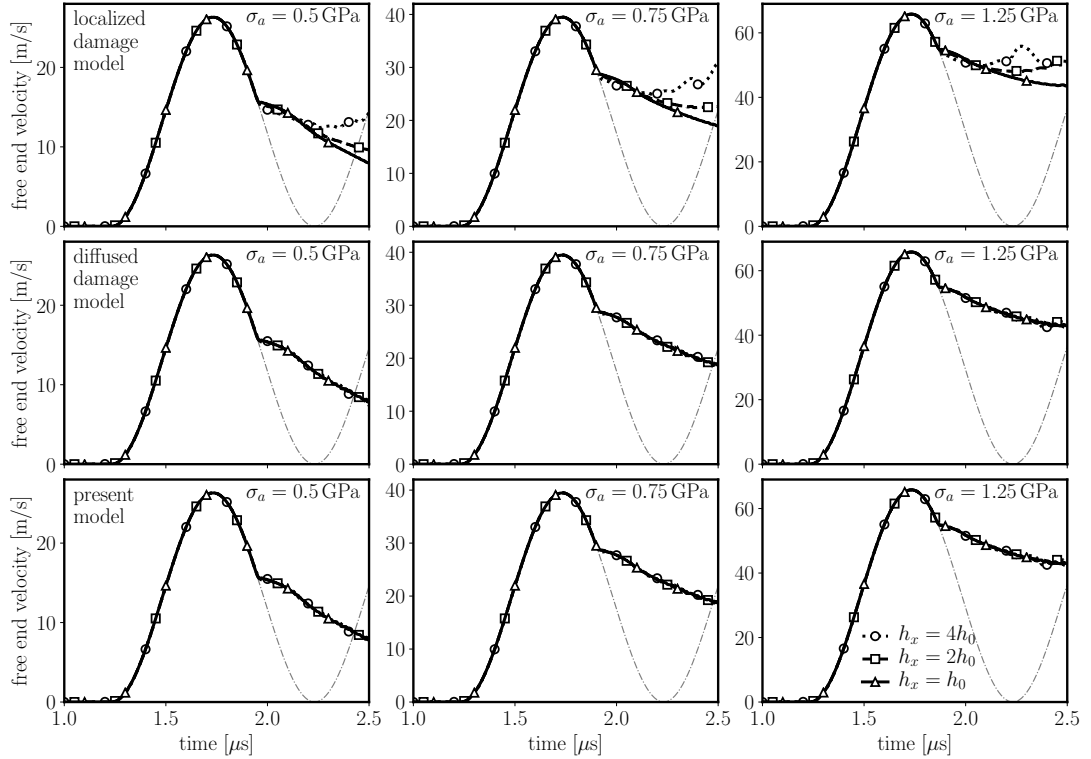


Figure 2.12: Time histories of free-end velocity predicted by the localized damage model (first row), the diffused damage model (middle row), and the present model (bottom row)

Fig. 2.12 presents the time histories of the free-end velocity simulated by the three approaches together with the elastic solution represented by the dashed line. It is seen that both the diffused damage model and the present model yield essentially the same mesh-insensitive results, whereas the simulation by the localized damage model shows a strong mesh dependence. Clearly all three methods give the same results up to the point of damage initiation (i.e. point where the result deviates from the elastic solution). Note that the peak free-end velocity corresponds to the instant when the peak of the incident stress wave has reached the free end of the bar. After tensile damage occurs, the diffused damage model and the present model predict that the free-end velocity decreases continuously over the time domain considered in the simulation, due to continuous energy dissipation in the damaged zone. By contrast, the localized damage model predicts a local minimum followed by a second ascending branch of the free-end velocity diagram for the large mesh size, which indicates the arrival of a second compressive wave at the right end. This compressive wave arises from the reflection of the previously formed tensile wave at the spalling plane in the completely damaged elements. On the other hand, for smaller mesh sizes the velocity history does not show any local minimum, since the values of the velocity continuously decrease due to energy dissipation at the spall plane. This result implies that, for the localized damage model, elements of larger size are more brittle, and therefore are more prone to damage as compared to small elements. This behavior is closely tied to its energy regularization. The central idea of the localized damage model is that, regardless of the mesh size h_x , the energy expended (per thickness) for complete damage of an element is equal to $G_f h_y$. The aforementioned mesh-dependent results indicate that the localized damage model underestimates the energy dissipation for damaging a single element.

To further analyze the energy dissipation, we plot in Fig. 2.13 the time history of the total energy dissipation due to damage: i.e. $W_d(t) = A_0 \int_L [\mathcal{W}(x, t) - \frac{1}{2} \sigma_{ij}(x, t) \epsilon_{ij}(x, t)] dx$, where A_0 = cross-sectional area of the bar, and $\mathcal{W}(x, t) = \int_0^t \sigma_{ij}(x, t') \dot{\epsilon}_{ij}(x, t') dt'$. Similarly to the aforementioned results of the time-history of the free-end velocity, the diffused damage model and the present model predict the same history of energy dissipation, which is mesh insensitive. However, the localized damage model yields a strongly mesh-dependent result. For the three stress pulses considered here, as the mesh size increases, the energy dissipation grows at a faster rate but the ultimate amount of dissipated energy becomes smaller. This result further supports the foregoing conclusion that the energy dissipation of each finite element is underestimated by the localized damage model.

The underestimation of the dissipated energy by the localized damage model indicates that the failure pattern of the bar is not featured by damage localization. In fact, the agreement between the results of the present model and the diffused damage model implies that the bar must rather

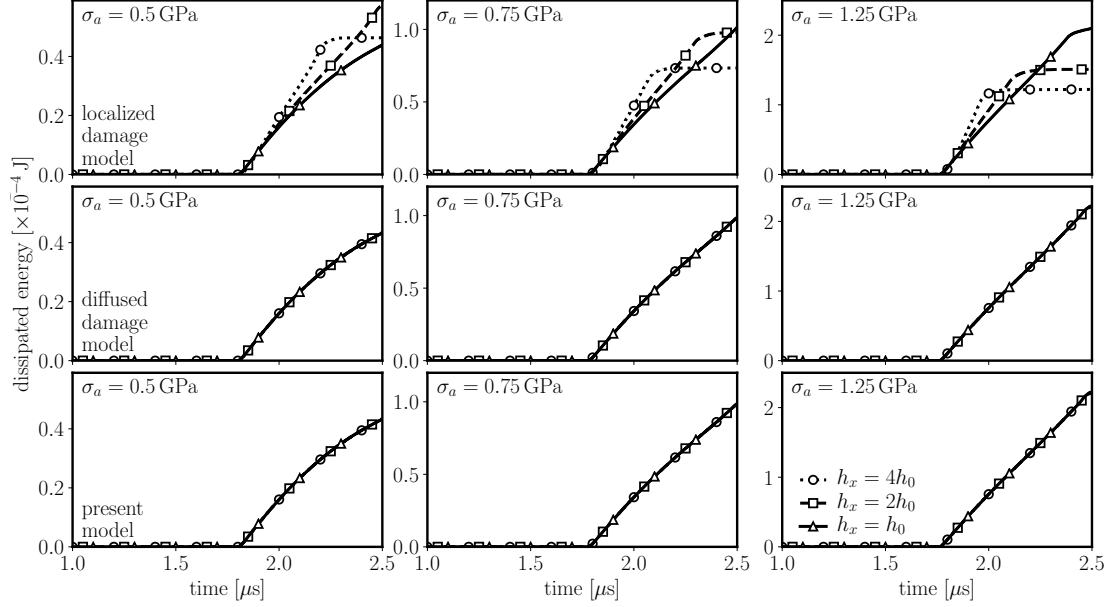


Figure 2.13: Time histories of energy dissipation simulated by the localized damage model (first row), the diffused damage model (middle row), and the present model (bottom row)

experience a diffused damage pattern. Figs. 2.14 and 2.15 show snapshots of the damage pattern at different times, as captured from the simulations using the localized damage model and the present model, respectively. It is seen that both models predict a large damage zone, the size of which is governed by the length of the reflected tensile wave. Therefore, for each stress pulse, the size of the damage zone is approximately constant regardless of the mesh size. Such damage pattern indicates that each finite element should experience diffused cracking, and therefore the energy dissipation due to damage is proportional to the mesh size h_x . However, the localized damage model enforces constant energy dissipation independent of the mesh size, which leads to underestimation of the dissipated energy as the mesh size increases. Moreover, one can note that the localized damage model predicts, at the same instant of time, more severe damage for elements of larger size, which indicates that the crack growth rate is itself mesh dependent, with damage propagating faster at larger elements (Fig. 2.14). This is again, characteristic of the more brittle behavior of larger elements imposed by the crack band model. By contrast, the present model ensures constant crack propagation velocity independent of the mesh size, as is verified by the overlapping damage profiles of all mesh sizes at all instants of time (Fig. 2.15). The present model is able to correctly capture

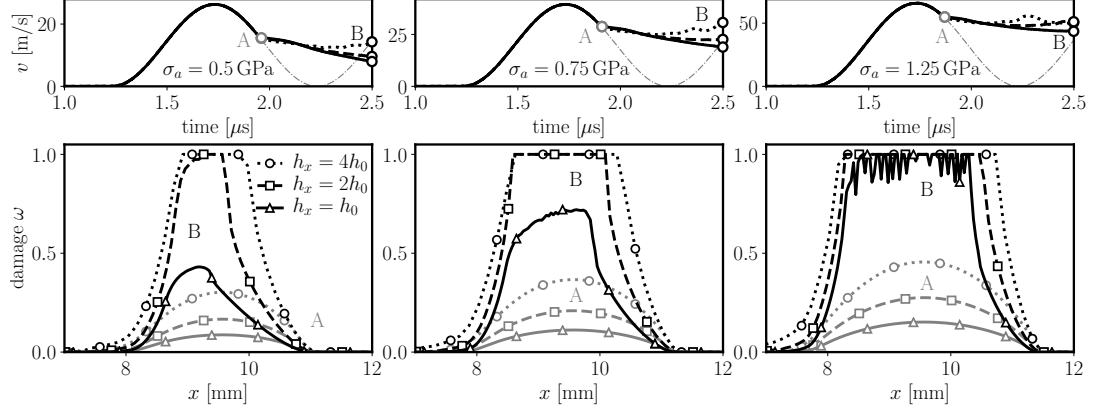


Figure 2.14: Snapshots of the damage pattern of the bar at different times simulated by the localized damage model

the energy dissipation of the element based on the information of the evolving damage state, and therefore predicts a mesh-insensitive damage pattern and overall energy dissipation. It should be mentioned that the present model may exhibit mesh sensitivity if the mesh size is so large that there is lack of sufficient resolution of the damage profile.

2.5 Conclusions

A general energy regularization method is developed for finite element (FE) simulations of quasibrittle fracture for both localized and diffused damage mechanisms [68]. The model is cast in the framework of continuum damage mechanics, with an explicit relation to fracture mechanics. By employing a localization parameter, the model adjusts the energy regularization of the material constitutive relation based on the prevalent local damage mechanism. The model is further extended to rate-dependent constitutive behavior, in which the formulation of the damage growth rate is seamlessly combined with the energy regularization scheme. The model can easily be implemented in finite element codes, and is suitable for large-scale FE simulations.

The present model is applied to analyze both static and dynamic fracture of quasibrittle structures. It is shown that the model recovers the crack band model for the case where the structure experiences a purely localized damage pattern. For structures which exhibit a transition from diffused damage to localized damage, the present model outperforms both the localized damage model and the diffused damage model in terms of suppressing the spurious mesh sensitivity. In the dynamic

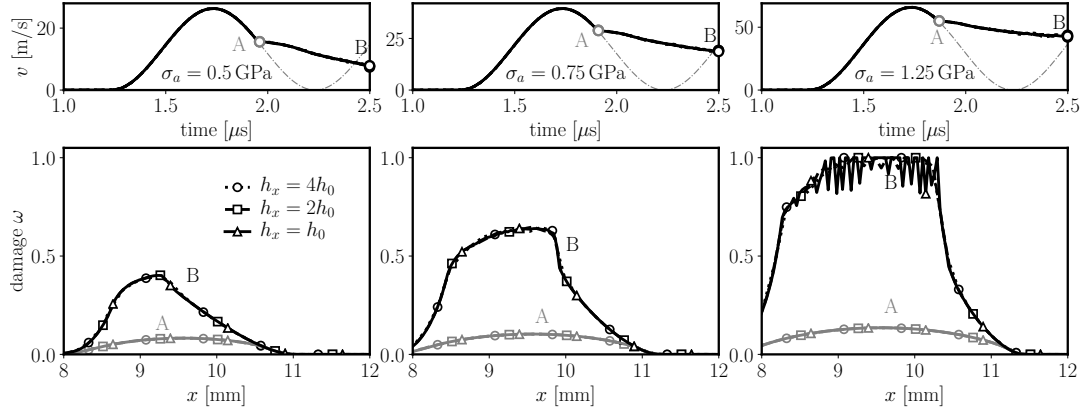


Figure 2.15: Snapshots of the damage pattern of the bar at different times simulated by the present model

spalling test, the specimen exhibits a diffused damage pattern, and the present model is shown to yield a mesh-independent simulation result. By contrast, the localized damage model grossly underestimates the energy dissipation for large mesh size. These different numerical examples clearly demonstrate the advantage of the present mechanism-based energy regularization method for FE analysis of quasibrittle structures, which may exhibit complex damage patterns under different loading scenarios.

Chapter 3

Rate and Size Effects on Strength Distribution of Quasibrittle Structures

Chapter 2 presented an energy regularization method that effectively mitigates mesh dependence in continuum finite element (FE) simulations of quasibrittle fracture under general loading scenarios. This energy regularization scheme was applied solely in deterministic analysis of quasibrittle structures. As explained in Section 1.1, stochastic FE simulations of quasibrittle fracture can lead to mesh dependent output probabilistic structural response. One potential means to mitigate the mesh dependence issue in the stochastic setting is to consider that the probability distributions of constitutive properties of finite elements depend on the mesh size. The underlying idea is to treat each finite element as a material element of finite size. This implies that the sampling distribution functions of constitutive parameters should depend on both the inherent randomness of material properties as well as the failure mechanism of the corresponding element. As shown in Chapter 2, quasibrittle structures can exhibit a complex failure pattern, including both localized and diffused damage states, which evolve during loading. Therefore, it is important to understand the size effects on quasibrittle structures under different loading configurations. For this reason, this chapter studies the combined rate and size effects on the strength statistics of quasibrittle structures through stochastic discrete element model simulations of tensile failure of ceramic specimens. An analytical probabilistic model is developed, that can capture the rate and size effects on the first and second

statistical moments of structural strength, as provided by the stochastic discrete element computations. The proposed model has important implications for mitigating mesh dependence of stochastic FE simulations of strain-softening continua.

3.1 Stochastic Discrete Model Simulations of Dynamic Failure

3.1.1 Model Description

In order to explore the underlying physical mechanisms leading to the size and rate dependent mechanical and probabilistic structural response, we perform a series of stochastic discrete element model simulations of dynamic fracture of ceramic specimens. In the computational model, the specimen is represented by a set of interconnected discrete rigid bodies. The geometry of the model is random to avoid any bias in the crack propagation direction. A set of nuclei is first randomly placed in the domain, where the mutual distance of two adjacent nuclei is controlled to be approximately equal to the grain size l_{\min} of the material. Once these nuclei are created, Voronoi tessellation is used to discretize the domain (Fig. 3.1a)). The location of the i th nuclei is denoted by \mathbf{x}_i . Each nucleus has three translational and three rotational degrees of freedom. Due to the imposition of the length scale l_{\min} , each Voronoi body can be considered to represent a material grain. The contact surface (henceforth referred to as facet) between the bodies represents the grain boundary (Fig. 3.1b)). The overall nonlinear macroscopic behavior of the material is determined by the mesoscale constitutive behavior of the facets.

In this study, the formulation of the constitutive behavior of the facet follows the lattice discrete particle model (LDPM), which was originally developed for concrete materials [4, 47–51]. Since this study focuses primarily on macroscopic tensile failure, we adopt a simplified version of the LDPM, which is briefly summarized here. The detailed description of the model can be found in [58].

The relative motion of two adjacent Voronoi bodies directly results in displacement jumps on the facet. For two adjacent bodies i and j , the displacement jump vector Δ_{ij} on their common facet can be calculated as [58]

$$\Delta_{ij} = \mathbf{A}_j \begin{pmatrix} \mathbf{u}_j \\ \boldsymbol{\theta}_j \end{pmatrix} - \mathbf{A}_i \begin{pmatrix} \mathbf{u}_i \\ \boldsymbol{\theta}_i \end{pmatrix} \quad (3.1)$$

where $\mathbf{u}_k, \boldsymbol{\theta}_k$ ($k = i, j$) = displacement and rotation vectors of the nucleus of body k and \mathbf{A}_k ($k =$

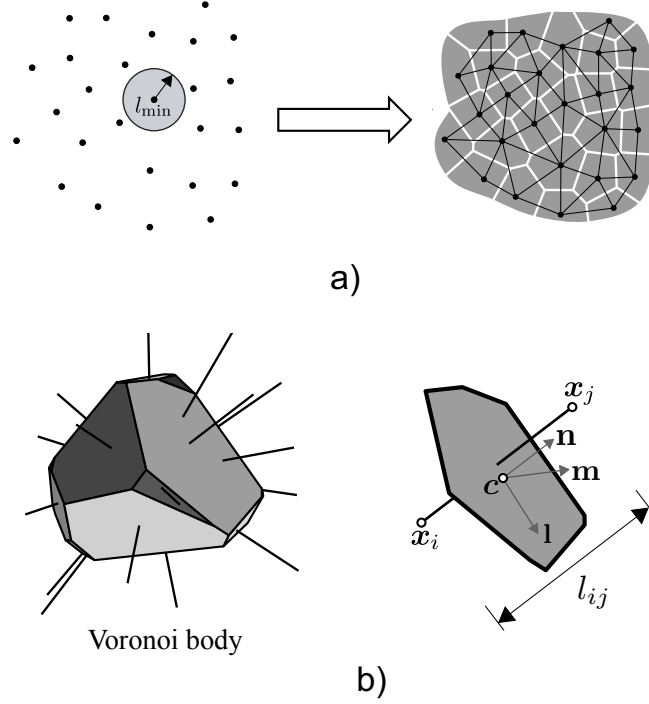


Figure 3.1: Representation of the discrete element model: a) domain discretization, and b) Voronoi body and facet

i, j) = transformation matrices, which can be written as

$$\mathbf{A}_k = \begin{bmatrix} 1 & 0 & 0 & 0 & x_3^c - x_3^k & x_2^k - x_2^c \\ 0 & 1 & 0 & x_3^k - x_3^c & 0 & x_1^k - x_1^c \\ 0 & 0 & 1 & x_2^c - x_2^k & x_1^k - x_1^c & 0 \end{bmatrix} \quad (3.2)$$

where x_1^c, x_2^c, x_3^c = coordinates of the facet centroid, and x_1^k, x_2^k, x_3^k = coordinates of the nucleus of body k .

The components of the strain vector can be calculated as $e_n = \mathbf{n} \cdot \Delta_{ij}/l_{ij}$, $e_l = \mathbf{l} \cdot \Delta_{ij}/l_{ij}$, $e_m = \mathbf{m} \cdot \Delta_{ij}/l_{ij}$, where Δ_{ij} = displacement jump vector, l_{ij} = distance between the nuclei of rigid bodies i, j , and $\mathbf{n}, \mathbf{l}, \mathbf{m}$ = unit vectors in the normal and two orthogonal tangential directions of the facet, respectively. The corresponding traction vector transmitted over the facet can then be related to

the strain vector by using damage mechanics, i.e.

$$\begin{pmatrix} t_n \\ t_l \\ t_m \end{pmatrix} = E_0(1 - \omega) \begin{pmatrix} e_n \\ \alpha e_l \\ \alpha e_m \end{pmatrix} \quad (3.3)$$

where E_0 = elastic stiffness, ω = damage parameter, α represents the ratio of tangential to normal stiffness, and t_n, t_l, t_m = components of the traction vector in the directions of \mathbf{n}, \mathbf{l} and \mathbf{m} , respectively. The damage parameter is expressed in terms of the equivalent stress and strain, i.e.

$$\omega = 1 - \frac{s_{eq}}{E_0 e_{eq}} \quad (3.4)$$

$$s_{eq} = f_{eq} \exp \left(\frac{K}{f_{eq}} \left\langle \chi - \frac{f_{eq}}{E_0} \right\rangle \right); \quad e_{eq} = \sqrt{e_n^2 + \alpha(e_m^2 + e_l^2)} \quad (3.5)$$

For tension and shear dominated loading, the equivalent strength f_{eq} can be defined as [49, 58]

$$f_{eq} = f_t \left[\frac{(\eta^2 + \mu^2) \sin \psi - \sqrt{(\eta^2 - \mu^2)^2 \sin^2 \psi + 4\alpha\eta^2 \cos^2 \psi}}{2\mu^2 \sin^2 \psi - 2\alpha \cos^2 \psi} \right] \quad (3.6)$$

where f_t = tensile strength, f_s = shear strength, $\psi = \tan^{-1} [e_n / \sqrt{\alpha(e_m^2 + e_l^2)}]$, $\eta = f_s / f_t$, and $\mu =$ constant. The history variable χ is expressed as

$$\chi = \begin{cases} e_{eq} \psi / \psi_0 + e_{max} (1 - \psi / \psi_0) & \psi_0 \leq \psi < 0 \\ e_{max} & \psi \geq 0 \end{cases} \quad (3.7)$$

where $e_{max} = \sqrt{\max(e_n^2) + \alpha \max(e_m^2 + e_l^2)}$, in which the maxima is calculated for the entire loading history, and $\psi_0 = -\arctan(\zeta \sqrt{\alpha})$. For the present numerical simulations, the facets mainly experience tensile-shear damage. Therefore, it is not necessary to cover the full scenario of compressive damage.

Finally, parameter K represents the initial slope of the nonlinear branch of the constitutive law [49], which is given by

$$K = -K_t \left[1 - \left(\frac{\psi - \pi/2}{\psi_0 - \pi/2} \right)^{n_t} \right]; \quad n_t = \frac{\ln[K_t / (K_t - K_s)]}{\ln(1 - 2\psi_0 / \pi)} \quad (3.8)$$

where K_t, K_s are the values of K for pure tensile and shear loading, respectively. K_t and K_s are

expressed as

$$K_t = \frac{2E_0}{l_t/l_{ij} - 1} \quad K_s = \frac{2\alpha E_0}{l_s/l_{ij} - 1} \quad (3.9)$$

where $l_t = E_0 G_t / f_t^2$, $l_s = E_0 G_s / f_s^2$, and G_t, G_s = mode I and II fracture energies. It should be pointed out that Eq. (3.9) involves two material length scales l_t and l_s so that the energy expended for the fracture of a unit area of facet is independent of the distance between the nuclei. Once the traction vectors on the facets are determined, the forces and moments of the nuclei can be calculated based on the principle of virtual work [58].

It is worthwhile to mention that the present constitutive model is itself rate-independent, and therefore the rate effect on macroscopic behavior of the specimen is largely due to inertia and its influence on the interaction of facet failures. Such a modeling approach has been adopted in several previous discrete simulations of dynamic fracture of ceramic materials [54, 87, 88, 138], which were able to capture the rate-dependent failure behavior reasonably well. Meanwhile, it has also been shown that the rate dependence of the constitutive behavior plays a secondary role in the overall failure behavior under high strain-rate loading [112, 113], which is of interest to the present study.

The aforementioned constitutive model contains the following parameters: 1) elastic modulus E_0 in the normal direction, 2) tangential to normal stiffness ratio α , 3) mesoscopic tensile and shear strengths f_t, f_s , 4) mesoscopic mode I and II fracture energies G_t, G_s , and 5) constants μ and ζ . It is well known that the properties of quasibrittle materials usually exhibit a considerable degree of spatial variability. For studying the failure behavior, the most relevant parameters are the strengths and fracture energies [69]. In this study, we characterize the spatial random distribution of mesoscopic strengths and fracture energies by assigning a single random field $h(\mathbf{x})$:

$$f_t(\mathbf{x}) = \bar{f}_t h(\mathbf{x}); \quad f_s(\mathbf{x}) = \bar{f}_s h(\mathbf{x}) \quad (3.10)$$

$$G_t(\mathbf{x}) = \bar{G}_t [h(\mathbf{x})]^2; \quad G_s(\mathbf{x}) = \bar{G}_s [h(\mathbf{x})]^2 \quad (3.11)$$

where the overbar denotes the mean of the corresponding random variable. Eqs. (3.10) and (3.11) imply that, on each facet, the material length scales l_t and l_s are deterministic constants. The underlying probability distribution function governing the random field $h(\mathbf{x})$ follows the Gauss-Weibull grafted distribution (Eqs. (3.16a) and (3.16b)) with a mean value equal to one. The spatial autocorrelation of the field $h(\mathbf{x})$ is characterized by a Gaussian function, i.e.

$$R(\delta x) = \exp[-(\delta x/l_a)^2] \quad (3.12)$$

where $\delta x = |\mathbf{x} - \mathbf{x}'|$ and $l_a =$ autocorrelation length. The generation of the random field $h(\mathbf{x})$ consists of three steps [59]: 1) a standard Gaussian random field $\hat{h}(\mathbf{x})$ is generated on a regular square grid with a spacing of $l_a/4$, 2) the value of $\hat{h}(\mathbf{x})$ on each facet is determined by using the optimal linear estimation method [95], and 3) the standard Gaussian field generated on the facets is converted to the Gauss-Weibull random field $h(\mathbf{x})$ by using the isoprobabilistic transformation. Fig. 3.2 presents a typical realization of the random field $h(\mathbf{x})$.

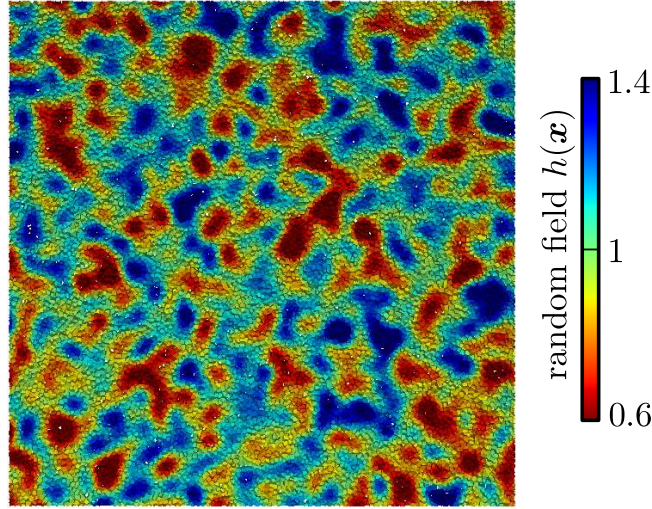


Figure 3.2: A typical realization of the random field $h(\mathbf{x})$

The aforementioned computational model is numerically implemented with the implicit Newmark method [7, 109]. The equation of motion is solved incrementally in an implicit scheme, which is unconditionally stable. The mass matrix is constructed by using the full inertia tensor of the Voronoi bodies. The moment of inertia of these polyhedral bodies are calculated by dividing them into tetrahedra [130]. Though a stable numerical solution scheme is chosen, a small time step is needed to capture the dynamic failure of the facet. For each simulation case, several trial simulations are performed to determine a desirable time step, which yields a consistent result.

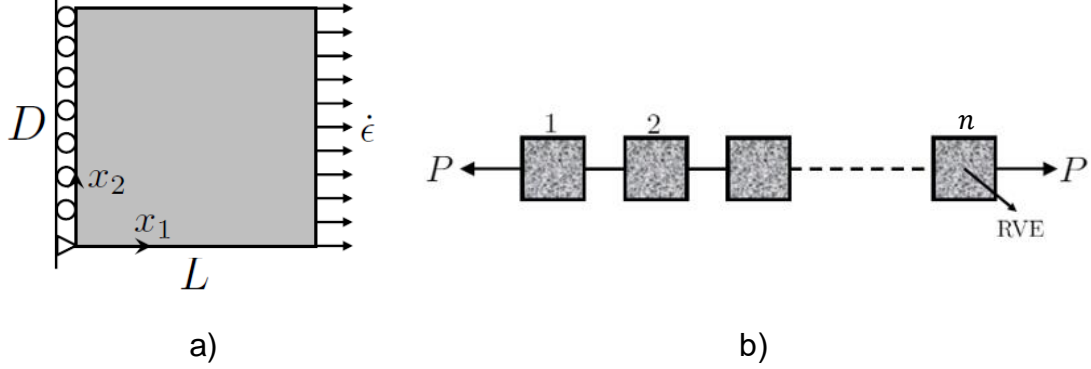


Figure 3.3: A rectangular specimen loaded by a prescribed strain rate: a) schematic of the specimen, and b) weakest link model representation

3.1.2 Simulations of Dynamic Tensile Failure of Aluminum Nitride Specimens

The aforementioned stochastic discrete element computational model is applied to simulate the dynamic tensile failure of aluminum nitride (AlN) specimens. In the simulations, we consider square specimens of different in-plane sizes $D = L = 50 \mu\text{m}$, $100 \mu\text{m}$, $200 \mu\text{m}$, $400 \mu\text{m}$, $800 \mu\text{m}$ (Fig. 3.3a)), whereas the out-of-plane thickness is set constant $b = 10 \mu\text{m}$. The average in-plane grain size l_{\min} of AlN material is taken as $6 \mu\text{m}$ [54]. Each specimen is subjected to a constant strain-rate loading, which is applied by imposing a non-uniform velocity field described as $v_{x_1} = x_1 \dot{\epsilon}$ (x_1 denotes the horizontal position of each nucleus). This velocity gradient is applied as an initial condition ($t = 0$), whereas at subsequent times ($t > 0$) only the velocities of the sections at $x_1 = 0$ and $x_1 = L$ are controlled (equal to 0 and $\dot{\epsilon}L$ respectively). In order to investigate the rate-dependent behavior, we consider a wide range of applied strain rates, i.e. $\dot{\epsilon} = 1, 1000, 2500, 5000, 7500, 10^4, 3 \times 10^4, 5 \times 10^4, 10^5, 2 \times 10^5/\text{s}$.

We choose the following mesoscale material parameters for AlN: $E_0 = 530 \text{ GPa}$, $\alpha = 0.17$, $\bar{f}_t = 150 \text{ MPa}$, $\bar{f}_s = 3\bar{f}_t$, $\bar{G}_t = 2 \text{ Jm}^{-2}$, $\bar{G}_s = 16\bar{G}_t$, $\mu = 0.2$, and $\zeta = 0.95$. The elastic parameters (E_0 and α) are determined to match the macroscopic elastic response of AlN reported in [54]. The inelastic mesoscale material parameters are chosen so that the model predicts the quasi-static tensile strength of a $50 \mu\text{m}$ square AlN specimen being about 120 MPa , which is similar to the published results [54]. It is admitted that mixed-mode loading scenarios will be needed to better calibrate

the coupling between tensile and shear damage. However, such a detailed calibration procedure is not necessary for the present purpose. For the random field $h(\mathbf{x})$, we consider that it has an autocorrelation length l_a of $24\text{ }\mu\text{m}$, and the underlying Gauss-Weibull distribution function has a mean value of one, a coefficient of variation of 20%, a Weibull modulus of 30 and a grafting probability of 5×10^{-4} .

For each specimen size and strain rate, about 70 realizations of different random fields $h(\mathbf{x})$ and mesostructures are used to determine the mean and variance of the peak load capacity of the specimen. As mentioned earlier, the peak load capacity of the specimen is expressed in terms of the nominal strength, which in this case is equal to the maximum value of the nominal stress σ_a along the x_1 -direction (Fig. 3.3a)). For the present discrete system, we first calculate the fabric stress tensor of a single Voronoi body k as in [5, 77, 122]:

$$\bar{\boldsymbol{\sigma}}^k = \frac{1}{V_k} \sum_{p=1}^{n_k} \mathbf{t}^p \otimes (\mathbf{x}^{cp} - \mathbf{x}^k) A_p \quad (3.13)$$

where V_k = volume of the k th body, n_k = number of facets of the body, \mathbf{t}^p = traction vector on the p th facet expressed in the global coordinate system, \mathbf{x}^{cp} = position vector of the centroid of the p th facet, \mathbf{x}^k = position vector of the nucleus of the body, and A_p = surface area of the p th facet. The nominal stress σ_a can then be calculated as a volume average of the fabric stress components in the x_1 -direction, i.e.:

$$\sigma_a = \frac{1}{V} \sum_{k=1}^N V_k \bar{\sigma}_{11}^k \quad (3.14)$$

where V = volume of the specimen, and N = number of Voronoi bodies in the specimen.

Based on the simulations, we obtain a set of random responses of the relationship between the nominal stress σ_a and the average strain ϵ_a , where $\epsilon_a = u/D$ and u = displacement measured at the free edge of the specimen. Fig. 3.4 presents the simulated average σ_a - ϵ_a curves for all specimen sizes and strain rates. It can be seen that, for a given specimen size, the average nominal strength $\bar{\sigma}_N$, which is the maximum value of the average nominal stress, increases with the applied strain rate. This rate enhancement is primarily due to the inertia effect. Meanwhile, we also observe that, as the strain rate increases, the post-peak softening behavior becomes less pronounced, which indicates that the specimen exhibits a more ductile behavior. This rate dependence can directly be observed from the simulated damage pattern at the peak load. As a demonstration, Fig. 3.5 shows the damage patterns of specimens of $D = 400\text{ }\mu\text{m}$ at the peak load for different applied strain rates. It is seen that, for a given specimen size, the damage is fairly localized at low strain rates while the specimen

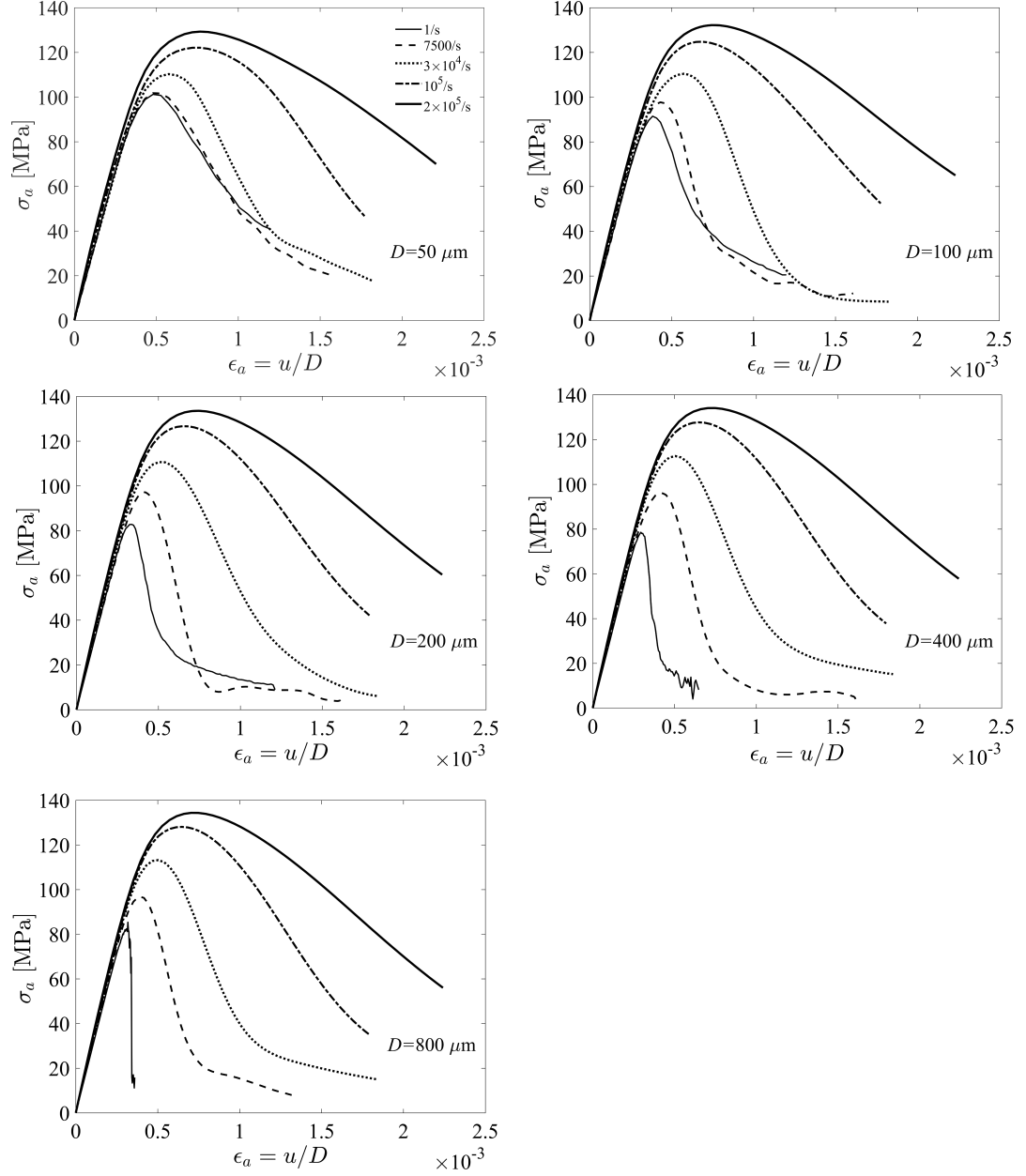


Figure 3.4: Simulated average nominal stress-strain curves for different specimen sizes and strain rates

exhibits a diffused damage pattern as the strain rate increases.

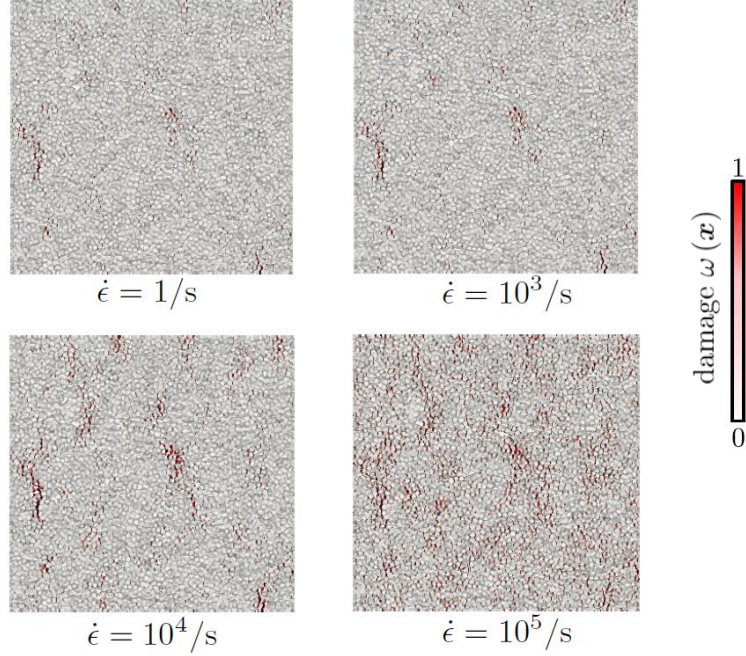


Figure 3.5: Simulated damage patterns of specimen of $D = 400\mu\text{m}$ at the peak load

It should be pointed out that the aforementioned brittle-to-ductile transition is based on the current simulation setup with the prescribed initial velocity field. Recent computational studies of ceramics and concrete specimens with the same setup showed similar rate-dependent failure patterns [54, 64]. Several experiments on the rate-dependent behavior of concrete also showed that the tensile stress-strain curve exhibits a more gentle post-peak softening behavior at high strain rates [72, 133]. However, there is experimental evidence showing that the compressive stress-strain response of brittle composites and ceramics could become more brittle at higher strain rates [35, 84, 96]. The setups of these experiments are different from the present simulations. We may expect that the rate dependence of failure behavior of quasibrittle materials could depend strongly on the specimen geometry and test configuration. This is consistent with the well accepted fact that, for quasibrittle structures, brittleness is influenced not only by the material properties, but also by the structure geometry and loading configuration. [8, 15, 19].

We can also compare the simulated post-peak responses of specimens of different sizes for a given strain rate. It is seen that, at low strain rates, the slope of the post-peak softening curve becomes much steeper as the specimen size increases. This implies that the specimen experiences a more brittle failure as the specimen size increases. Such a size dependent failure behavior at low strain rates has been well documented for many quasibrittle materials, such as concrete, rock, composites, ceramics, etc. [8, 19]. As the strain rate increases, the size dependence of the post-peak behavior starts to diminish. This is consistent with the present simulation results, which show that, at high strain rates, all the specimens considered in this study exhibit a diffused cracking pattern.

3.2 Rate-Dependent Finite Weakest Link Model

3.2.1 Model Formulation

The simulation results presented in Section 3.1.2 clearly indicate the rate dependence of the failure behavior of quasibrittle structures. Accurate probabilistic modeling of failure requires the assumptions of the corresponding mathematical models to be consistent with the actual failure mechanism of a structure, therefore the rate effect, through its influence on the failure mechanism, can have profound implications in the development of such models. In this section, we develop an analytical probabilistic model that can describe the combined rate and size effects on the strength distribution of quasibrittle structures. The statistics of static strength of quasibrittle structures of positive geometry have been described by the finite weakest link model [18, 90], which considers the structure to be statistically represented by a chain of representative volume elements (RVEs), and assumes that structural failure will occur as soon as a RVE fails. This assumption is realistic for quasibrittle structures of positive geometry, since these structures fail right at the initiation of a macroscopic crack. At the same time, the finite weakest link model takes into account the influence of the finite size fracture process zone (FPZ) on the failure behavior of quasibrittle structures, and is thus more general than Weibull's statistical theory [134], which applies to brittle failure only.

Since in this study we focus on quasibrittle structures, we essentially build upon the finite weakest link model, which will provide the limiting strength distribution for the case of very low strain rates (quasi-static), and extend this model so as to account for the change in the failure mechanism with an increasing strain rate. Considering a set of geometrically similar rectangular quasibrittle specimens, which are loaded under displacement control with a prescribed strain rate (Fig. 3.3a)), we define the nominal tensile strength, σ_N , as the maximum average stress that the specimen can sustain. In the weakest link representation of the structure (Fig. 3.3b)), we consider that the RVE size is

taken to be larger than the autocorrelation length of the underlying random strength field, thus the RVE strengths can be modeled as statistically independent random variables with cumulative distribution function (cdf) P_1 . In this case, the structural failure probability P_f (under quasi-static loading conditions) can be expressed as follows:

$$P_f(\sigma_N) = 1 - [1 - P_1(\sigma_N)]^n \quad (3.15)$$

where n is the number of RVEs in the structure, which, for the case of two-dimensional scaling, is equal to $n = A/l_{0s}^2$, $A = DL$ = area of the specimen, and l_{0s} = RVE size under quasi-static loading.

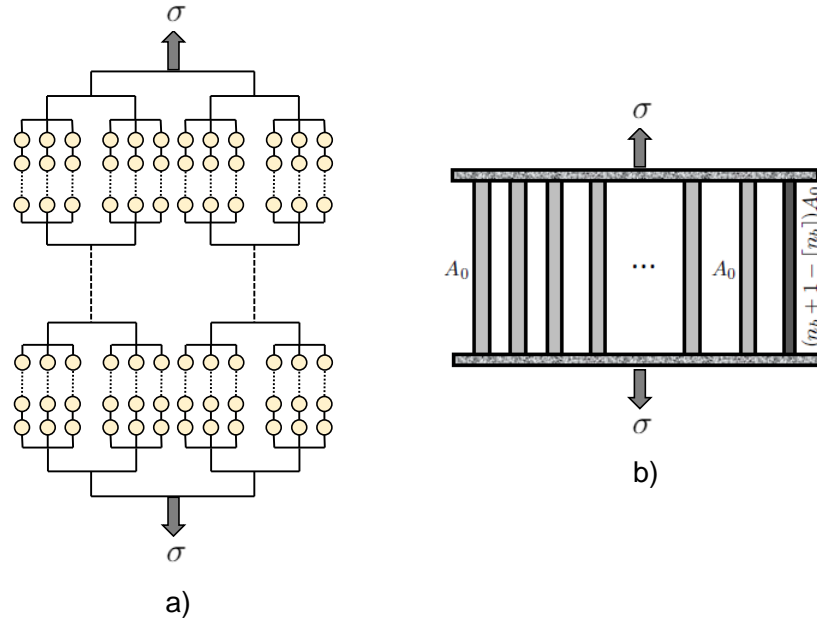


Figure 3.6: Modeling of strength distribution of a RVE: a) hierarchical model of static RVE, and b) fiber-bundle model of RVE under high strain-rate loading

In recent studies on statistics of static strength [14,15,18,90], it was shown that the RVE can be statistically modeled by a hierarchical model, which consists of a combination of bundles and chains (Fig. 3.6a)). This hierarchical model represents damage localization and load redistribution mechanisms at different material scales. The basic element in the model represents a nanoscale structure, either an atomic lattice or a disordered system of nano-particles. The failure statistics of the nanoscale structure was derived based on the transition rate theory and atomistic fracture mechanics [14,15,90]. Based on the hierarchical model, it was shown that the probability distribution

of the static strength of the RVE can be approximated by a Gaussian distribution onto which a Weibull tail (or, equivalently, a power-law tail) is grafted at a fairly low probability. Mathematically, the cdf of the RVE strength can be written as

$$P_1(\sigma_N) = \begin{cases} 1 - \exp(-\langle \sigma_N/s_0 \rangle^{m_0}) \approx \langle \sigma_N/s_0 \rangle^{m_0} & (\sigma_N \leq \sigma_{\text{gr}}^0) \\ P_{\text{gr}}^0 + \frac{r_{f0}}{\delta_{G0}\sqrt{2\pi}} \int_{\sigma_{\text{gr}}^0}^{\sigma_N} e^{-(x-\mu_{G0})^2/2\delta_{G0}^2} dx & (\sigma_N > \sigma_{\text{gr}}^0) \end{cases} \quad (3.16a)$$

$$(3.16b)$$

where m_0 and s_0 are the Weibull modulus and the scale parameter of the Weibull tail, respectively, and μ_{G0} and δ_{G0} are the mean and standard deviation of the Gaussian core if considered extended to $-\infty$; r_{f0} is a scaling parameter required to normalize the grafted cdf such that $P_1(\infty) = 1$, σ_{gr}^0 = grafting stress, and $P_{\text{gr}}^0 = (\sigma_{\text{gr}}^0/s_0)^{m_0}$ = grafting probability. Note that here the subscript and superscript “0” of all the parameters indicate the quasi-static case. The continuity of the probability density function (pdf) at the grafting point requires that $[dP_1/d\sigma_N]_{\sigma_{\text{gr}}^0+} = [dP_1/d\sigma_N]_{\sigma_{\text{gr}}^0-}$. Therefore, there are in total four independent parameters to define the grafted distribution of the RVE strength.

To incorporate the strain rate effect into the probabilistic model of structural failure, we start by modifying the weakest link model (Eq. (3.15)) in order to account for the rate dependence of the RVE size, denoted as $l_0(\dot{\epsilon})$. Several recent studies [54, 64] have investigated the dynamic tensile fracture behavior of ceramic and concrete materials by considering specimens similar to that depicted in Fig. 3.3a). These simulation results consistently showed that, with an increasing strain rate, the damage pattern becomes more diffusive, in agreement with the results of the present stochastic discrete element model computations described in Section 3.1.2. Therefore, we expect that the RVE size $l_0(\dot{\epsilon})$ will be an increasing function of the strain rate. Besides, the strain rate can also affect the statistical parameters of the distribution function $P_1 = P_1(\sigma_N, \dot{\epsilon})$. Based on the foregoing discussion, we can express the structural failure probability $P_f(\sigma_N, \dot{\epsilon})$ by a rate-dependent weakest-link model:

$$P_f(\sigma_N, \dot{\epsilon}) = 1 - [1 - P_1(\sigma_N, \dot{\epsilon})] [1 - P_1(\sigma_N, \dot{\epsilon})]^{(n(\dot{\epsilon})-1)} \quad (3.17)$$

where $P_1(\sigma_N, \dot{\epsilon})$ = strength distribution of either one RVE or the entire specimen, whichever has a smaller size, $n(\dot{\epsilon}) = A/[l_0(\dot{\epsilon})]^2$, $\langle x \rangle = \max(x, 0)$ = Macaulay bracket, and $l_0(\dot{\epsilon})$ = RVE size under dynamic loading conditions. Since the RVE size increases with the rate, for a given specimen size, an increase in the applied strain rate could possibly make the RVE larger than the specimen size, i.e. $n(\dot{\epsilon}) < 1$. In this case, Eq. (3.17) reduces to $P_f(\sigma_N, \dot{\epsilon}) = P_1(\sigma_N, \dot{\epsilon})$. In other words, $P_1(\sigma_N, \dot{\epsilon})$ becomes the strength distribution of the entire specimen. This implies that the weakest-link representation of structural failure vanishes since there is no damage localization in the specimen.

In order to determine the rate dependence of the distribution function $P_1(\sigma_N, \dot{\epsilon})$, we propose a fiber-bundle model for the RVE under dynamic loading, which consists of $\lceil n_b \rceil$ fibers, where $\lceil n_b \rceil =$ the least integer that is greater than or equal to n_b , and n_b represents the equivalent number of static RVEs in the dynamic RVE or in the entire structure, whichever is smaller:

$$n_b(\dot{\epsilon}) = \min[n(\dot{\epsilon}), 1] \left[\frac{l_0(\dot{\epsilon})}{l_{0s}} \right]^2 \quad (3.18)$$

where, it should be noted that, in the present context, we refer to an RVE of size equal to l_{0s} as the static RVE. The fiber-bundle statistical model represents a structure as a series of elements, called fibers, which are loaded in parallel (Fig. 3.6b)). In contrast to the weakest link model, the fiber-bundle model represents structural failure under distributed cracking, since, as soon as a fiber fails, its load is redistributed among other surviving fibers, preventing global failure. Thus, it is considered to be able to realistically represent the damage redistribution mechanism of the RVE under high strain rates (or of the entire specimen if $n(\dot{\epsilon}) < 1$), given the diffused damage pattern observed (Section 3.1.2).

Each fiber in the bundle model of the dynamic RVE represents a static RVE. For quasibrittle materials, the mechanical behavior of the static RVE will exhibit some degree of strain-softening. On the other hand, we also note that the static RVE should behave in a quasi-plastic manner since it contains only a few material heterogeneities [18]. This quasi-plastic failure behavior is also manifested by the dominant Gaussian distribution of RVE strength as indicated by Eq. (3.16b) [15, 18, 90]. Therefore, the stress-strain curve of the static RVE must have a gentle softening behavior even under quasi-static loading. As the applied strain rate increases, the static RVE would experience more diffusive micro-cracking, which alleviates the degree of strain softening [54, 64, 72, 133]. For this reason, we consider that the elements in the fiber-bundle model exhibit a plastic stress-strain behavior. Besides, the individual fiber strengths can be treated as statistically independent random variables, since the autocorrelation length of the random strength field is considered to be smaller than the size of the static RVE. The plastic bundle model of the RVE under dynamic loading indicates that the bundle strength is a weighted sum of the strengths of the individual fibers, which leads to the following relationship:

$$\sigma_N^b = \frac{1}{n_b} \left[\sum_{i=1}^{\lceil n_b \rceil - 1} \sigma_i + (n_b + 1 - \lceil n_b \rceil) \sigma_{\lceil n_b \rceil} \right] \quad (3.19)$$

where σ_i ($i = 1, \dots, \lceil n_b \rceil$) are the random strengths of the individual fibers. Since n_b may not be

an integer, in writing Eq. (3.19) we have considered that the bundle contains $\lceil n_b \rceil$ fibers, where $\lceil n_b \rceil - 1$ fibers have the same cross-sectional area A_0 , and the remaining fiber has a cross-sectional area of $(n_b + 1 - \lceil n_b \rceil)A_0$. The strength distribution of each fiber representing a static RVE is predominantly Gaussian with a very short power-law tail (Eqs. (3.16a) and (3.16b)). Previous studies have shown that, for such a strength distribution of fibers, the strength distribution of the bundle will also contain a power-law tail, and meanwhile the core of the strength distribution of the bundle is Gaussian [18]. Therefore, it is clear that the previously proposed grafted distribution function (Eqs. (3.16a) and (3.16b)) provides the correct functional form for the strength distribution function $P_1(\sigma_N, \dot{\epsilon})$, though the values of the statistical parameters must now depend on the applied strain rate.

As mentioned earlier, the grafted distribution function of the RVE strength can be determined by any four statistical parameters in Eqs. (3.16a) and (3.16b). In this study, we incorporate the strain rate dependence into the strength distribution function $P_1(\sigma_N, \dot{\epsilon})$ through the following four parameters:

- The Weibull modulus m measures the exponent of the power-law tail of the bundle. By using the series expansion method, it was shown that the power-law exponent of the bundle is equal to the sum of the power-law exponents of the tail distributions of the individual fibers [18]. In fact, this property also holds for brittle and softening bundles, where the randomness of the stress-strain curve of the fibers is described by an affine transformation [15, 90, 126]. Meanwhile, the strain rate may also affect the Weibull modulus of the static RVE itself, which is described by an empirical function $f(\dot{\epsilon})$ to be determined later. Following these considerations, we can express the Weibull modulus of the distribution function $P_1(\sigma_N, \dot{\epsilon})$ as

$$m(\dot{\epsilon}) = m_0 f(\dot{\epsilon}) \lceil n_b(\dot{\epsilon}) \rceil \quad (3.20)$$

- The grafting probability P_{gr} determines the extent of the power-law tail. Previous studies have shown that, as the number of fibers increases, the power-law tail of the strength distribution of the bundle shortens at the rate of $(P_{gr,f}/\lceil n_b \rceil)^{\lceil n_b \rceil}$ ($P_{gr,f}$ is the grafting probability of the strength distribution of an individual fiber) [18]. By further considering the potential influence of the strain rate on the grafting probability of the static RVE, the rate-dependent grafting probability is written as

$$P_{gr}(\dot{\epsilon}) \approx [P_{gr}^0 g(\dot{\epsilon}) / \lceil n_b(\dot{\epsilon}) \rceil]^{\lceil n_b(\dot{\epsilon}) \rceil} \quad (3.21)$$

where the term $P_{gr}^0 g(\dot{\epsilon})$ describes the rate-dependent grafting probability of the static RVE. Based on Eq. (3.21), it is clear that the Weibull tail of the RVE strength is shortened drastically as n_b increases. This means that, when the strain rate is sufficiently high, Eq. (3.20) becomes practically unimportant.

- Parameter μ_G is approximately equal to the mean strength of the plastic bundle. The power-law tail of the strength distribution of each fiber is too short to influence the mean behavior. Based on the statistics of the weighted sum of independent Gaussian variables (Eq. (3.19)), it is clear that μ_G is equal to the mean strength of each fiber, which leads to the following expression

$$\mu_G(\dot{\epsilon}) = \mu_{G0} p(\dot{\epsilon}) \quad (3.22)$$

where $p(\dot{\epsilon})$ is the rate enhancement function of the mean strength of the static RVE.

- Parameter δ_G measures the standard deviation of the bundle strength since the power-law tail of the distribution function has a minimal influence on the second moment of statistics. The statistics of the weighted sum of independent Gaussian variables gives

$$\delta_G(\dot{\epsilon}) = \frac{\delta_{G0} q(\dot{\epsilon})}{n_b} \left[\lceil n_b \rceil - 1 + (n_b + 1 - \lceil n_b \rceil)^2 \right]^{1/2} \quad (3.23)$$

where function $q(\dot{\epsilon})$ describes the influence of the strain rate on the standard deviation of the strength of the static RVE.

By substituting Eqs. (3.20)-(3.23) into the grafted distribution function (Eqs. (3.16a) and (3.16b)), we obtain the rate-dependent strength distribution function $P_1(\sigma_N, \dot{\epsilon})$. Based on the rate-dependent weakest-link model (Eq. (3.17)), we can then calculate the mean dynamic strength of the specimen as:

$$\bar{\sigma}_N(\dot{\epsilon}) = \int_0^1 \sigma_N dP_f(\sigma_N, \dot{\epsilon}) = \int_0^\infty [1 - P_1(\sigma_N, \dot{\epsilon})] [1 - P_1(\sigma_N, \dot{\epsilon})]^{(n(\dot{\epsilon})-1)} d\sigma_N \quad (3.24)$$

Meanwhile, the model also yields the rate-dependent second moment of strength statistics. For instance, the standard deviation of the dynamic strength can be calculated as:

$$\delta_{\sigma_N}(\dot{\epsilon}) = \sqrt{\int_0^1 \sigma_N^2 dP_f(\sigma_N, \dot{\epsilon}) - [\bar{\sigma}_N(\dot{\epsilon})]^2} \quad (3.25)$$

By considering specimens of different sizes, we can determine the effect of the specimen size on the statistics of dynamic strength. Together with the aforementioned rate dependence, Eqs. (3.24) and

(3.25) describe the combined size and rate effects on the first and second moments of the statistics of nominal tensile strength of the specimen.

3.2.2 Numerical Verification

We now use the rate-dependent finite weakest-link model (Eqs. (3.24) and (3.25)) to compare with the rate and size effects on the mean and standard deviation of structural strength as simulated by the stochastic discrete element model. Fig. 3.7 presents the size effect curves of the mean nominal strength at different applied strain rates. The most salient feature is that the mean size effect diminishes as the strain rate increases. At high strain rates, the entire specimen is occupied by diffused cracking as the peak load is reached (Fig. 3.5). In such a case, there does not exist any characteristic length scale governing the nominal strength. Since the failure is ductile (or quasi-plastic), the size effect on the nominal strength must be absent [8,15]. As the strain rate decreases, the damage pattern transitions from diffused cracking to a localized cracking zone. The size of the localized damage zone represents a characteristic length scale, which leads to a non-power law form of the mean size effect curve. As seen from the predictions of the rate-dependent finite weakest link model in Fig. 3.7, the influence of the strain rate on the mean size effect behavior can correctly be captured.

Based on this fitting, we determine the rate effect on the RVE size and on the statistical parameters of the strength distribution of the static RVE. From Fig. 3.8 it is clear that the RVE size l_0 increases with the strain rate. More specifically, the RVE size is almost constant for relatively low strain rates, and increases mildly over a range of intermediate strain rates $3 \times 10^4 - 5 \times 10^4$ /s. When the strain rate exceeds 5×10^4 /s, the RVE size increases significantly with the strain rate. In fact, for the high strain-rate regime studied here, the analysis indicates that all the specimens are smaller than the dynamic RVE. Therefore, the actual RVE size is not known. At high strain rates, the RVE can become a purely mathematical concept if the specimen does not exhibit damage localization. In this case, we may set $l_0(\dot{\epsilon})$ to be a very large number. However, introducing the concept of the RVE for the present theoretical framework is essential because it captures the rate dependence of the failure statistics, which transitions from a weakest-link model signifying the damage localization mechanism to a fiber-bundle model representing the more diffused damage mechanism with increasing strain rate.

The concept of the RVE is central to the present weakest-link model. In a recent study [93], it has been shown that the RVE size can be best determined from the optimum fitting of the mean size curve of nominal structural strength, and a relationship between the RVE size and basic material

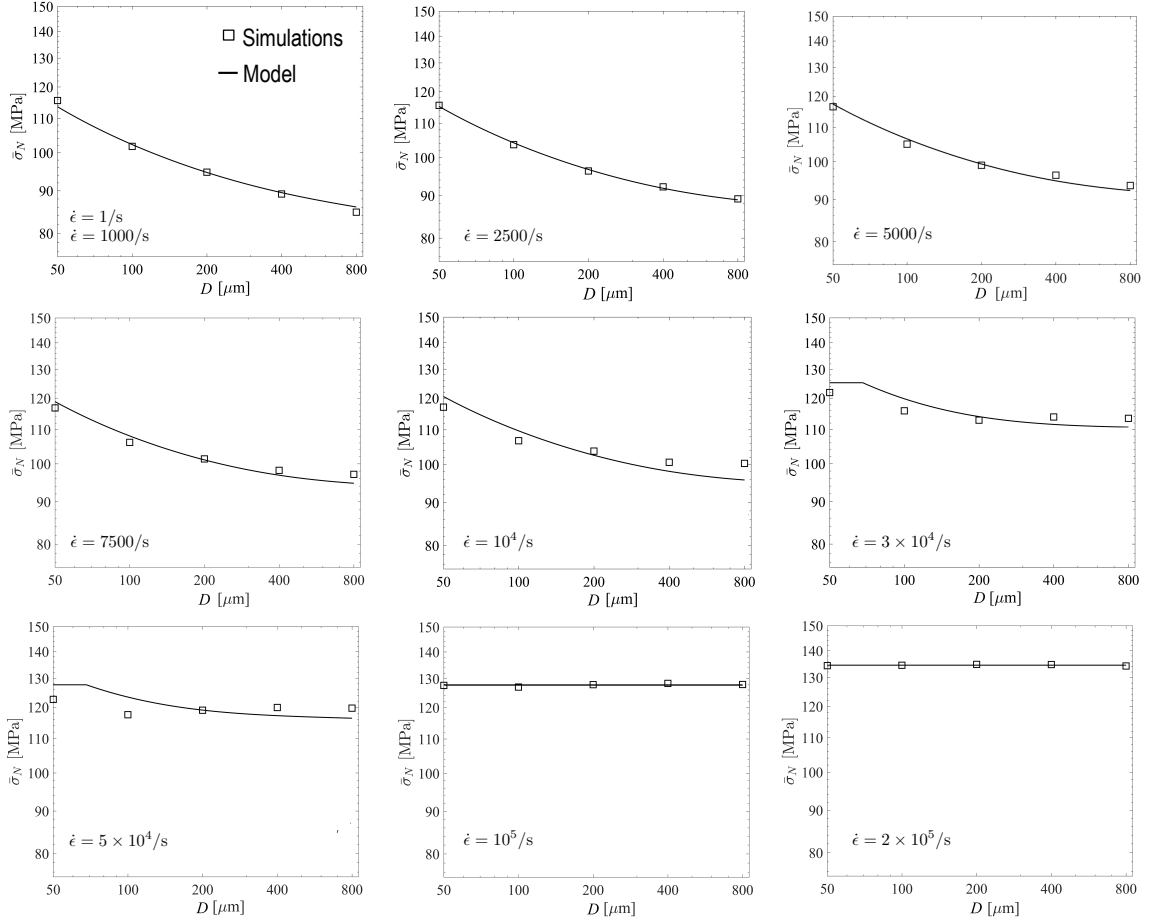


Figure 3.7: Simulated mean size effect curves of nominal strength at different strain rates and the optimum fits by the rate-dependent finite weakest-link model

length scales (Irwin's characteristic length and crack band width), was established for the case of quasi-static loading. Based on the results of this recent study, we expect that the RVE size will increase with the average grain size. Meanwhile, the RVE size will also increase with an increase in the mesoscale fracture energies. This implies that the RVE size is dependent on the loading configuration. For example, if the applied loading induces more shear-dominant fractures along the grain boundaries, based on the material properties used in the present simulation the specimen will exhibit a more ductile failure behavior and therefore the RVE size will increase.

Fig. 3.9 presents the influence of the applied strain rate on the strength statistics of a RVE with size equal to the corresponding static value l_{0s} (herein referred as the static RVE). We observe that Weibull modulus increases with the applied strain rate (i.e. $f(\dot{\epsilon}) > 1$ in Eq. (3.20)) and the grafting

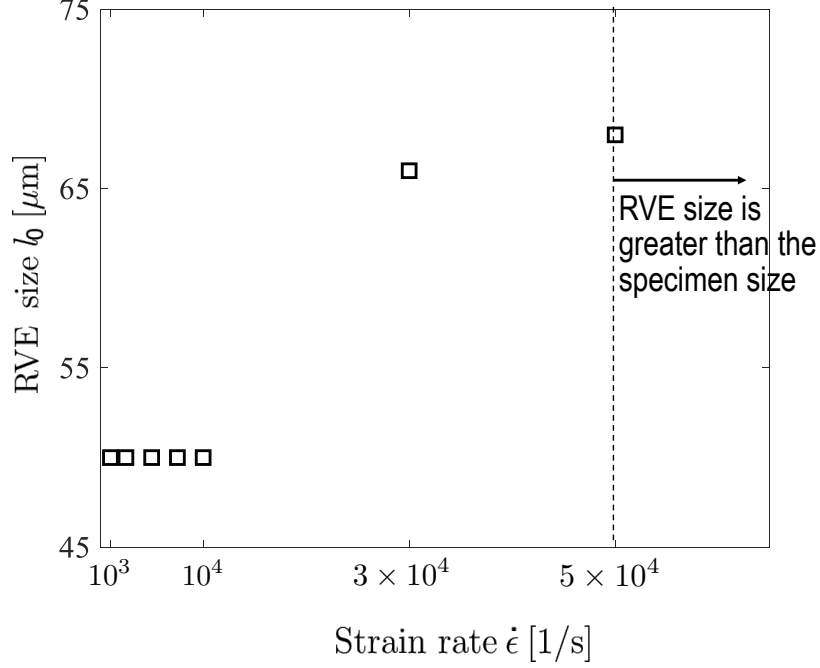
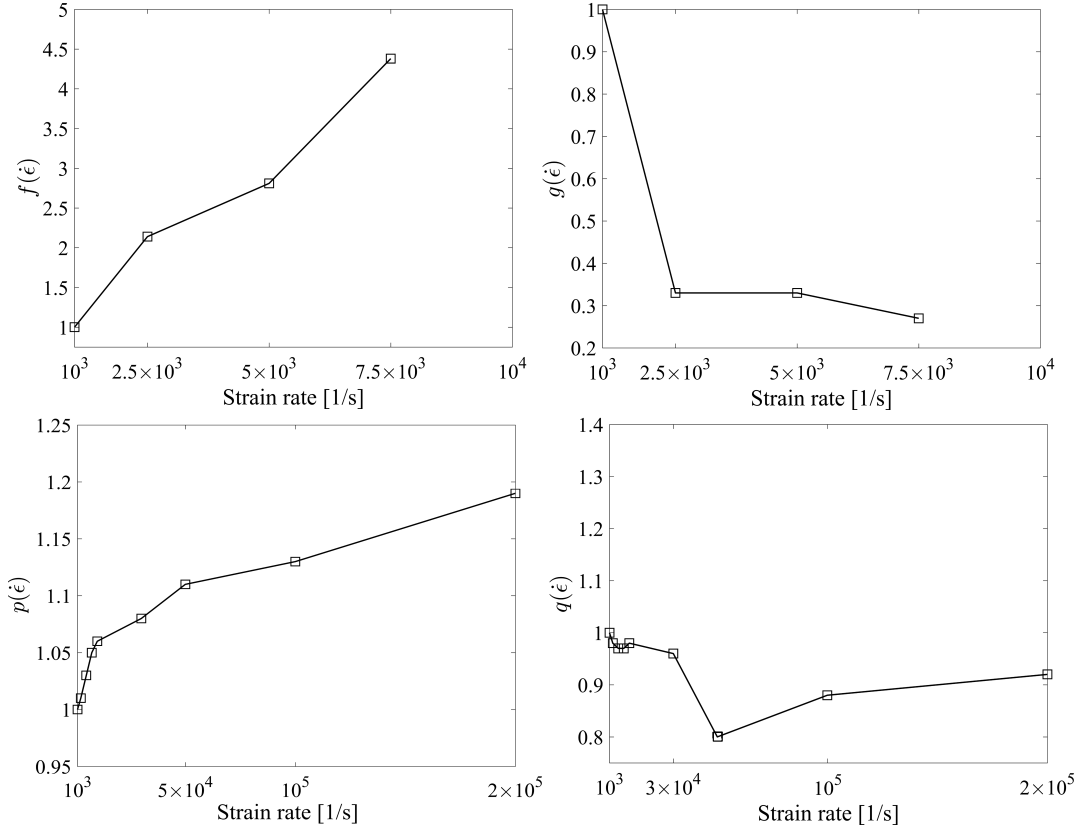


Figure 3.8: Effect of the strain rate on the RVE size

probability decreases with the strain rate (i.e. $g(\dot{\epsilon}) < 1$ in Eq. (3.21)). It is noted that, when the strain rate is higher than 7500/s, the power-law tail of the strength distribution of the static RVE is too short to be determined for the range of specimen sizes considered here. The observed rate dependence of the strength statistics of the static RVE can be attributed to the fact that, as the strain rate increases, the static RVE experiences more dense micro-cracking. In the context of the present stochastic discrete element model, microcracking is represented by the failure of grain boundaries (facets). The increase in the Weibull modulus can be qualitatively explained by the fishnet statistics model (Section 1.3.3), which was recently developed to analyze a fishnet structure for predicting the probability distribution of static strength of nacreous imbricated lamellar materials. Though the specimens dealt in the present study are very different from the fishnet structure, due to the similar failure mechanism which is described by diffuse microcracking, the same mathematical framework can be applied to both cases.

Following the fishnet model [99], the strength distribution of a static RVE can be calculated as

$$F_s(\sigma_N) = 1 - [P_{s,0}(\sigma_N) + P_{s,1}(\sigma_N) + \cdots + P_{s,N}(\sigma_N)] \quad (3.26)$$

Figure 3.9: Rate dependence of the statistical parameters of $P_1(\sigma_N)$

where $P_{s,r}$ = survival probability when r number of facets have experienced damage at stress level σ_N applied to the static RVE, and N = total number of facets. For obtaining an approximation to Eq. (3.26), we just need to retain several dominant terms ($r = 0, \dots, k$), which contribute to the overall failure probability. The aforementioned rate effect on microcracking density indicates that the number of damaged facets k increases with the applied strain rate. To calculate the individual probability component $P_{s,r}$ of Eq. (3.26), one would need to determine the load redistribution among the facets as damage proceeds. This requires performing the nonlinear stochastic discrete element simulations, which is computationally intensive. Nevertheless, the recent results of the fishnet analysis indicate that the exponent of the power-law tail of the strength distribution of the system increases in proportion to the dominant number of damaged facets (i.e. k in Eq. (3.26)) [99]. This explains the observed in the current study increase in the Weibull modulus with an increasing strain rate.

The decrease in the grafting probability indicates that the strength distribution of the static RVE approaches the Gaussian distribution. This can be physically related to the increasing number of damaged facets, which implies that the failure process becomes more ductile. Since more facets contribute to the failure of the static RVE, we expect that the standard deviation would decrease considerably. However, it is also noted that the random mesostructure causes a considerable variability of the stress field, and this variability is further enhanced by the inertia effect. Therefore, the stress field becomes more random at high strain rates, which leads to a larger standard deviation of the overall nominal strength. This effect counteracts the aforementioned decrease in the standard deviation due to the increasing number of damaged facets. As shown in Fig. 3.9, the calibration results show that the overall standard deviation of the strength of the static RVE decreases mildly with an increasing strain rate.

The calibrated rate-dependent weakest-link model is now used to predict the size effect curves of the standard deviation for different applied strain rates. Fig. 3.10 shows that the model prediction agrees well with the simulation results. It is seen that, in contrast to the diminishing size effect on the mean nominal strength at high strain rates, the size effect on the standard deviation becomes more pronounced as the strain rate increases. At low strain rates, the standard deviation exhibits an intricate size effect ending with a power-law asymptote at the large-size limit. This theoretical power-law asymptote is attributed to the fact that, according to the weakest-link model, at low strain rates the strength distribution of large-size specimens would approach the Weibull distribution, i.e. $P_f(\sigma_N) = 1 - \exp[-(D/l_0)^2(\sigma_N/s_0)^m]$. The corresponding standard deviation of σ_N can be written as

$$\delta_{\sigma_N} = s_0 \left(\frac{l_0}{D} \right)^{2/m} \sqrt{\Gamma\left(1 + \frac{2}{m}\right) - \Gamma^2\left(1 + \frac{1}{m}\right)} \quad (3.27)$$

where $\Gamma(x)$ = Eulerian gamma function. Eq. (3.27) indicates that, at low strain rates, the asymptotic size effect on the standard deviation is very weak since m is usually a large number.

For the high strain rates considered in this study ($\dot{\epsilon} > 10^5/\text{s}$), the fitting of the mean size effect curve indicates that the specimen size is smaller than the RVE size. According to Eq. (3.18), we have $n_b = (D/l_{0s})^2$. Therefore, the statistics of the nominal strength of the specimen is modeled by a plastic bundle, and the scaling of the standard deviation is given by Eq. (3.23). It can be easily shown that, as n_b increases (i.e. $n_b > 4$), Eq. (3.23) is approximately equivalent to:

$$\delta_G(\dot{\epsilon}) = \frac{\delta_{G0}q(\dot{\epsilon})}{\sqrt{n_b}} = \delta_{G0}q(\dot{\epsilon})l_{0s}D^{-1} \quad (3.28)$$

We note that the size effect expressed by Eq. (3.28) is much stronger than that predicted by the

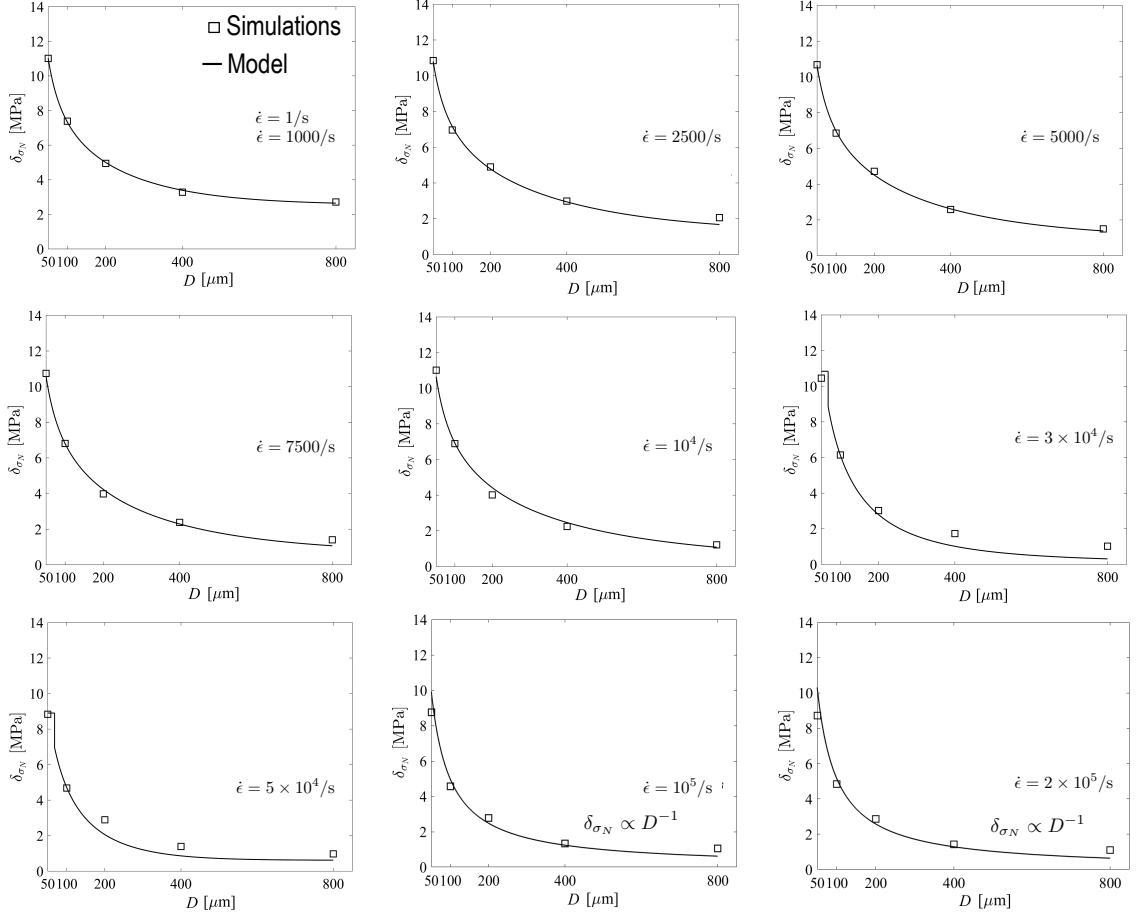


Figure 3.10: Simulated size effects on the standard deviation of nominal strength at different strain rates and its comparison with the rate-dependent finite weakest-link model

Weibull distribution. From Fig. 3.10, we see that Eq. (3.28) agrees well with the simulated size effect on the standard deviation at high strain rates.

The foregoing analysis elucidates the size and rate dependence of the functional form of the strength distribution. At low strain rates, the strength distribution of the specimen transitions from a Gaussian distribution modified by a far-left Weibull tail to a purely Weibull distribution as the specimen size increases. At increasing strain rates, for the specimens considered in this study, the strength distribution becomes predominantly Gaussian with a size independent mean value which increases with the rate, but with a standard deviation that decreases strongly with the specimen size. This transitional behavior is well captured by the proposed rate-dependent weakest-link model.

3.3 Conclusions

This study shows that the strain rate has a profound influence on the scaling of the nominal tensile strength of quasibrittle structures. This rate dependence arises from the influence of the strain rate on the failure behavior of the structure. The discrete element model simulations show that the structure exhibits a more diffused cracking pattern as the strain rate increases, which explains the observed diminishing mean size effect at high strain rates. Meanwhile, the rate-dependent failure behavior also leads to different scaling behavior of the standard deviation of the nominal strength at different strain rates. It is shown that, for a given strain rate, the standard deviation decreases with an increasing specimen size. At high strain rates, this decreasing trend becomes stronger and it exhibits a power-law scaling behavior. The result also indicates, that, for a given specimen size, an increasing strain rate leads to a reduction in the standard deviation of nominal strength.

It is shown that the simulated rate and size effects on the mean and standard deviation of the nominal tensile strength can be well captured by a rate-dependent finite weakest-link model. The model employs a rate-dependent length scale, which physically represents the transition from damage localization to diffused damage with an increasing strain rate. The model directly predicts the combined rate and size effects on the probability distribution of nominal strength. At low strain rates, the strength distribution varies from a predominantly Gaussian distribution to a Weibull distribution as the specimen size increases, whereas at high strain rates, the strength distribution is Gaussian for a significantly large range of specimen sizes. The developed rate-dependent finite weakest-link model provides an analytical tool to model the rate and size effects on the probability distribution of nominal tensile strength of quasibrittle structures, which could be implemented into stochastic FE simulations of quasibrittle fracture under various strain rates. More specifically, considering that each finite element represents a material element of finite size, the present model indicates that the input probability distribution of tensile strength of finite elements should depend on the failure mechanism, which was shown to be influenced by both the element size and applied strain rate. The above is an essential consideration for mitigating mesh dependence of the output probabilistic response in continuum finite element simulations of quasibrittle structures with random material properties.

Chapter 4

Stochastic Numerical Simulations of Strain-Softening Continua

Chapter 3 investigated the size effects on the statistics of structural strength of quasibrittle structures through stochastic discrete element model computations. The simulated set of quasibrittle specimens of different sizes exhibited different failure mechanisms ranging from fairly localized to purely diffused, which were triggered by application of various uniform tensile strain rates, from quasi-static up to the high strain-rate regime. It is clear that the observed failure mechanism governs the mathematical formulation of probabilistic models of structural failure. For instance, the well-established weakest-link and fiber-bundle models statistically represent the failure mechanisms of damage localization and distributed damage respectively. The developed rate-dependent finite weakest-link model transitions from a weakest-link to a fiber-bundle model representation of structural failure as the damage pattern changes from localized damage to distributed cracking with an increasing strain rate. Such transition was achieved by introducing rate dependence of the statistical parameters of the strength distribution. The model was shown to accurately capture the simulated size and rate-dependent mean and standard deviation of structural strength.

The aforementioned study has important implications for mitigating the mesh sensitivity of the output probabilistic structural response in stochastic FE simulations of strain-softening continua, which is the topic of the present chapter. The stochasticity of peak load capacity arises from the spatial variability of element tensile strength and fracture energy. Focus is placed on the case when the finite element mesh size is larger than the crack band width of the material, as well as the autocorrelation length of the underlying random field of constitutive properties. Considering that

each finite element represents a material element of finite size, the sampling probability distributions of the input tensile strength and fracture energy are related to the failure mechanism of the corresponding element. This is achieved by introducing a dependence of the distribution functions of apparent fracture properties on proposed numerical parameters, some of which were introduced in Chapter 2, that are able to capture the actual evolution of damage pattern including the stages of damage initiation, localization and propagation. Therefore, the present formulation of the probability distributions of fracture properties and the mechanism-based energy regularization scheme of Chapter 2 are interconnected and are always consistent with the actual failure mechanism of the structure. Besides, the explicit dependence of the present probabilistic model on the damage mechanism makes it applicable to general loading scenarios, including rate effects, and thus resulting in a more general approach than the rate-dependent weakest link model of Chapter 3, which was also published in [91]. The model is applied to simulate the stochastic failure behavior of quasibrittle structures of different geometries, subjected to different loading configurations. The numerical examples are selected such that various failure mechanisms are triggered and therefore the generality of the method can be tested. It is shown that the proposed model is efficient in mitigating mesh dependence of the output strength statistics in all considered cases, thus the present study provides a general framework for addressing the issue of mesh dependence in stochastic FE simulations of quasibrittle failure.

4.1 Model Formulation

4.1.1 Probabilistic Modeling of Element Fracture Properties

The constitutive law to which our probabilistic model is applied was formulated in Chapter 2 and is briefly described here. We consider an isotropic continuum damage mechanics model, written in general form as

$$\boldsymbol{\sigma} = f(\omega)\mathbf{C} : \boldsymbol{\epsilon} \quad (4.1)$$

where \mathbf{C} is the elastic stiffness tensor, ω is a scalar damage variable ranging from 0 to 1, $\boldsymbol{\epsilon}$ is the infinitesimal strain tensor, and $f(\omega)$ is a function which describes stiffness degradation of the bulk material due to damage. The constitutive law is defined by the following parameters: E = Young's modulus, ν = Poisson's ratio, f_{t0} = tensile strength, G_{f0} = mode I fracture energy, and h_0 = crack band width, from which we model only the tensile strength and fracture energy as statistically independent random variables, since these are governing the failure behavior. The subscript "0" is

used to denote the true material properties, which are defined for an element of size equal to the crack band width h_0 . The current analysis focuses on the case of finite elements of size larger than the crack band width, and aims to formulate the probabilistic models of apparent tensile strength f_t and fracture energy G_f of such elements. It should be noted that the proposed sampling distributions of apparent tensile strength and fracture energy of a given finite element need to be related to both the inherent randomness of the corresponding material properties, as captured by the probability distributions of f_{t0} and G_{f0} , as well as the failure mechanism experienced by the element, which will be quantified from proposed numerical parameters resembling the localization parameter introduced in Chapter 2.

Following the notation of Chapter 2, let us consider a finite element of in-plane dimensions h_1 and h_2 , where h_1 denotes the element dimension perpendicular to the direction of incipient crack propagation, and h_2 the dimension orthogonal to h_1 (Fig. 4.1). According the fictitious crack model [74], cracks are considered to initiate and propagate inside an element as soon as its tensile strength is reached. Denoting as n_f the number of potential damage zone locations from which fracture can initiate inside the element, we can expect that, due to the spatial variability of material strength, the location of damage zone formation inside an element is intrinsically random, and in this case $n_f = h_1/h_d$, where h_d is the size of the damage zone, to be determined from the failure pattern of the element. However, in the presence of significant stress concentration, for instance due to a propagating crack from the neighboring elements into the element of interest, there is only one possible damage zone location from which fracture can initiate in the considered element, dictated by mechanics rather than material randomness.

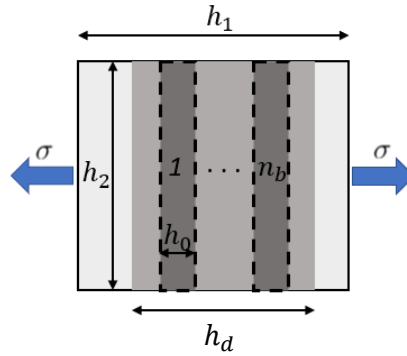


Figure 4.1: A finite element with a damage zone consisting of n_b number of crack bands

Based on the foregoing discussion, we consider a weakest-link statistical representation of element

failure, which reflects the randomness in the location of damage zone formation inside the element. The probability distribution P_{f_t} of the tensile strength of a finite element can thus be expressed as:

$$P_{f_t}(\sigma) = 1 - [1 - P_{f_t}^b(\sigma)]^{n_f} \quad (4.2)$$

where $n_f = h_1/h_d$ and $P_{f_t}^b$ is the probability distribution of strength of each damage zone, whose size can vary between h_0 and h_1 depending of the failure mechanism of the element. For instance, $h_d = h_0$ for localized damage through the formation of a single crack band, whereas $h_d = h_1$ for purely diffusive damage inside the element. Based on Eq. (4.2), the entire element will fail under controlled loads as soon as a single damage zone is formed.

The damage zone, by definition, experiences diffusive microcracking, therefore we statistically represent it by a fiber-bundle model, which is suitable to describe this failure mechanism. In the fiber-bundle model, the structure is modeled as a set of elements, called fibers, which are coupled in parallel. Once a fiber fails, its load is redistributed among other surviving fibers, this way preventing global failure. In this study, we consider that each fiber in the bundle model of the damage zone represents a potential fracture process zone (FPZ) of width h_0 , and denote as $n_b = h_d/h_0$ the number of fibers in the bundle (Fig. 4.1). The crack band width is usually a few times the size of material heterogeneities, and thus the reference element of size $h_1 = h_0$ is expected to exhibit a gradual softening stress-strain behavior. To simplify the mathematical formulation of the distribution of element strength, we assume that each fiber in the bundle model of the damage zone exhibits an elastic-perfectly plastic stress-strain behavior, for which case the bundle strength is a weighted sum of the strengths of the individual fibers. It has been shown [18] that the FPZ, which in our case is represented by the elements of the bundle model, has a strength distribution that can be approximated by a Gauss-Weibull grafted cumulative distribution function (cdf)

$$P_1(\sigma) = \begin{cases} 1 - \exp(-\langle\sigma/s_0\rangle^{m_0}) \approx \langle\sigma/s_0\rangle^{m_0} & (\sigma \leq \sigma_{\text{gr}0}) \\ P_{\text{gr}0} + \frac{r_{f0}}{\delta_{G0}\sqrt{2\pi}} \int_{\sigma_{\text{gr}0}}^{\sigma} e^{-(x-\mu_{G0})^2/2\delta_{G0}^2} dx & (\sigma > \sigma_{\text{gr}0}) \end{cases} \quad (4.3a)$$

$$P_1(\sigma) = \begin{cases} 1 - \exp(-\langle\sigma/s_0\rangle^{m_0}) \approx \langle\sigma/s_0\rangle^{m_0} & (\sigma \leq \sigma_{\text{gr}0}) \\ P_{\text{gr}0} + \frac{r_{f0}}{\delta_{G0}\sqrt{2\pi}} \int_{\sigma_{\text{gr}0}}^{\sigma} e^{-(x-\mu_{G0})^2/2\delta_{G0}^2} dx & (\sigma > \sigma_{\text{gr}0}) \end{cases} \quad (4.3b)$$

where m_0 and s_0 are the Weibull modulus and scale parameter of the Weibull tail, respectively, μ_{G0} and δ_{G0} are the mean and standard deviation of the Gaussian core if considered extended to $-\infty$; r_{f0} is a scaling parameter required to normalize the grafted cdf such that $P_1(\infty) = 1$, $\sigma_{\text{gr}0}$ = grafting stress, and $P_{\text{gr}0} = (\sigma_{\text{gr}0}/s_0)^{m_0}$ = grafting probability. The continuity of the probability density function (pdf) at the grafting point requires that $[dP_1/d\sigma]_{\sigma_{\text{gr}0}^+} = [dP_1/d\sigma]_{\sigma_{\text{gr}0}^-}$. Therefore, there are in total four independent parameters that define the grafted distribution of the fiber strength, which

in this study are taken to be $\bar{f}_{t0} = \mu_{G0}$, $\omega_0 = \delta_{G0}/\mu_{G0}$, m_0 , and P_{gr0} .

Because the crack band width h_0 can be considered to be larger than the autocorrelation length of the underlying random field of material strength, the fiber strengths can be treated as statistically independent random variables. The plastic fiber-bundle model of the damage zone implies that the cdf of bundle strength also follows a Gauss-Weibull grafted cdf, $P_{f_t}^b = P_1(\bar{f}_t, \omega, m, P_{gr})$, which can be defined by the four statistical parameters \bar{f}_t , ω , m , and P_{gr} representing the mean and coefficient of variation of the Gaussian core of bundle strength, and the Weibull modulus and grafting probability of its power-law tail respectively. According to the statistics of the sum of independent Gaussian variables and the mathematical properties of the plastic fiber-bundle model, the statistical parameters of the Gauss-Weibull cdf of bundle strength are given from the following equations relating them to the corresponding parameters of the individual fibers [91, 126]

$$\bar{f}_t = \bar{f}_{t0} \quad (4.4)$$

$$\omega = \frac{\omega_0}{n_b} \left[\lceil n_b \rceil - 1 + (n_b + 1 - \lceil n_b \rceil)^2 \right]^{1/2} \quad (4.5)$$

$$m = m_0 \lceil n_b \rceil \quad (4.6)$$

$$P_{gr} = (P_{gr0}/\lceil n_b \rceil)^{\lceil n_b \rceil} \quad (4.7)$$

where it was considered that the bundle contains $\lceil n_b \rceil - 1$ number of fibers with area A_0 and a single fiber with area $(n_b + 1 - \lceil n_b \rceil) A_0$, in order to ensure that the number of fibers is always an integer, even if the quantity n_b , which will be determined from numerical parameters quantifying the damage pattern of an element (Eqs. (4.22), (4.23)), is non-integer.

Even though the weakest-link representation of element strength is suitable for failures featured by damage localization, the proposed model of Eq. (4.2) is able to represent different failure mechanisms, because the quantities n_f and n_b governing the scaling of the strength distribution are not predetermined constants. Instead, they are calculated during the simulation and can evolve according to the actual failure mechanism of the element. At this point, it can be illustrative to provide the limiting values of n_f and n_b during the three stages that are generally present in any quasibrittle failure process, which are: 1) damage initiation, characterized by a diffused damage pattern through the formation of multiple microcracks, 2) damage localization, during which the previously formed microcracks coalesce into a single macrocrack, and 3) damage propagation, characterized by propagation of the developed macrocrack leading to ultimate failure. Based on the definitions of n_f and n_b , for a given element we should thus have: 1) $n_f = 1$ and $n_b = h_1/h_0$ during damage initiation,

since the zone of diffusive cracking (damage zone) occupies the entire element, 2) $n_f = h_1/h_0$ and $n_b = 1$ during damage localization, since a single crack has been formed in the element out of the h_1/h_0 possible cracks with random locations of formation, 3) $n_f = 1$ and $n_b = 1$ during propagation of a band of localized strains from the neighboring elements into the considered element, since stress concentration due to damage localization in the neighbors determines the location of crack band formation in the considered element.

As will be shown later, the mathematical expressions based on which n_f and n_b will be calculated satisfy these limits, and upon their substitution to Eq. (4.2), it can be seen that, in cases of diffusive damage, the entire element is statistically represented by the fiber-bundle model, in the case of damage localization, the proposed model transitions to the weakest-link representation of element failure, and in the case of damage propagation, the distribution of element strength coincides with the Gauss-Weibull strength cdf of the reference element of size equal to the crack band width (Eq. (4.3)). For all cases lying between purely diffused and purely localized damage, the proposed model is transitional among the fiber-bundle, the weakest-link, and the constant distribution models. It is also important to note that the dependence of the probability distributions of constitutive properties on the damage pattern, as introduced in the present model, requires an assumption for the cdf of tensile strength f_t at the initial state, if undamaged. Since the randomness of material properties can precipitate damage localization, we assume a weakest-link representation of structural failure prior to damage initiation, whereas after the onset of damage the proposed model evolves during the simulation according to the actual damage pattern. Eqs. (4.2), (4.3) and (4.4)-(4.7) provide the formulation of the probability distribution of tensile strength of a given finite element, which is governed by its failure mechanism.

The probabilistic model of apparent fracture energy G_f , which is the second constitutive parameter modeled as random variable in the present study, will be derived from energetic considerations during propagation of n_b number of crack bands of width h_0 inside the damage zone formed in the corresponding element. The energy required (per unit thickness) for simultaneous advancement of n_b cracks by the same distance δa under quasi-static conditions and assuming fracture as the only dissipative process, is equal to $n_b G_f \delta a = n_b G_f h_2 \delta \omega$, where G_f represents the apparent fracture energy of the element under mode I conditions and $\delta a = h_2 \delta \omega$, based on our interpretation of the damage variable in Chapter 2. Crack growth is made possible through the release of strain energy from the entire element during the increment of the crack length(s) δa , which can be written as $h_1 h_2 \delta U$, where U represents a free energy function that governs tensile failure. The energy balance

equation in the limit of $\delta a \rightarrow 0$, and thus $\delta \omega \rightarrow 0$, yields

$$\frac{\partial U}{\partial \omega} + \frac{G_f}{h_1} n_b = 0 \quad (4.8)$$

The fracture energy is defined as the energy required to create a unit of new crack surface area. For this general case considered, with $1 \leq n_b \leq h_1/h_0$ number of crack bands that could be developed inside the element, the total energy dissipated in failure is

$$E_d = \sum_{i=1}^{n_b} A_{si} G_{fi} \quad (4.9)$$

where G_{fi} and A_{si} denote the fracture energy and surface area of crack i , respectively, and it is considered that the fracture energies of all crack bands are statistically independent and identically distributed random variables. In case when n_b is not an integer, we consider that inside the element there have been formed $\lceil n_b \rceil - 1$ number of cracks with surface area A_{s0} and a single crack with area $(n_b + 1 - \lceil n_b \rceil) A_{s0}$. The apparent fracture energy of the element can be obtained by dividing Eq. (4.9) with the total surface area of all developed cracks, thus

$$G_f = \frac{\sum_{i=1}^{\lceil n_b \rceil - 1} A_{s0} G_{fi} + (n_b + 1 - \lceil n_b \rceil) A_{s0} G_{f0}}{n_b A_{s0}} \quad (4.10)$$

Eq. (4.10) represents a weighted sum of statistically independent random variables, thus, following the Central Limit Theorem (CLT), the distribution of apparent fracture energy G_f will approach the Gaussian distribution when sufficiently large number of cracks have been developed, thus when failure is characterized by a purely diffusive damage pattern.

In the present study, we consider that the fracture energies of elements of size equal to the crack band width h_0 , which represent the actual material properties, are Gaussian random variables with the same mean \bar{G}_{f0} and coefficient of variation ω'_0 , i.e. $G_{fi} \sim N(\bar{G}_{f0}, \omega'_0)$. Therefore, the apparent fracture energy of the element will also follow the Gaussian distribution even if n_b is not large enough for the CLT to hold, with the following parameters:

$$G_f \sim N\left(\bar{G}_{f0}, \frac{\omega'_0}{n_b} \left[\lceil n_b \rceil - 1 + (n_b + 1 - \lceil n_b \rceil)^2\right]^{1/2}\right) \quad (4.11)$$

Based on Eq. (4.11), in cases when failure of an element is featured by damage localization due to a single crack that has either been formed inside the element or is about to propagate from its neighbors, $n_b = 1$, and so the distribution of the apparent fracture energy of the element coincides

with that of the fracture energy of a single crack band, $G_f \sim N(\bar{G}_{f0}, \omega'_0)$. In cases of multiple crack formation, the mechanics of energy dissipation lead to a size dependence of the coefficient of variation of apparent fracture energy which decreases with the element size, and a size independent mean.

Having completed the formulation of our probabilistic model of apparent fracture properties, we can now combine it with our mechanism-based energy regularization scheme (Chapter 2). We thus focus on Eq. (4.8), which is a general energy balance equation applicable to different failure mechanisms depending on the value of n_b . Eq. (4.8) is equivalent to Eq. (2.5) which is also reproduced below, if the energy regularization function g is related to quantity n_b as in Eq. (4.13).

$$\frac{\partial U}{\partial \omega} + \frac{G_f}{h_0} g = 0 \quad (4.12)$$

$$g = \left(\frac{h_0}{h_1} \right) n_b \quad (4.13)$$

Similarly to Chapter 2, function g transitions from 1 in cases of a purely diffused damage pattern to h_0/h_1 in the case of damage localization. It has also been shown (Chapter 2 and [68]), that satisfaction of the general energy balance equation (Eqs. (4.8) or (4.12)) by the damage mechanics constitutive law is essential in order to preserve correct energy dissipation during failure regardless of the spatial discretization, and thus ensure the mesh-objectivity of finite element simulations of strain-softening continua in the deterministic setting. In the case of failure with damage localization, i.e. $n_b = 1$ and Eq. (4.8) implies a size-dependent input constitutive behavior, which is essential for mitigating the otherwise mesh-dependent simulated structural response [17, 68]. Additionally, the size dependence of the input sampling distributions of f_t and G_f arising due to the failure mechanism of a given element and described by the current probabilistic model (Eqs. (4.2), (4.4)-(4.7) and (4.11)), will be shown to be effective in mitigating the mesh dependence of the output first and second statistical moments of structural strength in the present case of stochastic analysis. From Eqs. (4.12) and (4.13), it can be seen that the energy regularization scheme and the probabilistic models of fracture properties are interconnected, since the term n_b is present in both the general energy balance equation as well as the distribution functions of f_t and G_f .

Finally, we reproduce below the expressions for the damage function $f(\omega)$ and the damage evolution law $\omega(\bar{\epsilon})$ as taken from Chapter 2, which are required along with Eq. (4.1) to fully define our constitutive model:

$$f(\omega) = \frac{1 - \omega}{1 - a\omega} \quad (4.14)$$

$$\omega = \frac{1}{a} - \frac{\bar{\epsilon}}{a} \sqrt{\frac{h_0 E (1 - a)}{2 G_f g}} \quad (4.15)$$

$$a = 1 - \frac{2 E G_f g}{h_0 f_t^2} \quad (4.16)$$

where a is a parameter which depends on the material properties as well as the energy regularization function g , not to be confused with the crack length a for which the same notation was used, and $\bar{\epsilon} =$ Mazar's equivalent strain (Eq. 2.8). Damage is allowed to initiate only after the equivalent strain $\bar{\epsilon}$ exceeds the threshold value $\epsilon_0 = f_t/E$ related to the element tensile strength, and the damage variable is irreversible, i.e. $\dot{\omega} \geq 0$. Eqs. (4.1), (4.14), (4.15) as well as Eqs. (4.2) and (4.11) complete the description of mechanical and probabilistic response of a material element of finite size, which are intimately tied to its failure mechanism.

4.1.2 Description of the Local Damage Pattern

The probabilistic and constitutive models described in Section 4.1.1 require the calculation of quantities n_f and n_b , representing the number of potential damage zones inside an element and the number of crack bands inside the damage zone respectively. It is clear that these quantities should be related to the damage pattern of the corresponding finite elements. In this section, we introduce two numerical parameters which capture the evolving damage pattern around each element, and continue to describe the details of their implementation within the finite element procedure. Quantities n_f and n_b can then be determined by the introduced numerical parameters based on proposed expressions.

The first numerical parameter is called the localization parameter $\delta_{\omega 1}$ and has the same physical meaning as parameter δ_{ω} introduced in the energy regularization scheme of Chapter 2. $\delta_{\omega 1}$ aims to describe the level of damage localization inside a given finite element. The value of $\delta_{\omega 1}$ ranges from 0, representing the case when the considered element is either under a diffused damage state or when damage localization cannot occur, to δ_{1m} , representing a fully localized damage pattern. The second parameter, $\delta_{\omega 2}$, is called the propagation parameter. Its minimum value is 0, corresponding to the case when it is unlikely that a crack from the neighboring finite elements will propagate into the element of interest, and its maximum value is δ_{2m} , corresponding to the case when damage propagation will most certainly occur.

In the finite element implementation of our constitutive model, we follow the procedure outlined below to determine parameters $\delta_{\omega 1}$ and $\delta_{\omega 2}$, which is suitable for the case when linear shape functions are used for the interpolation of the displacement field. For a given finite element i , we initially

compute its average strain tensor from the corresponding strain values at all the element Gauss points. We denote as \vec{n}_e the unit vector with the direction of maximum principal average strain at the onset of damage. It is considered that cracks will form in the direction perpendicular to \vec{n}_e , which is kept constant after damage initiation, as assumed in the fixed crack model. Length h_1 can now be calculated by projecting the element onto the direction of \vec{n}_e and has therefore the same value for all Gauss points of a given element, while length h_2 will correspond to the element dimension orthogonal to h_1 . At every Gauss point of element i , we construct the unit vectors \vec{v}_{ij}^g connecting the current Gauss point with the centroid of neighboring element j (Fig. 4.2), and among all possible connection vectors, we identify those that are most closely aligned with the vector \vec{n}_e , and denote them as \vec{v}_{m1}^g and \vec{v}_{m2}^g . The localization parameter of every Gauss point $\delta_{\omega 1}$, can then be calculated as follows

$$\delta_{\omega 1} = \left\langle 1 - \frac{\hat{\omega}_{i1} + \hat{\omega}_{i2}}{2\hat{\omega}_i} \right\rangle^s \quad (4.17)$$

where $\langle x \rangle = \max(x, 0)$, $\hat{\omega}_i$ = characteristic damage level of element i , and $\hat{\omega}_{i1}, \hat{\omega}_{i2}$ = characteristic damage levels of the two adjacent elements that are along the directions of \vec{v}_{m1}^g and \vec{v}_{m2}^g . From the definition of $\delta_{\omega 1}$ in Eq. (4.17), it is observed that $\delta_{\omega 1}$ is equal to 0 in the case of uniform distribution of the damage $\hat{\omega}$ along the direction perpendicular to the crack path, as well as in the case when the characteristic damage level of element i is lower than the average of the characteristic damage levels of its adjacent elements most closely aligned with \vec{n}_e , since localization of damage in element i is unlikely to occur under the conditions of the second case. $\delta_{\omega 1}$ attains its maximum value δ_{1m} when a fully localized damage pattern is observed, i.e. only the element of interest i experiences damage, whereas its neighboring elements along the directions of \vec{v}_{m1}^g and \vec{v}_{m2}^g are undamaged.

The second parameter introduced in the present model is the propagation parameter $\delta_{\omega 2}$, which is calculated for every Gauss point of the considered element i as follows:

$$\delta_{\omega 2} = \max_j \left[\overline{\delta_{\omega 1 j}}^p (1 - \|\vec{n}_e \cdot \vec{v}_{ij}^g\|)^q \right] \quad (4.18)$$

where $\overline{\delta_{\omega 1 j}}$ is the average value of the localization parameter at a neighboring element j , and the exponents p and q are set equal to 1 and 2 respectively. $\delta_{\omega 2}$ is calculated as the maximum of the inside the brackets quantity in Eq. (4.18) among all neighboring elements j . Based on Eq. (4.18), the propagation parameter is taken equal to the average localization parameter of the neighboring element that is most closely aligned with the direction of crack propagation inside element i , since it is reasonable to consider that, after damage localizes in this specific neighbor, the developed crack will propagate into the element of interest. Here one could note that, in contrast to $\delta_{\omega 1}$, which

aims to describe the level of damage localization inside a given element and is affected by both the damage state of this element as well as that of its neighbors in the direction perpendicular to the crack path, parameter $\delta_{\omega 2}$ does not take into account the damage pattern of the element of interest, but only that of its neighbors along the crack direction.

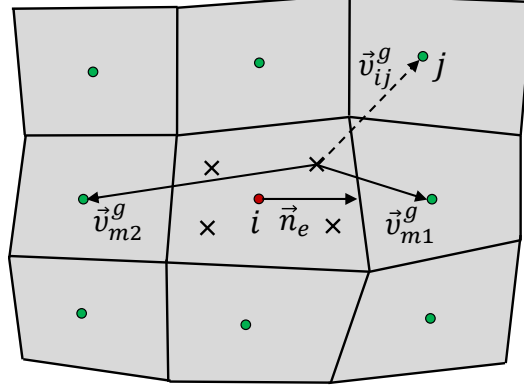


Figure 4.2: Schematic of finite element mesh for calculation of the localization and propagation parameters

The characteristic damage levels $\hat{\omega}_k$ employed for the calculation of the localization and propagation parameters, where k denotes the index of the corresponding element, are defined as follows:

$$\hat{\omega}_k = \alpha_w \bar{\omega}_k + (1 - \alpha_w) \left(\frac{\bar{\omega}_{k-1} + \bar{\omega}_{k+1}}{2} \right) \quad (4.19)$$

where $\bar{\omega}_k$ denotes the average damage level of element k , as calculated by using the damage values at all Gauss points of the element, $\bar{\omega}_{k-1}, \bar{\omega}_{k+1}$ are the average damage levels of its neighboring elements along the direction perpendicular to the direction of crack propagation inside element k , and α_w is a selected weighting coefficient in the interval $(0, 1]$. In the case of $\alpha_w < 1$ considered in the present study, the characteristic damage level of a given element k is a nonlocal quantity, since it additionally contains information of the average damage levels of elements $k - 1$ and $k + 1$. Introduction of a nonlocal damage quantity for the determination of parameters $\delta_{\omega 1}$ and $\delta_{\omega 2}$ is essential in the case of random properties considered here, since, due to the spatial variability of fracture properties, a diffusive damage pattern of the structure may not be characterized by a homogeneous distribution of damage, even for loadings that create a uniform strain field. Thus, calculation of the localization parameter $\delta_{\omega 1}$ from the nonlocal damage levels of the corresponding elements ensures that it will not reach its maximum value indicating full localization, when there exist weak spatial variations of

the damage variable inside a predominantly diffused damage pattern. The maximum value of the localization parameter can now be calculated from Eqs. (4.17) and (4.19) applied to a fully localized damage pattern, i.e. only the element of interest i is damaged, whereas its neighbors 1 and 2 are undamaged. This yields:

$$\delta_{1m} = \left\langle \frac{3\alpha_w - 1}{2\alpha_w} \right\rangle^s \quad (4.20)$$

Based on Eq. (4.18), we can also calculate the maximum value of the propagation parameter $\delta_{\omega 2}$

$$\delta_{2m} = \delta_{1m}^p \quad \text{if } p > 0 \quad (4.21)$$

where $p = 1$ in the present study, so the maximum values of the localization and propagation parameters coincide. We should also note that in the initial, undamaged state, $\delta_{\omega 1}^0 = \delta_{1m}$ and $\delta_{\omega 2}^0 = 0$. As will be shown (Eqs. (4.22)-(4.24)), these initial conditions ensure that the tensile strength f_t is sampled from a weakest-link model of h_1/h_0 number of links prior to damage initiation, consistent with our previously mentioned assumption in Section 4.1.1.

Having proposed expressions for the localization and propagation parameters $\delta_{\omega 1}$ and $\delta_{\omega 2}$ in terms of the characteristic damage levels, we can quantitatively capture the failure mechanism of any element, and use this information inside the energy regularization scheme as well as for the determination of quantities n_b and n_f . We introduce the following equation for the energy regularization function g , which scales the post-peak part of the input constitutive law according to the failure mechanism of the element, so as to ensure correct amount of energy dissipation:

$$g = \frac{h_0}{h_1} + \left(1 - \frac{h_0}{h_1}\right) \left\{ 1 - \left[\frac{\langle \delta_{\omega 1} - \delta_{t1} \rangle}{\delta_{1m} - \delta_{t1}} \right]^\kappa \right\} \left\{ 1 - \left[\frac{\langle \delta_{\omega 2} - \delta_{t2} \rangle}{\delta_{2m} - \delta_{t2}} \right]^\lambda \right\} \quad (4.22)$$

where δ_{t1} , δ_{t2} , κ , λ are parameters to be determined from numerical simulations. For $\delta_{\omega 2} = 0$, $\delta_{t1} = 0$ and $\alpha_w = 1$, Eq. (4.22) is equivalent to $g = 1 + \left(\frac{h_0}{h_1} - 1\right) \delta_{\omega 1}^\kappa$, a functional form which, when combined with a similar definition of the localization parameter $\delta_{\omega 1}$ (Eq. (4.17)), has been shown (Chapter 2) to be efficient in mitigating mesh dependence of deterministic finite element simulations of structures made of strain-softening materials under general failure mechanisms [68]. Solving Eq. (4.13) with respect to n_b , we get:

$$n_b = \frac{h_1}{h_0} g \quad (4.23)$$

and below, we introduce the relation for the number of potential damage zones n_f inside an element

$$n_f = \frac{h_1}{n_b h_0} + \left(1 - \frac{h_1}{n_b h_0}\right) \left[\frac{\langle \delta_{\omega 2} - \delta_{t2} \rangle}{\delta_{2m} - \delta_{t2}} \right]^\lambda \quad (4.24)$$

Eqs. (4.22)-(4.24) recover the limiting behaviors of function g and of quantities n_b and n_f , including damage initiation ($\delta_{\omega 1} = 0$, $\delta_{\omega 2} = 0$), localization ($\delta_{\omega 1} = \delta_{1m}$, $\delta_{\omega 2} = 0$), and propagation ($\delta_{\omega 2} = \delta_{2m}$). Section 4.1 has provided a complete description of the probabilistic and constitutive model, which are interconnected through the energy regularization scheme. The remaining sections of the current chapter present the application of the model in stochastic FE simulations of quasibrittle structures experiencing different failure mechanisms, and evaluate its efficiency in mitigating mesh dependence of the output strength statistics.

4.2 Numerical Examples

4.2.1 Description of Analysis

The performance of the proposed model in mitigating mesh dependence of the output first and second statistical moments of structural strength is evaluated by its application in stochastic FE simulations of quasibrittle specimens of different geometries under different loading configurations. The simulations are performed in the open-source FEM software OOFEM [115], where the present constitutive and probabilistic models were implemented. A two-dimensional state of plane stress is assumed. The specimens are subjected to the three-point and four-point bending tests, under displacement control conditions. For the three-point bending test, two different structure geometries are considered; an unnotched beam of in-plane dimensions 7.5 mm (length) \times 2.5 mm (depth) (Fig. 4.3), and a notched beam of the same dimensions, with relative notch depth 0.5 and notch width $w = h_0/2$, where h_0 = crack band width (Fig. 4.6). Only the unnotched beam is subjected to the four-point bending test (Fig. 4.8). The beams are made of a dense alumina ceramic, with elastic properties treated as deterministic quantities with values: $E = 370$ GPa and $\nu = 0.24$. The crack band width is set constant and equal to $h_0 = 37.5$ μ m, which is a few times the average grain size of the material.

The tensile strength f_t and fracture energy G_f of different finite elements in the discretization vary spatially and are modeled as statistically independent random variables. Their values are calculated by inverting the input sampling distributions at probability levels which are randomly generated at the beginning of every simulation, and are the same among all Gauss points of a given element. The

probability levels remain constant during each simulation, but the cdfs of fracture properties evolve with the damage pattern of an element, following the current probabilistic model. For comparison purposes, we consider another two probabilistic models of the fracture properties: the weakest-link model and the assumption of constant input distribution functions. More specifically, the three different probabilistic models employed in the simulations are:

- I) The proposed model, where the tensile strength and fracture energy are sampled from the distributions of Eqs. (4.2) and (4.11) respectively, which are related to the actual failure mechanism of the structure through quantities n_f and n_b , and can lead to a transition from a fiber-bundle model statistical representation of failure to a weakest-link model as damage localization emerges from diffusive damage.
- II) The weakest-link model, where the distribution of tensile strength takes the form $P_{f_t} = 1 - (1 - P_1)^{h_1/h_0}$ with P_1 sampled from Eq. (4.3), and the fracture energy follows a Gaussian distribution with size independent statistical parameters corresponding to the properties of an element of size equal to the crack band width, $G_f \sim N(\bar{G}_{f0}, \omega'_0)$. The weakest link model is based on the assumption of structural failure with damage localization.
- III) The assumption of constant distributions, where the material properties of tensile strength and fracture energy are sampled from a Gauss-Weibull grafted cdf, $P_{f_t} = P_1(\bar{f}_{t0}, m_0, \omega_0, P_{gr0})$, and a purely Gaussian distribution $G_f \sim N(\bar{G}_{f0}, \omega'_0)$, respectively, with statistical parameters which do not depend on the element size.

The input statistical parameters of the Gauss-Weibull cdf of material tensile strength are: $\bar{f}_{t0} = 200$ MPa, $\omega_0 = 0.15$, $m_0 = 30$, $P_{gr0} = 5 \times 10^{-3}$, and of the Gaussian distribution of fracture energy are $\bar{G}_{f0} = 50$ J/m², $\omega'_0 = 0.15$. These values characterize the inherent randomness of material properties of an element of size equal to the crack band width. It should be noted that the energy regularization scheme described in Section 4.1.2, Eq. (4.22), is applied to all aforementioned probabilistic models, so that the corresponding deterministic problems are regularized and thus any observed mesh dependence of the output statistics of structural strength when using approaches I)-III) can be mainly attributed to incorrect scaling of the corresponding probability distributions of constitutive properties.

All beams are discretized by a uniform mesh consisting of quadrilateral bilinear elements, using full Gauss integration. To investigate the mesh dependence, three different discretizations of the beams are considered: the reference case, with dimensions of finite elements $h_x = h_0$ and $h_y = h_0$,

where subscripts x, y , denote the directions of the beam span and depth respectively, and two other coarser discretizations, with $h_x = 2h_0$ and $h_x = 4h_0$ whereas h_y is kept constant. The mesh lines are aligned with the direction of overall crack band growth to avoid mesh-induced directional bias, so the element size along the direction of the maximum principal strain h_1 is approximately equal to h_x .

For each loading case and structure geometry, we calculated the mean and standard deviation of the peak load of the structure, as captured from the output load-midpoint displacement diagram. A sufficient number of random simulations was performed, ranging between 300-500, such that convergence of both statistics of peak load is achieved. In all three different probabilistic models used, the parameters of the energy regularization function $\delta_{t1}, \delta_{t2}, \kappa, \lambda$ (Eq. (4.22)) were calibrated such that the mesh dependence of the output mean peak load is alleviated, so the models can then be compared in terms of their ability to mitigate mesh dependence of the second statistical moment of structural strength. The remaining parameters of the model required in Eqs. (4.17)-(4.21) are constant and set equal to: $s = 0.5$, $p = 1$, $q = 2$, $a_w = 0.5$. Parameters $\delta_{t1}, \delta_{t2}, \kappa$, and λ , once calibrated for a given material and a selected probabilistic model (I-III), retain the same values among the different structure geometries and loading configurations.

4.2.2 Unnotched beams under three-point bending

In this section we investigate the performance of all three different cases of sampling of the random variables of element tensile strength f_t and fracture energy G_f (approaches I-III), in terms of their ability to mitigate mesh dependence of the statistics of peak load of three-point bend beams (Fig. 4.3). Fig. 4.4 presents the output mean and standard deviation of peak load, as calculated from 500 random simulations, for all probabilistic models and element sizes $h_x = h_0, 2h_0, 4h_0$. The parameters $\delta_{t1}, \delta_{t2}, \kappa$, and λ have been calibrated separately for each probabilistic model such that the mean size effect is mitigated, as shown in Fig. 4.4 (left). The optimum values of these parameters were found to be: $\delta_{t1} = 0$, $\delta_{t2} = 0$, $\kappa = 1$, $\lambda = 1$ for the proposed model and the case of constant distributions, whereas $\delta_{t1} = 0.7$, $\delta_{t2} = 0.7$, $\kappa = 1$, $\lambda = 1$ for the weakest-link model. Given that all models perform excellent in terms of the mean behavior, we can focus on their ability to mitigate the size dependence of the second statistical moment. In Fig. 4.4 (right), we observe that the optimum result is achieved by the proposed model, which gives a maximum error for the standard deviation of the coarser mesh compared to the reference mesh of approximately 11%, followed by the case of constant distributions with maximum error around 16%. The mesh dependence issue of the output standard deviation when using the weakest-link model is exacerbated.

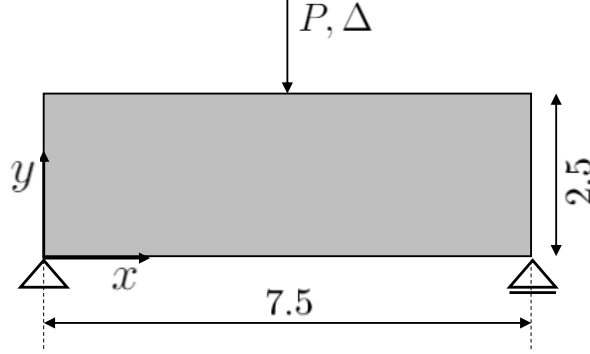


Figure 4.3: Geometry of unnotched beams under three-point bending considered in the simulation (all dimensions are in mm)

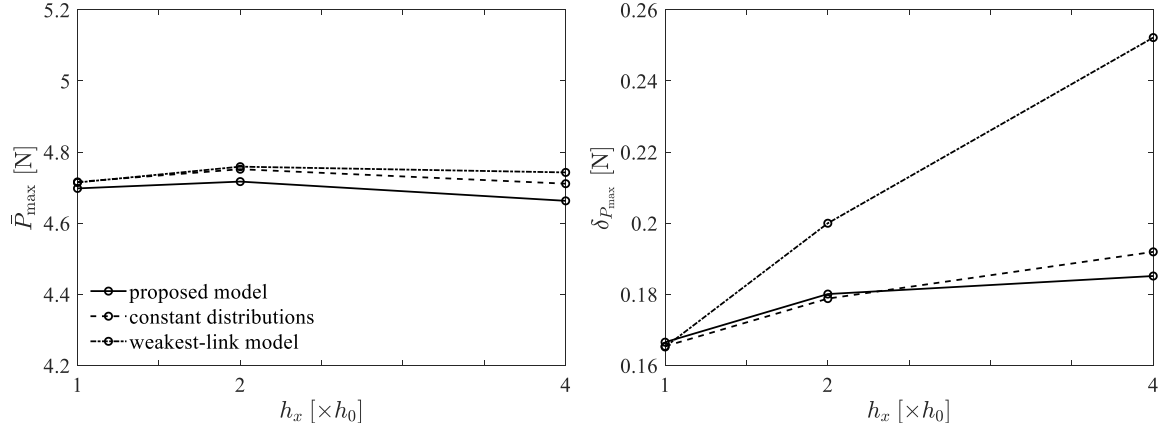


Figure 4.4: Mean (left) and standard deviation (right) of peak load of the unnotched beam under three-point bending with probabilistic models I)-III) ($\bar{G}_{f0} = 50\text{J/m}^2$)

The resulting size dependence of the second statistical moment of structural strength can be explained by the failure mechanism of this unnotched beam under three-point bending. Even though the randomness of material properties can lead to different number of damaged elements as well as different locations of crack initiation between random simulations, when the peak load is reached, the most prevalent failure mechanism of this beam is failure where multiple cracking contributes significantly to the peak load capacity. This means that the maximum load is governed by the contributions of all softening elements inside the damage zone, and is not solely dictated by the strength of the weakest element. Such averaging effect can lead to a decrease in the standard deviation of structural strength with increasing number of elements inside the damage zone. Considering the overall damage zone size being approximately constant, since it is mainly governed by the struc-

ture geometry and loading configuration, a coarser discretization implies fewer elements inside the damage zone, and thus less averaging effect. The above considerations explain why the present simulation results show an increasing trend of the standard deviation of peak load with the mesh size for all three probabilistic models.

The present model has the ability to “feel” the averaging effect because its sampling distributions of fracture properties depend on the localization parameter $\delta_{\omega 1}$, which quantifies the actual damage pattern around each element. In cases of distributed cracking, $\delta_{\omega 1} \ll \delta_{1m}$ so the model will switch from the initial assumption of weakest-link failure to the fiber-bundle model, if there is not significant propagation of localized damage, i.e. $\delta_{\omega 2} \ll \delta_{2m}$. According to the fiber-bundle model, the input CoV of tensile strength and fracture energy is scaled such that larger elements have less variable properties (Eqs. (4.5)-(4.6),(4.11)), and this scaling is shown to significantly mitigate the mesh dependence of the output standard deviation of structural strength, so the increasing trend of standard deviation with the mesh size is insignificant when the proposed model is used. In the case of constant distributions, though, the size dependence of the standard deviation becomes more pronounced, since this approach does not introduce any dependence of the statistics of fracture properties on the element size.

The worst result is obtained when the weakest-link model is used, which leads to a drastic increase of the standard deviation with the mesh size. The weakest-link assumption is inconsistent with the actual failure mechanism of the structure, which justifies the poor performance of this model. More specifically, the weakest-link model assigns lower mean strength to larger elements, in contrast to the fiber-bundle model as well as the case of constant distributions, where the input mean properties are size-independent. An initial set of trial simulations with the weakest-link model and parameters of the energy regularization function g set equal to $\delta_{t1} = 0$, $\delta_{t2} = 0$, $\kappa = 1$, $\lambda = 1$, which were the optimum values of the parameters calibrated for approaches I) and III), resulted in a quite pronounced reduction of the mean peak load of the structure with the mesh size. To improve this result, thresholds δ_{t1} and δ_{t2} were both increased to the value of $0.7 < \delta_{1m} = \delta_{2m} = 0.707$, which means that the energy regularization function g was set equal to 1 for a large part of the damage process, thus no scaling of the post-peak part of the softening law was applied. In the presence of some level of damage localization, absence of energy regularization implied by using $g = 1$, leads to larger elements having higher fracture energy so the mean peak load of these elements increased and counteracted the reduction of mean peak load with the mesh size imposed by the weakest-link sampling, resulting in a mesh-independent mean behavior. However, the output standard deviation exhibits a strong increasing trend with the mesh size, even though the weakest-link model introduces

a scaling of the input CoV such that larger elements have less variable tensile strength, unless the large-size limit is reached, for which the CoV depends only on Weibull's modulus m_0 . The reason for this significant increase in the standard deviation with the mesh size probably lies in the fact that use of $g = 1$ over a large range of the damage process to improve the mean size effect, may be an assumption not reflecting the actual failure mechanism of the beam, which is best quantified when using the calculated values of the localization and propagation parameters $\delta_{\omega 1}$, $\delta_{\omega 2}$ inside the energy regularization scheme, that is when $\delta_{t1} \ll \delta_{1m}$ and $\delta_{t2} \ll \delta_{2m}$. We could also note that, given that the present model, which is transitional among the weakest-link, the fiber-bundle, and the constant distributions models, has the best performance followed by the case of constant distributions, the most prevalent failure mechanism of the considered beam must lie between distributed cracking which, at some locations, localizes and propagates into neighboring elements.

In order to further demonstrate the ability of the proposed model to switch between the different limiting cases of failure with distributed cracking, weakest-link type of failure, and failure due to propagation of localized damage, we now consider a beam of exactly the same geometry (Fig. 4.3), but with reduced input mean material fracture energy from $\bar{G}_{f0} = 50 \text{ J/m}^2$ to 15 J/m^2 . Since in the present study we aim to cover many different failure mechanisms, we now consider a nominally less ductile beam to present a case for which the weakest-link assumption becomes more appropriate. Due to the different material, the relevant parameters δ_{t1} , δ_{t2} , κ and λ need to be recalibrated for each probabilistic model. Their optimum values in this case are: $\delta_{t1} = 0.6$, $\delta_{t2} = 0.6$, $\kappa = 1$, $\lambda = 1$ for the proposed model, $\delta_{t1} = 0$, $\delta_{t2} = 0$, $\kappa = 1$, $\lambda = 1$ for the case of constant distributions, and $\delta_{t1} = 0.7$, $\delta_{t2} = 0.7$, $\kappa = 1$, $\lambda = 1$ for the weakest-link model.

Fig. 4.5 presents the mesh size dependence of the output mean and standard deviation of peak load for all three probabilistic failure models, where convergence was achieved after 300 random simulations. Even though the weakest-link model leads to a non-negligible error for the mean peak load of around 6%, its overall performance in mitigating mesh dependence of both mean and standard deviation of structural strength is significantly improved compared to its application to the previously considered more ductile material. We can expect that further reduction of the fracture energy or increase of the beam size such that failure becomes perfectly brittle will lead to the weakest-link model having the best performance, and our model converging to the weakest-link model. In this study, we considered the first alternative to change the failure type, since increase of the beam size would increase the computational cost. However, the input fracture energy we could use was limited by the snap-back condition, $h_1 < 2EG_f/f_t^2$, which is required by our energy regularization scheme whenever a fully localized damage pattern occurs. Due to the randomness,

the actual sampled element fracture energies can be less than the mean value, which is the initial input in the model, so there is no a priori way to determine the minimum value of input mean fracture energy to avoid snap-back. For the selected value of $\overline{G}_{f0} = 15 \text{ J/m}^2$, which led to very few random simulations exhibiting snap-back that were discarded, it seems that failure of the considered beam is still not perfectly brittle, though the contribution of distributed cracking to the peak load is significantly reduced. The latter can also be verified by the fact that the mesh dependence of the output standard deviation when using the constant distributions is much more pronounced, indicating less averaging effect. Lastly, we can observe that the present model has now shifted such that is closer to the weakest-link model than to the case of constant distributions, and has similar performance to the weakest-link model in terms of the standard deviation, but significantly improved performance in terms of the mean size effect.

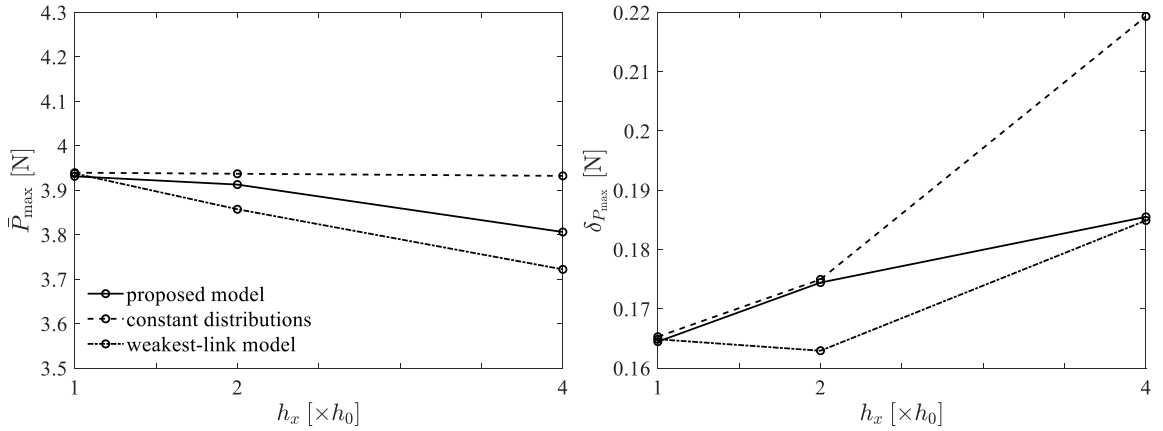


Figure 4.5: Mean (left) and standard deviation (right) of peak load of the unnotched beam under three-point bending with probabilistic models I)-III) ($\overline{G}_{f0} = 15 \text{ J/m}^2$)

4.2.3 Notched beam under three-point bending

In the preceding analysis of unnotched beams under three-point bending, we focused on two intermediate cases of failure lying between the limits of purely diffused and purely localized damage, for which the performance of the proposed model in mitigating mesh dependence of the output strength statistics has been satisfactory. Most importantly, it was shown that the model is able to switch from the fiber-bundle to the weakest-link model as the failure process transitions from predominantly diffused to more localized, which is a consequence of the imposed dependence of the sampling distribution functions of fracture properties on the numerical parameters $\delta_{\omega 1}$ and $\delta_{\omega 2}$ capturing the

actual damage pattern of an element.

In the current and following sections, we further evaluate the consistency of probabilistic and mechanical behavior in the present model, by verifying it applies the correct scaling of the probability distributions as well as of the post-peak slope of the constitutive law in the limiting cases of propagation of localized damage and of a purely diffused damage pattern. We consider a notched beam of the same size as the unnotched beam of the previous section ($7.5 \text{ mm} \times 2.5 \text{ mm}$), having relative notch depth 0.5 (Fig. 4.6). All elastic properties as well as input statistical parameters of fracture properties retain the values provided in Section 4.2.1. To investigate the mesh dependence of the output statistics of peak load of the beam, we again consider the same set of element sizes $h_x = h_0, 2h_0, 4h_0$ whereas $h_y = h_0 = \text{constant}$, and a regular mesh consisting of rectangular elements aligned with the direction of overall crack growth. It should be noted that, in order to ensure a large notch width over notch depth ratio, there is a single element just above the notch, of trapezoidal shape, with lower side representing the notch width of dimension $w = h_0/2$, and upper side of dimension equal to the current dimension h_x of the subsequent rectangular finite elements. Use of a trapezoidal element with bases w and h_x at the notch tip allows us not only to specify a sufficiently small and constant notch width w such that the resulting stress concentration is significant and the energy regularization scheme is efficient, but also to always have a single column of elements above the notch, regardless of the selected value of h_x .

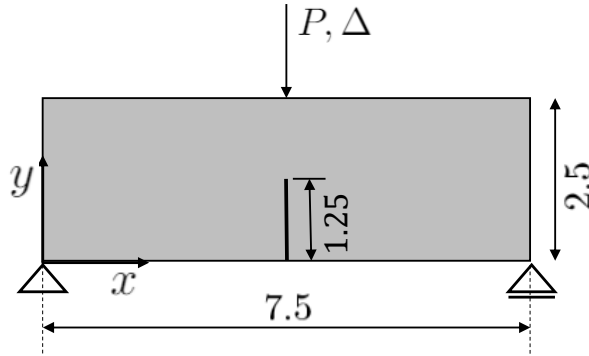


Figure 4.6: Notched beam under three-point bending considered in the simulation (all dimensions are in mm)

Stress concentration induced by the presence of the notch dictates the location of damage initiation to be confined inside the single element above the notch tip, regardless of the randomness of material properties. Consequently, the mean peak load is a deterministic quantity whereas material randomness affects only the variability of structural strength, as is known in this case of Type II

size effect [15, 59, 103]. Strain localization is already pronounced when the peak load is reached, so the energy regularization scheme will switch to the crack band model [17], and will be able to fully recover mesh objectivity of the mean peak load, as shown in the results of the proposed model in Fig. 4.7 (left), obtained with the previously calibrated optimum set of parameters for this material ($\delta_{t1} = 0$, $\delta_{t2} = 0$, $\kappa = 1$, $\lambda = 1$). Following strain localization at the element above the notch, damage propagation into a single band of elements will occur, and this will lead to the propagation parameter $\delta_{\omega 2}$ quickly reach its maximum value, so the present model will transition to the case of constant distributions. This can be verified by Fig. 4.7, where it is clear that the output statistics obtained by application of the present model and of the assumption of constant distributions almost coincide. Additionally, these two approaches are the most efficient in mitigating mesh dependence of the output statistics of peak load. Given that, at the peak load, there is always a single column of damaged elements just above the notch, consisting of approximately the same number of failed elements since the dimension h_y is kept constant between the different discretizations, the output variability of peak load should directly reflect the input randomness, and should thus be independent of the element size if the fracture properties are sampled from size-independent distributions.

Based on the above discussion, we expect that application of the weakest-link model in the considered case of the notched beam will have a poor performance in providing size-independent statistics of peak load capacity, since this model always introduces a dependence of the statistical parameters on the element size. More specifically, the weakest-link model assigns lower mean strength and coefficient of variation to larger elements, apart from the perfectly brittle case, where the imposed size-effect is still present in the mean but not in the coefficient of variation. Given that the simulated notched beam has uncracked ligament of depth comparable to Irwin's characteristic length, as calculated using the mean values of the relevant material properties, its failure is not perfectly brittle, so the peak load is controlled by both the tensile strength and fracture energy, and thus its statistics will depend on the element size h_x as a consequence of the size dependence of the sampled from the weakest-link model tensile strengths. As shown in Fig. 4.7, both the mean as well as the standard deviation of peak load eventually decrease for the largest element size used. The mesh dependence of the second statistical moment is more pronounced than the corresponding of the mean peak load, since the parameters of the energy regularization scheme, which remain the same as in the unnotched beam of the same material ($\delta_{t1} = 0.7$, $\delta_{t2} = 0.7$, $\kappa = 1$, $\lambda = 1$), were calibrated such that the mean size effect is mitigated. However, the induced delay in the transition of the energy regularization scheme to the crack band model in order to increase the mean peak load of larger elements and thus alleviate the mean size effect, is totally inconsistent with the failure mechanism

of the notched beam, which requires the scaling of the post-peak branch of the constitutive law such that the fracture energy is preserved to be applied as soon as damage initiates. Only towards large beam sizes, we expect to obtain mesh-objective strength statistics even when using the weakest-link model of tensile strength, since in that case the peak load of the structure is solely governed by the fracture energy, which will be preserved by the energy regularization scheme and will be sampled from the reference size-independent Gaussian distribution ($G_f \sim N(\bar{G}_{f0}, \omega'_0)$), due to the purely localized damage pattern ($n_b = 1$ when $g = h_0/h_1$) of a notched beam.

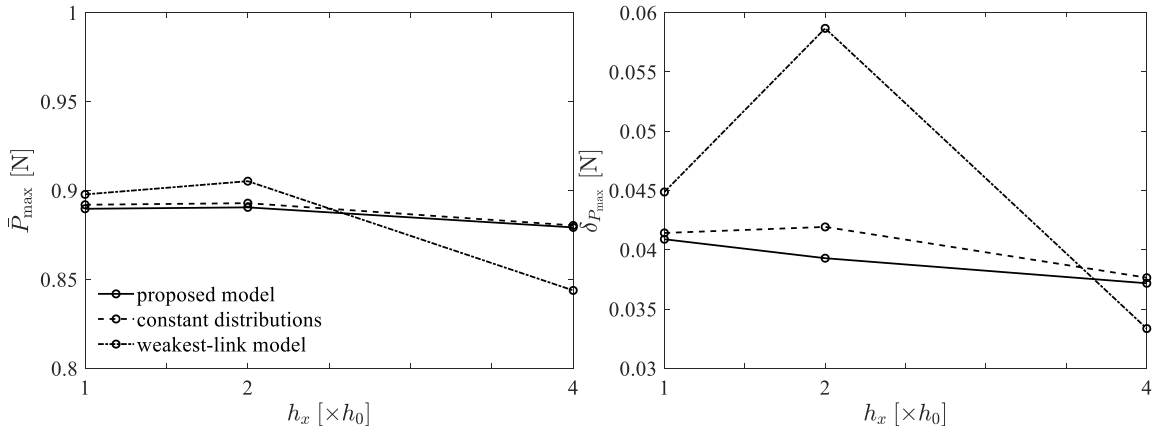


Figure 4.7: Mean (left) and standard deviation (right) of peak load of the notched beam under three-point bending with probabilistic models I)-III)

4.2.4 Unnotched beam under four-point bending

The last limiting case of failure for which we aim to evaluate the performance of the current probabilistic model is purely diffusive damage. We thus consider the four-point bending test, which can induce more diffusive cracking due to the development in the specimen of a region of constant bending moment between the concentrated loads. We simulate an unnotched beam of inner span 7.5 mm (same as the total length of the three-point bent beams), overall span of 11.25 mm, and depth 2.5 mm. A regular mesh of quadrilateral elements aligned with the expected direction of crack growth is used, similarly to the previous simulations. To investigate mesh dependence, we consider the three different element sizes $h_x = h_0, 2h_0, 4h_0$ whereas $h_y = h_0 = \text{constant}$. The input elastic and fracture properties of the beam remain the same and have been provided in Section 4.2.1. The experimental set-up is mimicked in the finite element model by applying increasing levels of vertical displacement at the midpoint of the top part of the beam, and imposing the sum of the corresponding displace-

ments of the end points of the inner span to equal the applied midpoint displacement (Fig. 4.8). To avoid damage initiation at the loaded regions, the entire upper layer of the beam as well as its cross sections above the supports have been discretized with elements of extremely high tensile strength such that they always remain elastic. Such elastic layers have been used in all simulations presented in the current study.

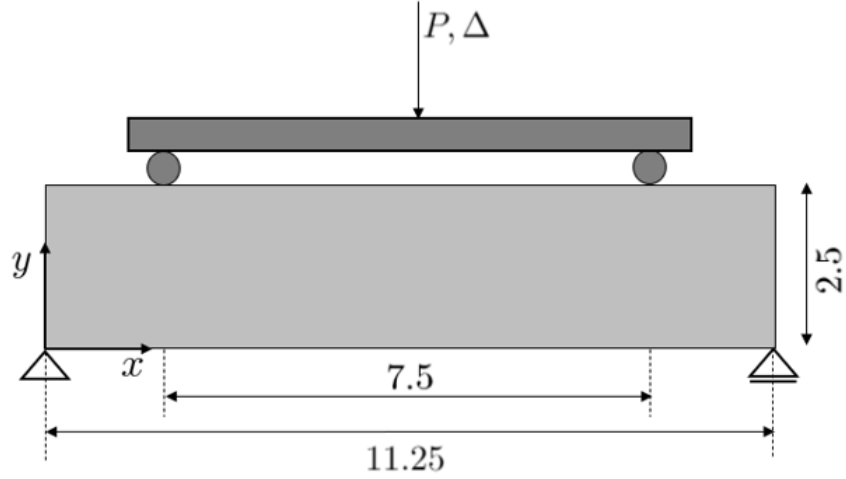


Figure 4.8: Unnotched beam under four-point bending considered in the simulation (all dimensions are in mm)

The probabilistic structural response of the beam is captured by calculating the mean and standard deviation of peak load, where 400 random simulations were required to achieve convergence of the second statistical moment. The sampling of the fracture properties was performed by approaches I)-III), with optimum values of parameters as provided in the results of the three-point bending test for the same material, i.e. $\delta_{t1} = 0$, $\delta_{t2} = 0$, $\kappa = 1$, $\lambda = 1$ for the proposed model and the case of constant distributions, and $\delta_{t1} = 0.7$, $\delta_{t2} = 0.7$, $\kappa = 1$, $\lambda = 1$ for the weakest-link model.

Fig. 4.9 provides the simulated first and second statistical moments of peak load of the beam with respect to the element size h_x , for all three probabilistic failure models. As in all previous tests, we observe that all models are able to effectively mitigate the mean size effect, since their parameters have been calibrated such that the mean behavior is optimized. Regarding the mesh dependence of the second statistical moment, it can be seen that the present model is able to provide an almost mesh-insensitive result. Due to the purely diffused damage pattern of the four-point bend beam, the simplification of a plastic fiber-bundle model of the damage zone introduced in the present

model is indeed realistic, which explains why it exhibits the highest performance for this test. The assumption of constant distributions is also acceptable, since the error in the standard deviation is approximately 7%. On account of the larger size of the damage zone in the four-point bending test, the averaging effect is significantly more pronounced than in the three-point bending, and is able to decrease the standard deviation for coarser discretizations as well, to the extent that even the simplest case of size-independent distributions can lead to output strength statistics that are only mildly dependent on the element size. In fact, due to the significant damage zone size, the performance of all three probabilistic models in the four-point bending test is improved compared to the three-point bending test of the unnotched beam of the same material. However, the weakest-link model still leads to an unacceptably high error of the standard deviation, which is shown in Fig. 4.9 to strongly increase with the element size.

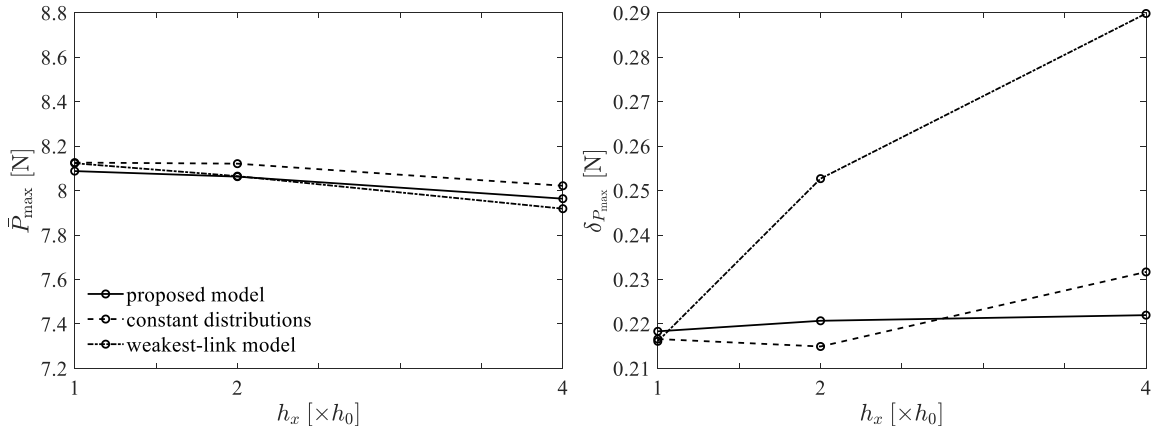


Figure 4.9: Mean (left) and standard deviation (right) of peak load of the unnotched beam under four-point bending with probabilistic models I-III)

4.3 Conclusions

The present study introduces a general probabilistic model of apparent fracture properties, which is informed by both the inherent material randomness as well as the failure mechanism of a structure. The mathematical formulation of the model (Section 4.1.1) ensures it can recover the well-established weakest-link and fiber-bundle models in the limiting cases of failure with damage localization and failure with distributed cracking respectively. Only the spatial variability of tensile strength and fracture energy is considered, as parameters on which the failure behavior of quasibrittle structures strongly depends. The formulated probability distributions of element strength and fracture en-

ergy are used as the sampling distribution functions of constitutive parameters in stochastic FE simulations of quasibrittle specimens of different geometries, under different loading configurations. The model does not require any a priori knowledge of the structural failure mechanism, since the distribution functions are made dependent on numerical parameters that can describe the evolving damage pattern in the structure, and lead to a transition of the probabilistic model towards the failure model most suitable with the actual damage mechanism.

The considered numerical examples of notched and unnotched beams under the three-point bending test, as well as of an unnotched beam subjected to four-point bending, are selected such that a wide range of structural failure mechanisms is triggered and therefore the generality of the model can be tested. It is shown that in all aforementioned tests resulting in damage patterns transitioning from purely localized to purely diffused through intermediate complex states, the model is able to switch to the failure model that is consistent with the damage mechanism experienced by the structure. An important feature of the probabilistic model is that is coupled with our recently developed mechanism-based energy regularization scheme [68], which was shown to be an efficient way of mitigating mesh dependence of the mechanical structural response in deterministic FE simulations of strain-softening continua, experiencing different damage mechanisms. In the present context of stochastic FE simulations, the size effects on the statistics of fracture properties that can arise during the evolving between loading steps, damage pattern of an element, are explicitly modeled by accordingly adjusting the input sampling distributions, and such adjustment plays an important role in mitigating mesh dependence of the output probabilistic structural response. Indeed, comparison of the present probabilistic model with other, predetermined distribution functions of constitutive parameters, shows that its performance in mitigating mesh dependence of the output statistics of structural strength is significantly higher than the performance of the prescribed probability distributions, which can be efficient only if the failure mechanism based on which they were derived happens to be the actual failure mechanism of the structure. Other benefits of the present model include its computational efficiency which makes it an attractive option for stochastic FE simulation of large-scale structures, where most probably the selected element sizes will be larger than the autocorrelation length of material properties, as well as simplicity, since the same spatial discretization used for the mechanical problem is also used for modeling of the randomness of fracture properties.

Chapter 5

Conclusions

This research introduces a general framework to address the issue of spurious mesh sensitivity of finite element (FE) simulations of strain-softening continua, for both deterministic and stochastic analyses. In the deterministic setting, mesh sensitivity is successfully mitigated by a mechanism-based energy regularization of the constitutive law, which is governed by the actual damage mechanism in a structure and ensures consistent energy dissipation in failure regardless of the mesh discretization. In the stochastic setting, the structural failure mechanism is additionally considered in the formulation of the sampling probability distributions of apparent fracture properties. The randomness of element tensile strength and fracture energy is described by a probabilistic model, that can be informed by the inherent variability of material properties, but more importantly, is adjusted based on the actual failure pattern of an element and can transition between the weakest-link and fiber-bundle models for the cases of purely localized and purely diffused damage respectively. It should be emphasized that the behavior of each finite element is considered to represent the behavior of a material element of finite size, so the input constitutive and probabilistic models for the finite elements represent both material as well as structural behavior of the corresponding material elements. The latter is manifested through the failure mechanism, which is quantified by numerical parameters describing the nonlocal damage pattern around each element. These parameters are used in both the energy regularization scheme as well as the probability distributions of fracture properties. The introduction of these descriptors allows us to capture the evolving during the simulation damage pattern, which obviates the need for any a priori knowledge of the structural failure mechanism. Therefore, the proposed method can be applied to quasibrittle structures under general loading scenarios.

The following conclusions can be drawn based on this study:

1. Energy regularization of the constitutive law constitutes an important tool for mitigating the spurious mesh sensitivity of FE simulations of strain-softening continua, owing to its generality since it is connected with the energetic approach to fracture. The developed mechanism-based energy regularization scheme overcomes the limitations of the most prevalent energy regularization method, i.e. the crack band model. The present model is able to mitigate mesh dependence under various failure mechanisms, and recover the crack band model in cases of a purely localized damage pattern. Additionally, the crack band model is tied with the assumption that the fracture energy is the most important parameter governing the failure behavior and which should thus be preserved. For complicated constitutive laws, selection of the relevant parameters to preserve can be challenging. Such decision is not required though with the present model, since it adjusts the point-wise tangential stiffness tensor based on the current state of damage pattern.
2. Under dynamic loading conditions, energy regularization can be made possible by controlling the damage growth rate based on the actual failure mechanism. More specifically, if the applied strain rate and structure geometry are such that a purely diffused damage pattern is observed, then material point behavior and structural behavior coincide so the damage should propagate at the same rate regardless of the element size. However, in cases of a localized damage pattern (e.g. notched specimen under high strain-rate loading), the resulting more brittle failure behavior of larger elements implies that damage should propagate faster inside them, so the damage growth rate should depend on the element size.
3. Stochastic discrete element model simulations of unnotched quasibrittle specimens subjected to a wide range of tensile strain rates show the transition of the damage pattern from fairly localized to purely diffused with the rate. This result has important implications for the scaling of the distribution of structural strength. It is shown that, for low to intermediate strain rates, the mean and standard deviation of specimen strength decrease with an increasing specimen size. At high strain rates, the size effect on the mean diminishes whereas the decreasing trend of standard deviation becomes stronger and it exhibits a power-law scaling behavior, as would be predicted by a fiber-bundle model statistical representation of failure. The results also indicate that, for a given specimen size, an increasing strain rate leads to a reduction in the standard deviation of nominal strength due to the more diffusive cracking pattern. The simulated rate and size effects on the strength statistics have been captured by a rate-dependent weakest-link model, which transitions from a weakest-link to a fiber-bundle model representation of

structural failure as high strain rates lead to a more diffusive damage pattern. This part of the research has provided insight into the formulation of a general probabilistic model of apparent fracture properties, that is governed by the actual failure mechanism of a structure.

4. The present research proposes a new method to mitigate the mesh dependence of probabilistic structural response in stochastic FE simulations of softening continua. Instead of making an a priori assumption for the structural failure mechanism and sampling the input tensile strength from a prescribed probability distribution, a common practice in the literature, it is suggested to adjust the sampling distributions of constitutive properties according to the evolving damage pattern in the structure. The proposed model is formulated in a general form so that it can recover the well-established probabilistic models suitable for some limiting failure cases, such as the weakest-link and fiber-bundle models. The model also considers the effect of the failure mechanism on the distribution of fracture energy, and is coupled with the mechanism-based energy regularization scheme, introduced in the deterministic analysis. Stochastic FE simulations of quasibrittle structures of different geometries subjected to different loading configurations, show that the present model can efficiently mitigate the mesh dependence of the output first and second statistical moments of structural strength.

Bibliography

- [1] V. Agrawal and K. Dayal. Dependence of equilibrium Griffith surface energy on crack speed in phase-field models for fracture coupled to elastodynamics. *Int. J. Fract.*, 207(2):243–249, 2017.
- [2] R. Alessi, M. Ambati, T. Gerasimov, S. Vidoli, and L. De Lorenzis. Comparison of Phase-Field Models of Fracture Coupled with Plasticity. In *Advances in Computational Plasticity*, volume 46 of *Computational Methods in Applied Sciences*, pages 1–21. Springer International Publishing, Cham, 2017.
- [3] M. Ambati, T. Gerasimov, and L. De Lorenzis. Phase-field modeling of ductile fracture. *Comput. Mech.*, 55(5):1017–1040, 2015.
- [4] S. Esna Ashari, G. Buscarnera, and G. Cusatis. A lattice discrete particle model for pressure-dependent inelasticity in granular rocks. *Int. J. Rock Mech. Min. Sci.*, 91:49–58, 2017.
- [5] K. Bagi. Microstructural Stress Tensor of Granular Assemblies With Volume Forces. *ASME J. Appl. Mech.*, 66(4):934–936, 1999.
- [6] G. I. Barenblatt. The Mathematical Theory of Equilibrium Cracks in Brittle Fracture. volume 7 of *Adv. Appl. Mech.*, pages 55 – 129. Elsevier, 1962.
- [7] K.-J. Bathe. *Finite Element Procedures*. Prentice Hall, Englewood Cliffs, N.J., 1996.
- [8] Z. P. Bažant. *Scaling of Structural Strength*. Elsevier, London, 2005.
- [9] Z. P. Bažant and F. C. Caner. Comminution of solids caused by kinetic energy of high shear strain, with implications for impact, shock and shale fracturing. *Proc. Natl. Acad. Sci. U.S.A.*, 110(48):19291–19294, 2013.
- [10] Z. P. Bažant and F. C. Caner. Impact comminution of solids due to local kinetic energy of high shear strain rate: I. Continuum theory and turbulence analogy. *J. Mech. Phys. Solids*, 64:223–235, 2014.
- [11] Z. P. Bažant and L. Cedolin. Blunt crack band propagation in finite element analysis. *J. Eng. Mech. Div. ASCE*, 105(2):297–315, 1979.
- [12] Z. P. Bažant and L. Cedolin. *Stability of Structures: Elastic, Inelastic, Fracture and Damage Theories*. Oxford University Press, New York, 1991.
- [13] Z. P. Bažant and R. Gettu. Rate Effects and Load Relaxation in Static Fracture of Concrete. *ACI Mater. J.*, 89(5):456–468, 1992.

- [14] Z. P. Bažant and J.-L. Le. Nano-mechanics based modeling of lifetime distribution of quasibrittle structures. *Eng. Fail. Anal.*, 16:2521–2529, 2009.
- [15] Z. P. Bažant and J.-L. Le. *Probabilistic Mechanics of Quasibrittle Structures: Strength, Lifetime, and Size Effect*. Cambridge University Press, Cambridge, U.K., 2017.
- [16] Z. P. Bažant, J.-L. Le, and C. G. Hoover. Nonlocal boundary layer model: overcoming boundary condition problems in strength statistics and fracture analysis of quasibrittle materials. In *The 7th International Conference on Fracture Mechanics of Concrete and Concrete Structures (FraMCoS-7)*, pages 135–143, Jeju, Korea, 2010.
- [17] Z. P. Bažant and B. H. Oh. Crack band theory for fracture of concrete. *Mater. Struct.*, 16:155–177, 1983.
- [18] Z. P. Bažant and S. D. Pang. Activation energy based extreme value statistics and size effect in brittle and quasibrittle fracture. *J. Mech. Phys. Solids*, 55:91–131, 2007.
- [19] Z. P. Bažant and J. Planas. *Fracture and Size Effect in Concrete and Other Quasibrittle Materials*. CRC Press, London, 1998.
- [20] Z. P. Bažant. Softening Instability: Part I—Localization Into a Planar Band. In *J. Appl. Mech.*, volume 55, pages 517–522, New York, NY, 1988. ASME.
- [21] Z. P. Bažant. Softening Instability: Part II—Localization Into Ellipsoidal Regions. In *J. Appl. Mech.*, volume 55, pages 523–529, New York, NY, 1988. ASME.
- [22] Z. P. Bažant. Stable States and Paths of Structures with Plasticity or Damage. *J. Eng. Mech.*, 114(12):2013–2034, 1988.
- [23] Z. P. Bažant. Design of quasibrittle materials and structures to optimize strength and scaling at probability tail: an apercu. *Proc. R. Soc. A*, 475(2224):20180617, 2019.
- [24] Z. P. Bažant, T. B. Belytschko, and T.-P. Chang. Continuum Theory for Strain-Softening. *ASCE J. Eng. Mech.*, 110(12):1666–1692, 1984.
- [25] Z. P. Bažant and M. Jirásek. Nonlocal Integral Formulations of Plasticity and Damage: Survey of Progress. *ASCE J. Eng. Mech.*, 128(11):1119–1149, 2002.
- [26] Z. P. Bažant and S. D. Pang. Mechanics-based statistics of failure risk of quasibrittle structures and size effect on safety factors. *Proc. Natl. Acad. Sci. U.S.A.*, 103(25):9434–9439, 2006.
- [27] Z. P. Bažant and G. Pijaudier-Cabot. Measurement of Characteristic Length of Nonlocal Continuum. *ASCE J. Eng. Mech.*, 115(4):755–767, 1989.
- [28] Z. P. Bažant, M. R. Tabbara, M. T. Kazemi, and G. Pijaudier-Cabot. Random Particle Model for Fracture of Aggregate or Fiber Composites. *ASCE J. Eng. Mech.*, 116(8):1686–1705, 1990.
- [29] Z. P. Bažant and Q. Yu. Size-Effect Testing of Cohesive Fracture Parameters and Nonuniqueness of Work-of-Fracture Method. *ASCE J. Eng. Mech.*, 137(8):580–588, 2011.
- [30] T. Belytschko, H. Chen, J. Xu, and G. Zi. Dynamic crack propagation based on loss of hyperbolicity and a new discontinuous enrichment. *Int. J. Numer. Methods Eng.*, 58(12):1873–1905, 2003.
- [31] E. Berthier, V. Démery, and L. Ponson. Damage spreading in quasi-brittle disordered solids: I. Localization and failure. *J. Mech. Phys. Solids*, 102:101–124, 2017.

- [32] H. S. Bhat, A. J. Rosakis, and C. G. Sammis. A micromechanics based constitutive model for brittle failure at high strain rates. *ASME J. Appl. Mech.*, 79:031016, 2012.
- [33] J. Bleyer and J.-F. Molinari. Microbranching instability in phase-field modelling of dynamic brittle fracture. *Appl. Phys. Lett.*, 110(15):151903, 2017.
- [34] J. Bleyer, C. Roux-Langlois, and J.-F. Molinari. Dynamic crack propagation with a variational phase-field model: limiting speed, crack branching and velocity-toughening mechanisms. *Int. J. Fract.*, 204(1):79–100, 2017.
- [35] W. R. Blumenthal. High Strain Rate Compression Testing of Ceramics and Ceramic Composites. In J. J. Swab, editor, *Advances in Ceramic Armor Ceramic Engineering and Science Proceedings*, volume 26, pages 89–96, 2005.
- [36] J. E. Bolander, G. S. Hong, and K. Yoshitake. Structural Concrete Analysis Using Rigid-Body-Spring Networks. *J. Comput. Aided Civil Infrastruct. Eng.*, 15(2):120–133, 2000.
- [37] J. E. Bolander and S. Saito. Fracture analyses using spring networks with random geometry. *Eng. Fract. Mech.*, 61(5):569–591, 1998.
- [38] G. Borino, B. Failla, and F. Parrinello. A symmetric nonlocal damage theory. *Int. J. Solids Struct.*, 40(13):3621 – 3645, 2003.
- [39] B. Bourdin, G. A. Francfort, and J.-J. Marigo. Numerical experiments in revisited brittle fracture. *J. Mech. Phys. Solids*, 48(4):797–826, 2000.
- [40] B. Bourdin, G. A. Francfort, and J.-J. Marigo. *The Variational Approach to Fracture*. Springer Dordrecht, Netherlands, 2008.
- [41] B. Bourdin, G. A. Francfort, and J.-J. Marigo. The Variational Approach to Fracture. *J. Elasticity*, 91(1-3):5–148, 2008.
- [42] A. Braides. *Approximation of Free-Discontinuity Problems*. Lecture Notes in Mathematics. Springer-Verlag, Berlin and New York, 1998.
- [43] N. Chandra, H. Li, C. Shet, and H. Ghonem. Some issues in the application of cohesive zone models for metal–ceramic interfaces. *Int. J. Solids Struct.*, 39(10):2827 – 2855, 2002.
- [44] C.-H. Chen, E. Bouchbinder, and A. Karma. Instability in dynamic fracture and the failure of the classical theory of cracks. *Nat. Phys.*, 13(12):1186–1190, 2017.
- [45] P. A. Cundall. A Computer Model for Simulating Progressive Large Scale Movements in Blocky Rock Systems. In *Proc. Int. Symp. Rock Fracture*, volume 1, pages II–8, Nancy, France, 1971.
- [46] P. A Cundall and O. D. L. Strack. A discrete numerical model for granular assemblies. *Géotechnique*, 29(1):47–65, 1979.
- [47] G. Cusatis, Z. P. Bažant, and L. Cedolin. Confinement-Shear Lattice Model for Concrete Damage in Tension and Compression: I. Theory. *ASCE J. Eng. Mech.*, 129(12):1439–1448, 2003.
- [48] G. Cusatis, Z. P. Bažant, and L. Cedolin. Confinement-Shear Lattice Model for Concrete Damage in Tension and Compression: II. Computation and Validation. *ASCE J. Eng. Mech.*, 129(12):1449–1458, 2003.

- [49] G. Cusatis and L. Cedolin. Two-scale study of concrete fracturing behavior. *Eng. Fract. Mech.*, 74(1–2):3–17, 2007. Fracture of Concrete Materials and Structures.
- [50] G. Cusatis, A. Mencarelli, D. Pelessone, and J. Baylot. Lattice Discrete Particle Model (LDPM) for failure behavior of concrete. II: Calibration and validation. *Cem. Concr. Compos.*, 33(9):891–905, 2011.
- [51] G. Cusatis, D. Pelessone, and A. Mencarelli. Lattice Discrete Particle Model (LDPM) for failure behavior of concrete. I: Theory. *Cem. Concr. Compos.*, 22:881–890, 2011.
- [52] G. Cusatis and E. A. Schaufert. Cohesive crack analysis of size effect. *Eng. Fract. Mech.*, 76(14):2163 – 2173, 2009.
- [53] H. E. Daniels. The statistical theory of the strength of bundles of threads. I. *Proc. R. Soc. Lond. A*, 183(995):405–435, 1945.
- [54] N. P. Daphalapurkar, K.T. Ramesh, L. Graham-Brady, and J.-F. Molinari. Predicting variability in the dynamic failure strength of brittle materials considering pre-existing flaws. *J. Mech. Phys. Solids*, 59:297–319, 2011.
- [55] R. Desmorat, M. Chambart, F. Gatuingt, and D. Guilbaud. Delay-active damage versus non-local enhancement for anisotropic damage dynamics computations with alternated loading. *Eng. Fract. Mech.*, 77(12):2294 – 2315, 2010.
- [56] F. P. Duda, A. Ciarbonetti, P. J. Sánchez, and A. E. Huespe. A phase-field/gradient damage model for brittle fracture in elastic–plastic solids. *Int. J. Plast.*, 65:269–296, 2015.
- [57] D. S. Dugdale. Yielding of steel sheets containing slits. *J. Mech. Phys. Solids*, 8(2):100 – 104, 1960.
- [58] J. Eliáš. Adaptive technique for discrete models of fracture. *Int. J. Solids Struct.*, 100-101:376–387, 2016.
- [59] J. Eliáš, M. Vořechovský, J. Skoček, and Z. P. Bažant. Stochastic discrete meso-scale simulations of concrete fracture: Comparison to experimental data. *Eng. Fract. Mech.*, 135(1):1–16, 2015.
- [60] B. Erzar and P. Forquin. An Experimental Method to Determine the Tensile Strength of Concrete at High Rates of Strain. *Exp. Mech.*, 50(7):941–955, 2010.
- [61] S. Feng and P. N. Sen. Percolation on elastic networks: new exponent and threshold. *Phys. Rev. Lett.*, 52(3):216–219, 1984.
- [62] P. Forquin and B. Lukić. On the Processing of Spalling Experiments. Part I: Identification of the Dynamic Tensile Strength of Concrete. *J. Dyn. Behav. Mater.*, 4:34–55, 2018.
- [63] G. A. Francfort and J.-J. Marigo. Revisiting brittle fracture as an energy minimization problem. *J. Mech. Phys. Solids*, 46(8):1319–1342, 1998.
- [64] F. Gatuingt, L. Snozzi, and J. F. Molinari. Numerical determination of the tensile response and the dissipated fracture energy of concrete: role of the mesostructure and influence of the loading rate. *Int. J. Numer. Anal. Methods Geomech.*, 37:3112–3130, 2013.
- [65] R. G. Ghanem and P. D. Spanos. *Stochastic Finite Elements : A Spectral Approach*. Springer-Verlag, New York, 1991.

- [66] A. Giacomini. Size Effects on Quasi-Static Growth of Cracks. *SIAM J. Math. Anal.*, 36(6):1887–1928, 2005.
- [67] C. Giry, F. Dufour, and J. Mazars. Stress-based nonlocal damage model. *Int. J. Solids Struct.*, 48(25-26):3431–3443, 2011.
- [68] A. Gorgogianni, J. Eliáš, and J.-L. Le. Mechanism-Based Energy Regularization in Computational Modeling of Quasibrittle Fracture. *ASME J. Appl. Mech.*, 87(9), 2020.
- [69] P. Grassl and Z. P. Bažant. Random Lattice-Particle Simulation of Statistical Size Effect in Quasi-Brittle Structures Failing at Crack Initiation. *ASCE J. Eng. Mech.*, 135(2):85–92, 2009.
- [70] A. A. Griffith and G. I. Taylor. VI. The Phenomena of Rupture and Flow in Solids. *Trans. R. Soc. Lond. A*, 221(582-593):163–198, 1921.
- [71] M. Grigoriu. Simulation of Stationary Non-Gaussian Translation Processes. *J. Eng. Mech.*, 124(2):121–126, 1998.
- [72] D.L. Grote, S.W. Park, and M. Zhou. Dynamic behavior of concrete at high strain rates and pressures: I. experimental characterization. *Int. J. Impact Eng.*, 25:869–886, 2001.
- [73] H. J. Herrmann, A. Hansen, and S. Roux. Fracture of disordered, elastic lattices in two dimensions. *Phys. Rev. B*, 39(1):637–648, 1989.
- [74] A. Hillerborg, M. Modéer, and P.-E. Petersson. Analysis of crack formation and crack growth in concrete by means of fracture mechanics and finite elements. *Cem. Concr. Res.*, 6(6):773 – 781, 1976.
- [75] A. Hrennikoff. Solution of problems of elasticity by the framework method. *J. Appl. Mech.*, 8(4):169–175, 1941.
- [76] Y. K. Hwang, J. Bolander, and Y. M. Lim. Simulation of concrete tensile failure under high loading rates using three-dimensional irregular lattice models. *Mech. Mater.*, 101:136–146, 2016.
- [77] K. Iwashita and M. Oda. *Mechanics of Granular Materials: An Introduction*. CRC press, Boca Raton, FL, 1999.
- [78] M. Jirásek. Nonlocal Theories in Continuum Mechanics. *Acta Polytech.*, 44(5-6):16–34, 2004.
- [79] M. Jirásek and M. Bauer. Numerical aspects of the crack band approach. *Comp. Struct.*, 110-111:60–78, 2012.
- [80] M. Jirásek and Z. P. Bažant. Macroscopic fracture characteristics of random particle systems. *Int. J. Fract.*, 69(3):201–228, 1994.
- [81] M. Jirásek and Z. P. Bažant. Particle Model for Quasibrittle Fracture and Application to Sea Ice. *ASCE J. Eng. Mech.*, 121(9):1016–1025, 1995.
- [82] M. Jirásek. Mathematical analysis of strain localization. *REGC*, 11(7-8):977–991, 2007.
- [83] L. Kachanov. *Introduction to Continuum Damage Mechanics*. Springer, Netherlands, 1986.
- [84] A. Kara, A. Tasdemirci, and M. Guden. Modeling quasi-static and high strain rate deformation and failure behavior of a (± 45) symmetric E-glass/polyester composite under compressive loading. *Mater. Des.*, 49:566–574, 2013.

- [85] T. Kawai. New discrete models and their application to seismic response analysis of structures. *Nucl. Eng. Des.*, 48(1):207–229, 1978. Special Issue Structural Mechanics in Reactor Technology - Smirt-4.
- [86] O. Keita, C. Dascalu, and B. François. A two-scale model for dynamic damage evolution. *J. Mech. Phys. Solids*, 64:170–183, 2014.
- [87] J. Kimberley, K. T. Ramesh, and N. P. Daphalapurkar. A scaling law for the dynamic strength of brittle solids. *Acta Mater.*, 61:3509–3521, 2013.
- [88] R. H. Kraft, J. F. Molinari, K. T. Ramesh, and D. H. Warner. Computational micromechanics of dynamic compressive loading of a brittle polycrystalline material using a distribution of grain boundary properties. *J. Mech. Phys. Solids*, 56:2618–2641, 2008.
- [89] F. Kun, S. Zapperi, and H.J. Herrmann. Damage in fiber bundle models. *Eur. Phys. J. B*, 17(2):269–279, 2000.
- [90] J.-L. Le, Z. P. Bažant, and M. Z. Bazant. Unified nano-mechanics based probabilistic theory of quasibrittle and brittle structures: I. strength, crack growth, lifetime and scaling. *J. Mech. Phys. Solids*, 59:1291–1321, 2011.
- [91] J.-L. Le, J. Eliáš, A. Gorgogianni, J. Vievering, and J. Kveton. Rate-Dependent Scaling of Dynamic Tensile Strength of Quasibrittle Structures. *ASME J. Appl. Mech.*, 85(2):021003, 2018.
- [92] J.-L. Le and J. Eliáš. A probabilistic crack band model for quasibrittle fracture. *ASME J. Appl. Mech.*, 83(5):051005, 2016.
- [93] J.-L. Le, Z. Xu, and J. Eliáš. Internal Length Scale of Weakest-Link Statistical Model for Quasi-Brittle Fracture. *ASCE J. Eng. Mech.*, 144(4), 2017.
- [94] M. Lemaitre and J. L. Chaboche. Aspect Phenomenologique de la Rupture par Endommagement. *J. Mec. Appl.*, 2:317–365, 1978.
- [95] C.-C. Li and A. Der Kiureghian. Optimal Discretization of Random Fields. *ASCE J. Eng. Mech.*, 119(6):1136–1154, 1993.
- [96] Z. Li and J. Lambros. Determination of the dynamic response of brittle composites by the use of the split Hopkinson pressure bar. *Compos. Sci. Technol.*, 59:1097–1107, 1999.
- [97] E. Lorentz and V. Godard. Gradient damage models: towards full-scale computations. *Comput. Methods Appl. Mech. Eng.*, 200:1927–1944, 2011.
- [98] Y. B. Lu and Q. M. Li. About the dynamic uniaxial tensile strength of concrete-like materials. *Int. J. Impact Eng.*, 38(4):171–180, 2011.
- [99] W. Luo and Z. P. Bažant. Fishnet statistics for probabilistic strength and scaling of nacreous imbricated lamellar materials. *J. Mech. Phys. Solids*, 109:264–287, 2017.
- [100] W. Luo and Z. P. Bažant. Fishnet model with order statistics for tail probability of failure of nacreous biomimetic materials with softening interlaminar links. *J. Mech. Phys. Solids*, 121:281–295, 2018.
- [101] W. Luo and Z. P. Bažant. Fishnet Statistical Size Effect on Strength of Materials With Nacreous Microstructure. *ASME J. Appl. Mech.*, 86(8), 2019.

- [102] W. Luo and Z. P. Bažant. General Fishnet Statistics of Strength: Nacreous, Biomimetic, Concrete, Octet-Truss, and Other Architected or Quasibrittle Materials. *ASME J. Appl. Mech.*, 87(3):1–14, 2019.
- [103] W. Luo, J.-L. Le, M. Rasoolinejad, and Z. P. Bažant. Coefficient of Variation of Shear Strength of RC Beams and Size Effect. *J. Eng. Mech.*, 147(2), 2021.
- [104] S. May, J. Vignollet, and R. de Borst. A numerical assessment of phase-field models for brittle and cohesive fracture: Γ -Convergence and stress oscillations. *Eur. J. Mech. A Solids*, 52:72–84, 2015.
- [105] J. Mazars. *Application de la mécanique de l'endommagement au comportement non linéaire et à la rupture du béton de structure*. PhD thesis, University of Paris VI, Paris, France, 1984.
- [106] C. Miehe, M. Hofacker, L.-M. Schänzel, and F. Aldakheel. Phase field modeling of fracture in multi-physics problems. Part II. Coupled brittle-to-ductile failure criteria and crack propagation in thermo-elastic-plastic solids. *Comput. Methods Appl. Mech. Eng.*, 294:486–522, 2015.
- [107] C. Miehe, F. Welschinger, and M. Hofacker. Thermodynamically consistent phase-field models of fracture: Variational principles and multi-field FE implementations. *Int. J. Numer. Methods Eng.*, 83(10):1273–1311, 2010.
- [108] S. Murakami. Notion of Continuum Damage Mechanics and its Application to Anisotropic Creep Damage Theory. *J. Eng. Mater. Technol.*, 105(2):99–105, 04 1983.
- [109] N. M. Newmark. *A Method of Computation for Structural Dynamics*. University of Illinois, Urbana, 1959.
- [110] T. T. Nguyen, J. Yvonnet, M. Bornert, C. Chateau, K. Sab, R. Romani, and R. Le Roy. On the choice of parameters in the phase field method for simulating crack initiation with experimental validation. *Int. J. Fract.*, 197(2):213–226, 2016.
- [111] T.T. Nguyen, J. Yvonnet, Q.-Z. Zhu, M. Bornert, and C. Chateau. A phase-field method for computational modeling of interfacial damage interacting with crack propagation in realistic microstructures obtained by microtomography. *Comput. Methods Appl. Mech. Eng.*, 312:567–595, 2016.
- [112] J. Ožbolt, J. Bošnjak, and E. Sola. Dynamic fracture of concrete compact tension specimen: Experimental and numerical study. *Int. J. Solids Struct.*, 50(25-26):4270–4278, 2013.
- [113] J. Ožbolt, A. Sharma, and H.-W. Reinhardt. Dynamic fracture of concrete – compact tension specimen. *Int. J. Solids Struct.*, 48(10):1534–1543, 2011.
- [114] Z. Pan, R. Ma, D. Wang, and A. Chen. A review of lattice type model in fracture mechanics: theory, applications, and perspectives. *Eng. Fract. Mech.*, 190:382–409, 2018.
- [115] B. Patzák. OOFEM - An Object-Oriented Simulation Tool for Advanced Modeling of Materials and Structures. *Acta Polytech.*, 52(6):59–66, 2012.
- [116] L. F. Pereira, J. Weerheijm, and L. J. Sluys. A new effective rate dependent damage model for dynamic tensile failure of concrete. *Eng. Fract. Mech.*, 176:281–299, 2017.
- [117] S. L. Phoenix. Stochastic strength and fatigue of fiber bundles. *Int. J. Fract.*, 14(3):327–344, 1978.

- [118] G. Pijaudier-Cabot and J. Ludovic. Continuum damage modelling and some computational issues. *Revue Française de Génie Civil*, 6(6):991 – 1017, 2002.
- [119] Y. N. Rabotnov. Creep rupture. In M. Hetényi and W. G. Vincenti, editors, *Applied Mechanics*, pages 342–349, Berlin, Heidelberg, 1968. International Union of Theoretical and Applied Mechanics, Springer.
- [120] R. Rezakhani and G. Cusatis. Asymptotic expansion homogenization of discrete fine-scale models with rotational degrees of freedom for the simulation of quasi-brittle materials. *J. Mech. Phys. Solids*, 88:320–345, 2016.
- [121] A. J. Rosakis. Explosion at the Parthenon: Can We Pick Up the Pieces? Technical Report GALEIT SM Report 99-3, California Institute of Technology, 1999.
- [122] L. Rothenburg and R. J. Bathurst. Analytical study of induced anisotropy in idealized granular materials. *Géotechnique*, 39(4):601–614, 1989.
- [123] S. Roux and E. Guyon. Mechanical percolation : a small beam lattice study. *J. Physique Lett.*, 46(21):999–1004, 1985.
- [124] J. W. Rudnicki and J. R. Rice. Conditions for the localization of deformation in pressure-sensitive dilatant materials. *J. Mech. Phys. Solids*, 23:371–394, 1975.
- [125] M. Sahimi and J. D. Goddard. Elastic percolation models for cohesive mechanical failure in heterogeneous systems. *Phys. Rev. B*, 33(11):7848–7851, 1986.
- [126] M. Salviato and Z. P. Bažant. The asymptotic stochastic strength of bundles of elements exhibiting general stress-strain laws. *Probabilistic Eng. Mech.*, 36:1–7, 2014.
- [127] E. Schlangen and J.G.M van Mier. Experimental and numerical analysis of micromechanisms of fracture of cement-based composites. *Cem. Concr. Compos.*, 14(2):105–118, 1992.
- [128] H. Schuler, C. Mayrhofer, and K. Thoma. Spall experiments for the measurement of the tensile strength and fracture energy of concrete at high strain rates. *Int. J. Impact Eng.*, 32:1635–1650, 2006.
- [129] M. Shinozuka and G. Deodatis. Simulation of Multi-Dimensional Gaussian Stochastic Fields by Spectral Representation. *Appl. Mech. Rev.*, 49(1):29–53, 1996.
- [130] F. Tonon. Explicit Exact Formulas for the 3-D Tetrahedron Inertia Tensor in Terms of its Vertex Coordinates. *J. Math. Stat.*, 1(1):8–11, 2005.
- [131] C. V. Verhoosel and R. de Borst. A phase-field model for cohesive fracture. *Int. J. Numer. Methods Eng.*, 96(1):43–62, 2013.
- [132] J. Vignollet, S. May, R. de Borst, and C. V. Verhoosel. Phase-field models for brittle and cohesive fracture. *Mecc.*, 49(11):2587–2601, 2014.
- [133] J. Weerheijm, I. Vegt, and K. van Breugel. Research developments and experimental data on dynamic concrete behaviour. In *Conference on Advances in Construction Materials*, pages 765–773, Stuttgart, Germany, 2007.
- [134] W. Weibull. A Statistical Distribution Function of Wide Applicability. *ASME J. Appl. Mech.*, 153(18):293–297, 1951.

- [135] J.-Y. Wu. A unified phase-field theory for the mechanics of damage and quasi-brittle failure. *J. Mech. Phys. Solids*, 103:72–99, 2017.
- [136] J.-Y. Wu and V. P. Nguyen. A length scale insensitive phase-field damage model for brittle fracture. *J. Mech. Phys. Solids*, 119:20–42, 2018.
- [137] J. Y. Wu, V. P. Nguyen, C. T. Nguyen, D. Sutula, S. Sinaie, and S. Bordas. Phase-field modeling of fracture. *Adv. Appl. Mech.*, 2019.
- [138] F. Zhou and J. F. Molinari. Stochastic fracture of ceramics under dynamic tensile loading. *Int. J. Solids Struct.*, 41:6573–6596, 2004.
- [139] J. M. Ziman and D. Thouless. Models of disorder: The theoretical physics of homogeneously disordered systems. *Phys. Today*, 33(6):57–58, 1980.
- [140] J. L. Zinszner, B. Erzar, P. Forquin, and E. Buzaud. Dynamic fragmentation of an alumina ceramic subjected to shockless spalling : An experimental and numerical study. *J. Mech. Phys. Solids*, 85:112–127, 2015.
- [141] A. Zubelewicz and Z. P. Bažant. Interface Element Modeling of Fracture in Aggregate Composites. *ASCE J. Eng. Mech.*, 113(11):1619–1630, 1987.